LOCALLY CONTROLLING THE STRUCTURE AND COMPOSITION OF ATOMICALLY-THIN FILMS

A Dissertation

Presented to the Faculty of the Graduate School

of Cornell University

In Partial Fulfillment of the Requirements for the Degree of

Doctor of Philosophy

by

Mark Philip Levendorf

January 2014

LOCALLY CONTROLLING THE STRUCTURE AND COMPOSITION OF ATOMICALLY-THIN FILMS

Mark Philip Levendorf, Ph.D.

Cornell University 2014

Graphene has generated an intense amount of interest for nearly a decade, serving as the model 2-dimensional system. With exciting optical, electrical, and physical qualities, most studies have focused on the pristine system. Much of this research has been motivated by the potential graphene has in the realms of flexible and transparent electronics, 3-dimensional circuits, and other applications. While these experiments were essential to the proliferation of the field, well-defined heterogeneous systems are critical to the successful production of any useful device. Thus, new techniques to synthesize and fabricate such systems are needed for advancement towards this end. In this thesis we investigate the rational manipulation of graphene, as well as other atomically-thin materials. These efforts first focus on synthesizing large-scale intrinsic systems, after which we controllably dope these graphene sheets. We then introduce a new method for spatial control and integration of dissimilar films, including doped and undoped graphene as well as graphene and hexagonal boron nitride. Finally, we propose novel applications of these materials, including their use as the thinnest possible protection layers.

BIOGRAPHICAL SKETCH

Mark was born in raised outside of Cleveland, Ohio where he attended University School. In the fall of 2004 he arrived in Ithaca, New York to study at Cornell University as an economics major. After taking physical chemistry, however, he decided to double major and became interested in participating in undergraduate research. He was fortunate enough to be given an opportunity to work in Jiwoong Park's lab in the spring of 2007, which ultimately led to his staying at Cornell to pursue a Ph.D.

To my parents, Erin, and Augusta

ACKNOWLEDGMENTS

Over the years I have had the great pleasure to interact and learn from a diverse group of people both at Cornell and at institutions around the world. I would first like to thank Jiwoong Park, for without his support and guidance I never would have had such an amazing opportunity. I understand how lucky I have been to work for him as both an undergraduate and a graduate student, and will be forever grateful for the mentorship he has provided. His encouragement through the drudgery of nanowire synthesis (which, it should be noted, does not make an appearance in this thesis) is a testament to the patience he has had in building up his group and educating his students. Along these lines, I'd also like to express my appreciation for having such outstanding teachers throughout my education; in particular Mr. Johnston and Professor Hines, both of whom helped spark my interest in chemistry and science in general.

I would also like to thank the other members of my committee, Will Dichtel and Clif Pollock, whose insights and advice I have benefited from immensely over the years. I am also thankful for the opportunity to interact with a number of other professors through collaborations and discussions, including Paul McEuen, David Muller, and Abhay Pasupathy. I was fortunate to have worked with a group of very talented students and postdoctoral researchers, with special thanks to Pinshane Huang, Brian Bryce, John Colson, Shriram Shivaraman, Robert Hovden, Arend van der Zande, Liuyan Zhao, Theanne Schiros, Arnab Mukherjee, and Jared Strait.

My time in graduate school would truly not have been the same without the

friendships and bonds I have formed with other members of the Park group. The inordinate amount of time I spent with Carlos Ruiz-Vargas and Wei Tsen has been particularly meaningful, and helped me grow as a person and a researcher. I will also always remember the wonderful times with Kayvon Daie, Lihong Herman, Daniel Joh, Michael Segal, Sang-Yong Ju, Robin Havener, Chibeom Park, Lola Brown, Joel Sleppy, Lujie Huang, Cheol-Joo Kim, Matt Graham, Kin Fai Mak, and Saien Xie.

Lastly, I would like to thank my friends and family. Amber J. and Tina G., who have continued to be extremely important friends despite both moving on from Cornell. My parents and sister, to whom I owe everything and who have given me support and love my entire life. And of course, my wife Augusta, who has put up with late nights and long distance for too many years and with whom I am excited to finally spend the rest of my life with.

TABLE OF CONTENTS

CHAPTER 1

INTRODUCTION AND OVERVIEW

1.1 | Thesis Overview

Graphene is a sheet of carbon atoms arranged in a honeycomb lattice and was the first atomically-thin material isolated under ambient conditions. This discovery not only sparked interest in this particular system, but also led to an explosion of research on other similar materials classified as 2-dimensional films. In addition to representing the thinnest possible system, graphene exhibits excellent electronic properties including high carrier mobilities and the observation of the quantum Hall effect. Furthermore, graphene was found to be mechanically robust as well as uniformly transparent in the visible regime—highlighting its potential use in flexible and transparent electronics. Thus, work in this area has garnered attention from all avenues of the scientific community, including government agencies, industrial corporations, and academic institutions—largely because of the promise such films have for improving or augmenting existing technologies, as well as providing new systems through which scientific advancements may be made. In order to realize the potential these materials have, however, it is important to first be able to precisely and reliably control these films. While this goal is simple in nature it is nontrivial to achieve, especially since the field of 2-dimensional materials is less than a decade old and techniques to handle these sheets are still being refined. As such, many of the early studies focused on monocrystalline flakes which demonstrated exciting intrinsic optical and electronic properties. Although these findings were critical in furthering

this field, it also became clear that more complicated and/or large-scale studies posed two major challenges:

> ***Challenge A****: Generation of well-controlled large-area samples.* Unlike bulk silicon technologies, the isolation of graphene was, until recently, done only mechanically and yielded irregularly shaped samples in small number—prohibiting statistical studies and limiting experiments to those least likely to cause damage.
>
> ***Challenge B:*** *Spatial control of physical and chemical structure.* Fabrication of useful electronic devices is highly dependent on the ability to understand and alter the chemical properties of thin films in a geometrically defined way. Due to the atomic-thinness of graphene, current techniques would damage or completely destroy samples.

Therefore, before the potential of graphene can be fully unlocked, these problems need to be resolved. Significantly, any solutions to these issues can theoretically be applied to the broad number of other 2-dimensional materials, including hexagonal boron nitride (*h*-BN) and transition metal dichalcogenides (TMDs). Along with graphene, these materials represent the three fundamental building blocks of modern electronics: conductors (graphene), insulators (*h*-BN), and semiconductors (various TMDs). Being capable of controlling these films in spatially and chemically defined ways thus opens up the door to a wealth of novel and exciting systems, such as the thinnest possible 3-dimensional electronics and atomically-thin heterostructures. The major part of this thesis will present work we have done towards this end. We will investigate **Challenge A** in Chapters 3 and 4, where we will discuss the synthesis of

graphene films and how they can be chemically controlled and altered. Chapter 5 will be devoted to **Challenge B**, where we describe the integration of these techniques in order to form new, locally defined, devices. Finally, in Chapter 6 we will shift our focus towards the use of these materials for innovative applications.

1.2 | 2-Dimensional Materials

Graphene

Graphene was first isolated in 2004[1], making it the most recent allotrope of carbon to be discovered. It is an atomically-thin sheet of graphite, and for this reason researchers consider graphene to be a truly 2-dimensional (2D) system. As indicated in Figure 1.1 below, the carbon atoms are arranged in a honeycomb fashion and are joined to three contiguous partners by sp^2 bonds. Consequently, a defect free sheet of graphene has completely delocalized π orbitals, resulting in a gigantic aromatic hydrocarbon. This results in a remarkably stable material with a uniquely well-defined surface chemistry.

The initial studies performed on graphene were almost all focused on its interesting electronic structure and properties. Most notably, graphene exhibits high carrier mobilities[2] and both integer[3,4] and fractional[5] quantum Hall effects have been observed. These first discoveries ignited intense interest in the material from a broad number of scientific and engineering fields, despite the fact that graphene does not have an intrinsic bandgap[6].

Immediately, it can be seen that in order to generate samples of graphene one can take a "top-down" approach by starting with graphite working down towards one

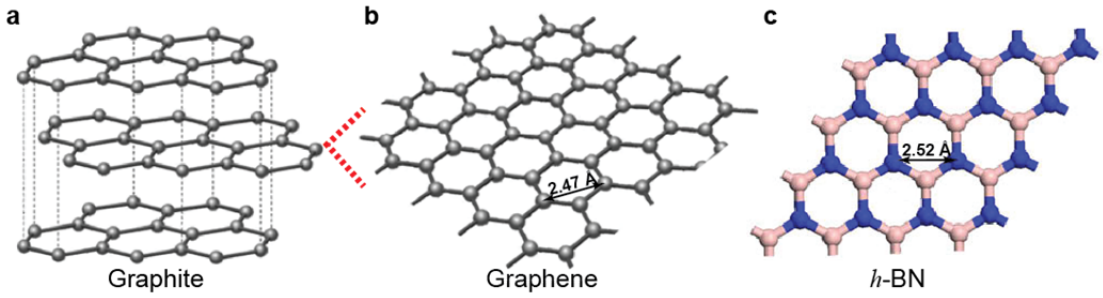

Figure 1.1 | Towards 2-Dimensional Materials. a, Bulk structure of graphite, consisting of stacked layers of graphene. **b**, Single layer of graphene showing honeycomb structure and a lattice constant of 2.47 Å. **c**, Structure of hexagonal boron nitride (*h*-BN), which is analogous to that of graphene except with pairs of B (pink) and N (blue) atoms. Notably, the lattice constant of *h*-BN, at 2.52 Å, is only ~2% different from that of graphene. **a** and **b** adapted from Ref. 6, **c** adapted from Ref. 7.

layer, or a "bottom-up" approach via chemical synthesis—posing interesting challenges to both materials scientists and organic chemists simultaneously. These and other synthetic techniques will be discussed in more detail in section 1.3.

Hexagonal Boron Nitride (h-BN)

h-BN is an exact analogue of graphene but with alternating B and N atoms (Figure 1c). Like graphene, it is atomically-thin film that can either be exfoliated from a bulk crystal or generated via synthetic routes. Unlike graphene *h*-BN is a wide gap insulator[7], due in part to the weakly ionic nature of the material, and is therefore more difficult to identify via optical and electrical measurements. However, due to these properties and the fact that it is essentially free of charge traps, *h*-BN has been proposed for use as an ideal dielectric[8] as well as a support layer for graphene electronics[9]. The reduction of dangling bonds and trapped charges (relative to a SiO_2 substrate) yields a much more uniform electronic environment for graphene by

reducing the amount of charge puddles and, therefore, local gating effects[10].

It is also interesting to note that the lattice constant of *h*-BN is similar to that of graphene (*h*-BN: 2.52 Å; Graphene: 2.47 Å). For this reason a considerable amount of work has been done towards integrating these two materials in order to create semiconducting BCN films[11,12] as well as define local *h*-BN/graphene domains and interfaces[13,14].

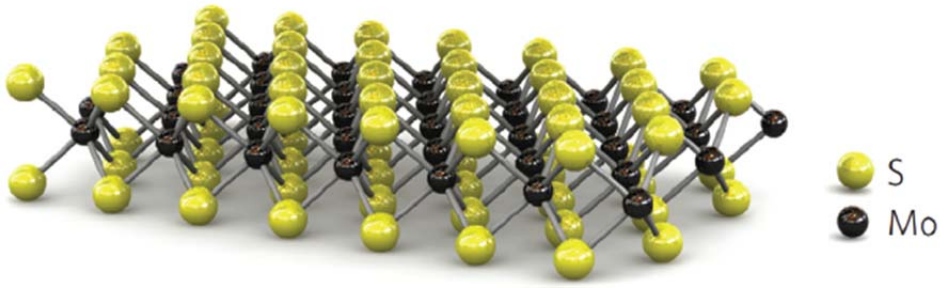

Figure 1.2 | Transition Metal Dichalcogenide Structure. The structure of MoS_2 is shown here, representative of a typical TMD material. When viewed from above the atoms are arranged in a honeycomb fashion, similar to graphene or *h*-BN, as the chalcogens are situated directly atop one another. Reproduced from Ref. 16.

Transition Metal Dichalcogenides

While not the focus of this thesis, it is worth mentioning that there exist a wide variety of other 2D materials that have similar structures to graphene. The family of transition metal dichalcogenides (TMDs) is one such group of materials. These systems all show the stoichiometry MX_2 (M: metal; X: chalcogen) and also exhibit a honeycomb arrangement, only with the two chalcogens directly on top of each other with bridging bonds to the metal atoms (see Figure 1.2 below). Examples of TMDs include MoS_2, WS_2, and $MoSe_2$, all of which are stable in single layers and show semiconducting behavior[15,16]. Additionally, recent works with MoS_2 have presented

promising routes to larger-scale methods similar to current graphene and *h*-BN processes[17,18].

1.3| Methods of Isolating or Synthesizing Graphene

The generation of graphene samples has evolved immensely since the Manchester group first published their findings nearly a decade ago. In this section we will introduce the major methods by which researchers obtain graphene. These range from the simple original techniques to the more complicated chemical procedures that are becoming more widespread in the field. Each method has distinct advantages and drawbacks, and therefore the experiment that one wishes to perform largely determines the type of graphene that will be used. Many of these techniques, in particular mechanical exfoliation and chemical vapor deposition, have also been applied to wide variety of other 2D materials, including those mentioned above.

Mechanical Exfoliation

The first reports on graphene were performed on few-layer flakes isolated from bulk graphite. This was accomplished by using a seemingly primitive technique: a fresh surface of graphite, either Kish or highly oriented pyrolytic graphite (HOPG), is adhered to a piece of scotch tape. The tape is then repeatedly folded over onto itself and then pulled apart, leaving behind thinner and thinner areas of graphite (see Figure 1.3a). After several iterations, the tape/graphite is then pressed down onto a Si/SiO_2 substrate and the adhesive is removed via standard solvent washing (Figure 1.3b)[19,20].

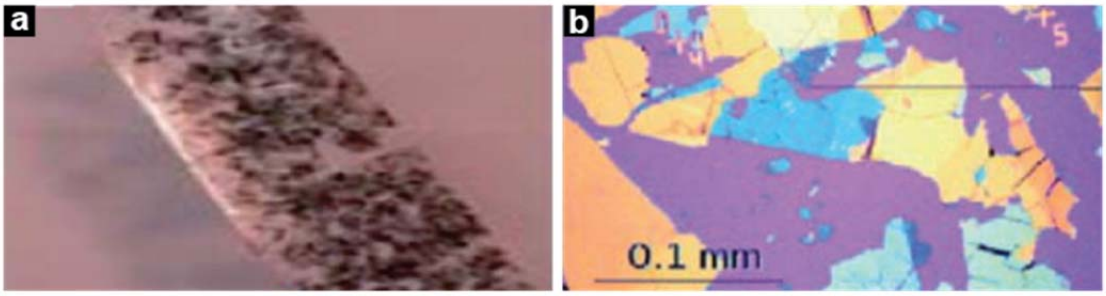

Figure 1.3 | Mechanical exfoliation of graphite. a, Photograph of a piece of scotch tape with chunks of graphite adhered. Strips of tape are repeatedly folded onto itself and then peeled apart in order to peel thinner and thinner sheets of graphene from the larger graphite flakes. **b**, After several repetitions of the peeling process the flakes are stuck to a target substrate, here a silicon wafer with thermal oxide. The golden areas are thick pieces of graphite, whereas the blue areas are thinner sheets of multilayer graphene. Adapted from Ref. 20.

The flakes left behind on the substrate are of random thickness; however, using techniques described below it is somewhat easy to determine the precise number of layers present. As seen in Figure 1.3b, the sheets are also uncontrolled in terms of size and shape, but can frequently be on the order of several tens of micrometers. Although this method can be time consuming, these graphene films are the cleanest available samples and are therefore used in more fundamental studies[3,4]. This is due to the nature of the method, where no photolithography is required to electrically isolate the graphene islands and the samples are deposited directly onto the target substrates—eliminating the need for a transfer step. Results of experiments performed on samples obtained in this way are therefore the gold standard to which synthesized graphene is compared.

Chemical Vapor Deposition (CVD)

CVD techniques have become the de facto standard for large-scale graphene synthesis. As shown schematically in Figure 1.4, these processes involve the

introduction of carbon containing reactants, usually in the presence of a catalytic film. Islands of graphene have been obtained on a wide variety of metal substrates, including Pt[21], Ru[22], and Ir[23]. Unfortunately, these growths require ultrahigh vacuum (UHV) and generate extremely small flakes with non-uniform thickness. More recently, researchers have discovered that both Ni[24,25] and Cu[26] yield large-area graphene films. In the case of Ni, the precursors decompose and the free C dissolves into the bulk metal. By controlling the cooling rate, it is then possible to recrystallize the carbon resulting in multilayer graphene sheets. In contrast to this, utilizing Cu as the catalytic layer leads to continuous monolayer sheets of graphene. This is primarily due to the fact that C is far less soluble in Cu and the reaction is largely surface catalyzed—leading to a self-limiting situation[27]. The intricacies of these synthetic methods will be discussed in more detail in Chapter 3.

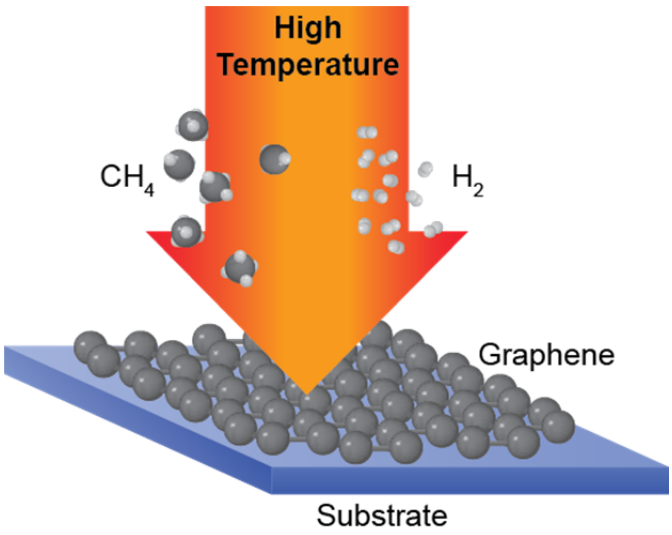

Figure 1.4 | Schematic of a chemical vapor deposition process. A general approach to the CVD synthesis of graphene. A target substrate or catalytic surface is placed in a reaction chamber, typically under a hydrogen atmosphere. A carbon source is then introduced at high temperature in order to initiate the decomposition of the precursor and facilitating the formation of graphene on the substrate.

In addition to metal substrates, certain insulating substrates have also been used in CVD processes. These growths have the advantage of not requiring a transfer step after synthesis, but most lose some degree of control over the quality of the resulting graphene. Furthermore, many methods still require a metal catalyst in some form, such allowing C to diffuse through Ni to a SiO_2 substrate below[28] or letting Cu evaporate during the growth process[29], although certain metal-free syntheses do exist[30].

Reduction of Graphite Oxide and Sublimation of Silicon Carbide

Although the previously mentioned methods are the most widely used, the reduction of graphite oxide (GO) and the sublimation of silicon carbide (SiC) have also been historically popular. GO is a compound composed of C, O, and H in largely uncontrolled proportions. In general, GO has a structure that is similar to a highly defected graphite mass, where the impurities are dangling hydroxyl or carboxylic groups randomly positioned (Figure 1.5a). These properties facilitate different types of techniques for separating layers, including rapid thermal heating or liquid exfoliation methods[31]. The resulting monolayer GO flakes can then be reduced by a variety of methods in order to produce graphene. As one might expect, however, graphene produced this way is of lower quality due to residual O and H defects. Nevertheless, this general procedure can yield large amounts of graphene flakes that can then be dropcast onto arbitrary substrates, and is therefore still employed in certain studies today.

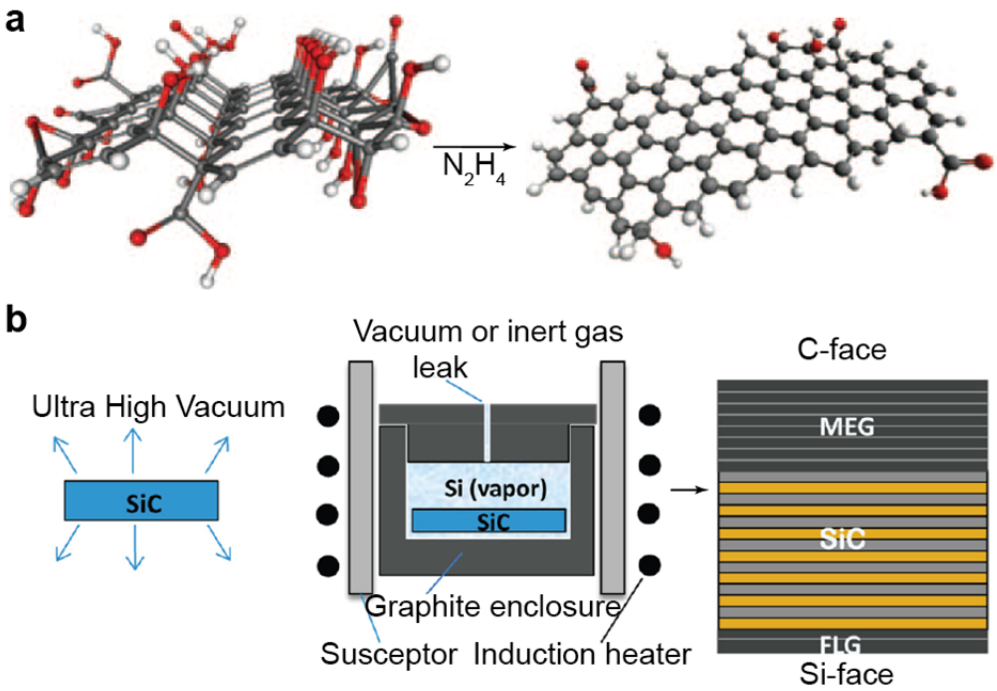

Figure 1.5 | Graphene from graphite oxide and silicon carbide. a, A typical approach to obtaining graphene via a GO source. The initial GO structure is shown on the left side, with several -COOH and -OH groups. In this example, the GO is washed with hydrazine to produce a sheet of graphene, leaving some un-reduced areas behind. Adapted from Ref. 31. **b**, Reaction scheme of producing epitaxial layers of graphene from a SiC wafer. Under a high temperature UHV environment Si is sublimed from the source wafer (left, middle), leaving behind few layer graphene (FLG) and multilayer epitaxial graphene (MLG) on the different faces of SiC. Modified from Ref. 32.

Unlike the reduction of GO, epitaxial growth of graphene on SiC has many similarities to CVD growth on metal substrates. Here, however, no additional C containing precursor is necessary, as the C in the SiC wafer acts as the source. By heating SiC to high temperatures (~1100 °C) under UHV it is possible to sublimate the Si atoms, leaving behind a C rich environment which consequently forms graphene sheets (see Figure 1.5b)[32]. Careful control of this process can lead to wafer scale continuous graphene with a predictable thickness. This method also provides an advantage in that SiC is a semi-insulating material, and thus delamination of graphene

is not necessarily required—unlike the metal catalysts described above. If one does desire to transfer the graphene, however, removal of the film is somewhat more difficult[33]. For this reason, in addition to the high cost of SiC wafers, many researchers have gravitated towards CVD synthesis.

1.4 | Identification of 2D Films

A wide variety of tools and techniques can be employed in order to both locate and identify 2D materials. In general, the most rapid tools are optical in nature, however, scanning probe and electron microscopies are also commonly used. Perhaps surprisingly, even though these films are only a single atom thick, these techniques are both easily employed and accurate, allowing researchers to quickly confirm the presence of a film and even the number of layers.

Optical Microscopy

Despite the atomically-thin nature of graphene, locating and determining the precise number of layers is a relatively straightforward process. Due to graphene's unique electronic structure, it has an unexpectedly high and uniform optical absorbance in the white light regime. Figure 1.6a demonstrates that each layer of graphene absorbs ~2.3% of light[34], which enables direct measurements on transparent substrates, such as quartz or sapphire. Identification on opaque substrates is only slightly more difficult.

By tailoring the thickness of thermal oxide on a Si wafer, it is possible to induce an enhanced contrast in areas where graphene is present. This is due to the fact that the graphene is an additional film with a different index of refraction. The phase

of the incident light is therefore affected at the interface between the graphene and the SiO_2, whereas it is not in the bare regions. Thus, areas with graphene on top can exhibit changes in contrast due to both the absorption of the white light, as well as constructive interference[35]. As can be determined from Figure 1.6b above, experimentalists typically use wafers with oxide thicknesses of either ~90 nm or ~300 nm, which provide maximal contrast over the visible range. An example of this is shown in Figure 1.6c, where on 300 nm of SiO_2 (left) graphene is clearly visible, whereas on 200 nm (right) it is indistinguishable from the background.

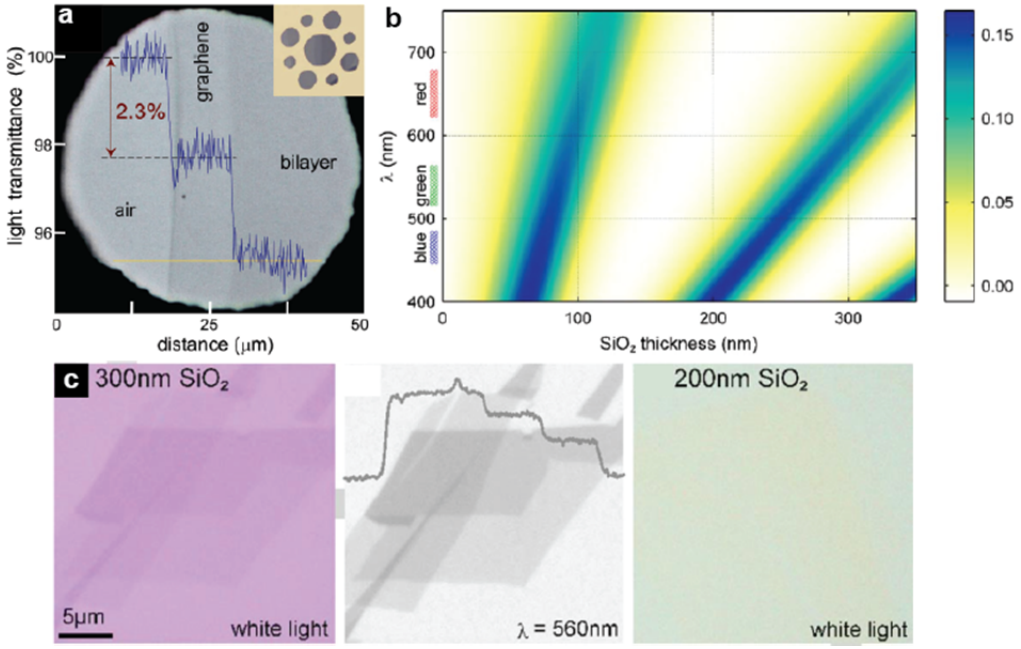

Figure 1.6 | Identification of graphene layers using optical microscopy. a, Due to the unique electronic structure of graphene, individual layers absorb ~2.3% of white light. Using this property it is possible to determine the exact number of layers present. Reproduced from Ref 34. **b**, Tailoring the SiO_2 thickness on Si wafers enhances the contrast of areas with graphene, allowing observation under white light. **c**, Graphene is clearly visible on 300 nm of SiO2 (left), but not on 200 nm (right), as predicted from the contrast plot shown in **b**. **b** and **c** reproduced from Ref. 35.

Optical spectroscopies can also be used to provide a more direct confirmation

of the material composition. For 2D materials like *h*-BN such measurements are necessary, as they are much more difficult to see on conventional substrates. Raman spectroscopy is perhaps the most commonly used technique for this purpose. Briefly, different materials exhibit dissimilar optical phonon modes due to their structures and compositions. The energies of these characteristic modes give rise to a distinctive spectrum for each type of film. This technique will be discussed in more detail in Chapter 2, as the information obtained can be used to more carefully characterize graphene sheets. Other spectroscopic techniques, such as UV-Vis-IR and, more recently, deep UV (DUV) imaging are also used, although they are less common due to either the restrictions on substrates (UV-Vis-IR) or the difficulty of implementing an efficient setup (DUV). Like Raman spectroscopy, these methods also provide unique spectra for each type of 2D material.

Atomic Force Microscopy (AFM)

While optical techniques can provide an indirect measurement of the number of layers, AFM gives explicit information on the height of the material. With proper calibration, these values can be precise, providing Angstrom resolution. After this number is determined, using the characteristic interlayer spacing it is possible to calculate how many layers are present. In order to obtain accurate information, however, one must also take into account differences in the van der Waals interactions between the substrate and the layered material. This, or material trapped in between the two, can lead to misleading height values, and must be properly corrected for. For example, graphite is known to have an interlayer spacing of ~3.4 Å, but, as shown in

Figure 1.7a, even mechanically exfoliated single layers are never measured as such[4]. Consequently, many of the early AFM measurements were correlated with transmission electron microscopy studies, which provided a more definitive picture.

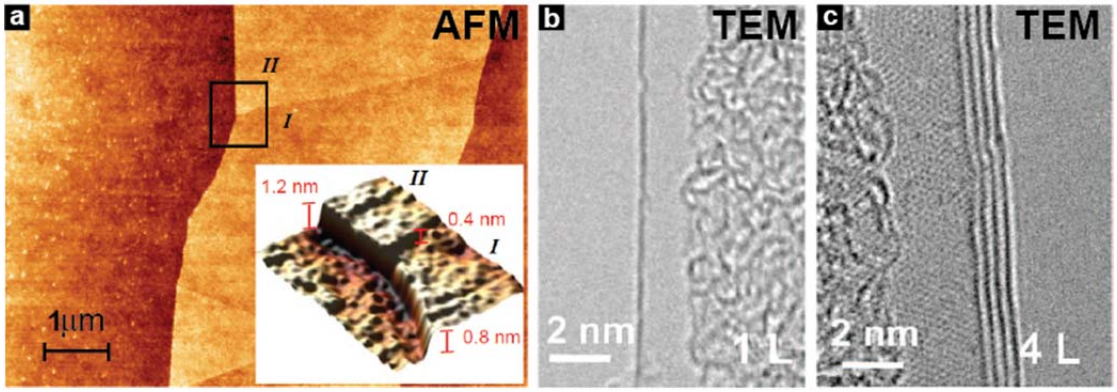

Figure 1.7 | Determining layer number and composition using atomic force microscopy and transmission electron microscopy. a, AFM allows for direct measurement of the number of layers of 2D materials. Because of interactions with the substrate and/or trapped materials, the first layer of graphene does not show the expected height difference, however the second layer is as predicted (inset). Reproduced from Ref. 4. **b**, **c**, TEM enables accurate distinguishing between monolayer graphene (**b**) and multi-layer graphene (**c**). Reproduced from Ref. 24.

Transmission Electron Microscopy (TEM)

TEM is yet another tool that can be helpful in determining the number of layers present. For these measurements, films can simply be suspended on standard TEM grids. Due to the nature of this process, graphene films tend to fold over at a number of locations. This causes a striation of intensity that corresponds to the number of layers involved in the fold[24]. If suspension is impossible due to sample size one can also use solid supports. The substrate can then be cleaved and positioned perpendicular to the electron beam. This takes advantage of the tool's X-Y resolution and allows researchers to observe the position of individual layers. As neither of these

methods require atomic-resolution, these techniques can readily be performed on any standard TEM. Correlating these images with either AFM or optical studies allows for experimentalists to use these more rapid techniques in order to confidently assign layer thicknesses of individual samples.

If further confirmation is required higher resolution TEMs can be used to identity individual atoms. Scanning TEM (STEM) is one such technique that explicitly determines the makeup and structure of films[12]. These setups require great deal of both technical expertise and monetary investment, however, and are therefore less commonly used. Despite this limited availability, the information that is gathered from these measurements is invaluable to confirming structural and compositional makeup. For example, STEM recently helped confirm theoretical predictions regarding the nature of point defects and grain boundary formation in single layer graphene (SLG)[36,37].

1.5 | Summary

The discovery of graphene represented the birth of an entire new field of science. While this area is less than a decade old, an immense amount of progress has been made in terms of understanding and synthesizing graphene. The techniques and experiments that arose from this material are now being used to explore the plethora of other 2D systems, yet the challenges discussed in 1.1 still exist. Although significant advancements have been made towards synthesis of large-area films, none of the current methods are easily integrated with existing device technologies, nor do they yield films that meet the

stringent requirements of uniformity that exist in the silicon industry. Further, the spatially defined modulation of the properties of atomically thin-film has been largely ignored by the greater scientific community, resulting in state-of-the-art procedures that are heavy handed or not easily reproduced. By establishing a set of tools that provides experimentalists with a greater degree of precision and accuracy over the attributes of their samples, we not only open up the door to high quality studies in the future, but also enable the investigation of the broader macroscopic properties of these films.

Here, we have introduced the basic properties and methods of synthesis for graphene and *h*-BN, the major focuses of this work. We have also discussed the tools used to locate and identify these films. In the following chapters, we will first begin by introducing the characterization methods used throughout this thesis. Many of these techniques have a basis in the tools already introduced, but provide more in depth information regarding quality and composition. After establishing these concepts, we will then move on to the work we have done to address the issues presented in 1.1. In Chapter 3 we discuss the synthesis and characterization of intrinsic CVD graphene films. Within this chapter we will also present advancements we have made towards the integration of these methods with existing processing technologies. Next we will discuss the global properties of these sheets, and how these improvements can be utilized in novel applications and structures. In Chapter 4 we will then

examine the chemical control and modification of these intrinsic graphene sheets. Dopants of both *p*- and *n*-type can be introduced into graphene films in a controllable and stable way, which we will show in this section. Once the characteristics of these doped films have been established, we will demonstrate our ability to apply this synthetic control in a spatially defined way allowing us to fabricate completely new device structures (Chapter 5), as well as turn our attention to interesting applications of such films (Chapter 6).

REFERENCES

1. Novoselov, K. S. *et al.* Electric field effect in atomically thin carbon films. *Science* **306,** 666–669 (2004).

2. Bolotin, K. I. *et al.* Ultrahigh electron mobility in suspended graphene. *Solid State Commun.* **146,** 351–355 (2008).

3. Novoselov, K. S. *et al.* Two-dimensional gas of massless Dirac fermions in graphene. *Nature* **438,** 197–200 (2005).

4. Zhang, Y., Tan, Y.-W., Stormer, H. L. & Kim, P. Experimental observation of the quantum Hall effect and Berry's phase in graphene. *Nature* **438,** 201–204 (2005).

5. Du, X., Skachko, I., Duerr, F., Luican, A. & Andrei, E. Y. Fractional quantum Hall effect and insulating phase of Dirac electrons in graphene. *Nature* **462,** 192–195 (2009).

6. Scarselli, M., Castrucci, P. & De Crescenzi, M. Electronic and optoelectronic nano-devices based on carbon nanotubes. *J. Phys. Condens. Matter* **24,** 313202 (2012).

7. Tang, S. & Cao, Z. Structural and electronic properties of the fully hydrogenated boron nitride sheets and nanoribbons: Insight from first-principles calculations. *Chem. Phys. Lett.* **488,** 67–72 (2010).

8. Song, L. *et al.* Large scale growth and characterization of atomic hexagonal boron nitride layers. *Nano Lett.* **10,** 3209–3215 (2010).

9. Dean, C. R. *et al.* Boron nitride substrates for high-quality graphene electronics. *Nature Nanotech.* **5,** 722–726 (2010).

10. Xue, J. *et al.* Scanning tunnelling microscopy and spectroscopy of ultra-flat graphene on hexagonal boron nitride. *Nature Mater.* **10,** 282–285 (2011).

11. Song, L. *et al.* Binary and ternary atomic layers built from carbon, boron, and nitrogen. *Adv. Mater.* **24,** 4878–4895 (2012).

12. Krivanek, O. L. *et al.* Atom-by-atom structural and chemical analysis by annular dark-field electron microscopy. *Nature* **464,** 571–574 (2010).

13. Sutter, P., Cortes, R., Lahiri, J. & Sutter, E. Interface formation in monolayer graphene-boron nitride heterostructures. *Nano Lett.* **12,** 4869–4874 (2012).

14. Levendorf, M. P. *et al.* Graphene and boron nitride lateral heterostructures for atomically thin circuitry. *Nature* **488,** 627–632 (2012).

15. Coleman, J. N. *et al.* Two-dimensional nanosheets produced by liquid exfoliation of layered materials. *Science* **331,** 568–571 (2011).

16. Radisavljevic, B., Radenovic, A., Brivio, J., Giacometti, V. & Kis, A. Single-layer MoS2 transistors. *Nature Nanotech.* **6,** 147–150 (2011).

17. Lee, Y.-H. *et al.* Synthesis of large-area MoS_2 atomic layers with chemical vapor deposition. *Adv. Mater.* **24,** 2320–2325 (2012).

18. Shi, Y. *et al.* van der Waals epitaxy of MoS_2 layers using graphene as growth templates. *Nano Lett.* **12,** 2784–2791 (2012).

19. Novoselov, K. S. *et al.* Two-dimensional atomic crystals. *Proc. Natl. Acad. Sci.* **102,** 10451–10453 (2005).

20. Kang, J., Shin, D., Bae, S. & Hong, B. H. Graphene transfer: key for applications. *Nanoscale* **4,** 5527–5537 (2012).

21. Sutter, P., Sadowski, J. T. & Sutter, E. Graphene on Pt(111): Growth and substrate interaction. *Phys. Rev. B.* **80,** 245411 (2009).

22. Sutter, P. W., Flege, J.-I. & Sutter, E. a. Epitaxial graphene on ruthenium. *Nature Mater.* **7,** 406–411 (2008).

23. N'Diaye, A. T., Coraux, J., Plasa, T. N., Busse, C. & Michely, T. Structure of epitaxial graphene on Ir(111). *New J. Phys.* **10,** 043033 (2008).

24. Reina, A. *et al.* Large area, few-layer graphene films on arbitrary substrates by chemical vapor deposition. *Nano Lett.* **9,** 30–35 (2009).

25. Kim, K. S. *et al.* Large-scale pattern growth of graphene films for stretchable transparent electrodes. *Nature* **457,** 706–710 (2009).

26. Li, X. *et al.* Large-area synthesis of high-quality and uniform graphene films on copper foils. *Science* **324,** 1312–1314 (2009).

27. Li, X., Cai, W., Colombo, L. & Ruoff, R. S. Evolution of graphene growth on Ni and Cu by carbon isotope labeling. *Nano Lett.* **9,** 4268–4272 (2009).

28. Peng, Z., Yan, Z., Sun, Z. & Tour, J. M. Direct growth of bilayer graphene on SiO_2 substrates by carbon diffusion through nickel. *ACS Nano* **5,** 8241–8247 (2011).

29. Ismach, A. *et al.* Direct chemical vapor deposition of graphene on dielectric surfaces. *Nano Lett.* **10,** 1542–1548 (2010).

30. Song, H. J. *et al.* Large scale metal-free synthesis of graphene on sapphire and transfer-free device fabrication. *Nanoscale* **4,** 3050–3054 (2012).

31. Mao, S., Pu, H. & Chen, J. Graphene oxide and its reduction: modeling and experimental progress. *R. Soc. Chem. Adv.* **2,** 2643 (2012).

32. De Heer, W. A. *et al.* Large area and structured epitaxial graphene produced by confinement controlled sublimation of silicon carbide. *Proc. Natl. Acad. Sci.* **108,** 16900–16905 (2011).

33. Shivaraman, S. *et al.* Free-standing epitaxial graphene. *Nano Lett.* **9,** 3100–3105 (2009).

34. Nair, R. R. *et al.* Fine structure constant defines visual transparency of graphene. *Science* **320,** 1308 (2008).

35. Blake, P. *et al.* Making graphene visible. *Appl. Phys. Lett.* **91,** 063124 (2007).

36. Huang, P. Y. *et al.* Grains and grain boundaries in single-layer graphene atomic patchwork quilts. *Nature* **469,** 389–392 (2011).

37. Meyer, J. C. *et al.* Experimental analysis of charge redistribution due to chemical bonding by high-resolution transmission electron microscopy. *Nature Mater.* **10,** 209–215 (2011).

CHAPTER 2:

CHARACTERIZATION OF ATOMICALLY-THIN MATERIALS

2.1 | Overview

The characterization of 2D materials introduces a unique combination of new problems and distinct advantages relative to the study of bulk crystals. Many techniques used to study 3D systems may be useless, or even destructive to the sheet. On the other hand, surface specific tools that may provide limited data on thicker films can be helpful in the study of 2D systems. For example, energy-dispersive X-ray spectroscopy (EDS) is a technique commonly employed that provides quantitative elemental analysis of materials and is easily integrated with scanning electron microscopy (SEM) systems. This tool cannot be used for studying atomically-thin films, however, because the incident beam penetrates a micrometer into the sample, meaning that any signal generated from the 2D film will be overwhelmed by background noise. Consequently, a technique related to EDS known as X-ray photoelectron spectroscopy (XPS), is more commonly used to study single-atom thick materials. XPS is designed to be surface sensitive, meaning that the collected data will come only from the thin sheet. Thus, while techniques like XPS provide limited information about conventional thin-films, for atomically-thin materials they can provide a complete picture. These unique difficulties and benefits have led to a rapid realignment of the tools and techniques used to investigate graphene and related materials.

In this Chapter we will introduce and discuss the major methods used in the characterization of our 2D films. In general there are three overarching categories of analyses we are interested in: compositional, structural, and electrical. The combination and correlation of these approaches allow us to compile a more complete understanding of our system, and therefore provide insight on how to tailor its properties in the future. The techniques discussed here are general, and can be used in the study of any 2D material, however, we will focus on their applications to graphene. We will first discuss spectroscopic tools, most notably Raman spectroscopy and methods derived from this effect. Next, we will introduce methods of structural analysis of our films, including the observation of both accidental and intentional defects. The last portion of this chapter will focus on the analysis of field effect transistors (FETs), and introduce the most common measurements performed on these devices.

2.2 | Compositional Analysis

Spectroscopic tools are particularly useful for studying atomically-thin materials as they are typically non-destructive and sample preparation is usually straightforward. Additionally, most methods are relatively rapid, enabling spatial mapping of our materials—which is critical when integrating multiple films of different properties. In general, these tools function by exploiting the interaction of a probe with matter, providing information on the chemical composition of the material and, in many cases, suggesting structural characteristics as well.

Raman Spectroscopy

Raman spectroscopy is one of the most popular and robust methods of identifying and understanding graphene films. This technique takes advantage of characteristic inelastic scattering under laser light. Due to interactions with the vibrational modes of a material, the energy of the incident photons can be shifted up or down. This leads to a unique spectral profile that provides information about the phonon modes, and is thus sensitive to any changes in physical and/or electronic structure[1]. This is particularly useful for studying 2D materials, as in many cases the band structure changes as a function of the number of layers, therefore allowing experimentalists to verify both the presence of a film as well as determine the thickness—and in some cases the stacking order—of the material[2].

There are three major peaks used to identify graphene. These features are known as the G, D, and 2D (or G') peaks (see Figure 2.1). The G-band ('Graphite'-band) is a first order intravalley process that is present at roughly 1580 cm^{-1} and has a relatively constant shape for almost all thicknesses of graphite. The D-band, located at ~1350 cm^{-1}, is so called because it is a defect mediated intervalley scattering process[3]. This peak, therefore, is not present in ideal graphene sheets and is consequently used in order to determine the approximate density of defects. "Defects" can be intentional dopants, the presence of grain boundaries, edge-states, vacancies, or anything else that deviates from the C hexagonal crystal structure. While the D-band is the most intense defect related process, if the concentration of imperfections becomes large enough, a second resonance known as the D'-band can appear at ~1620 cm^{-1}.

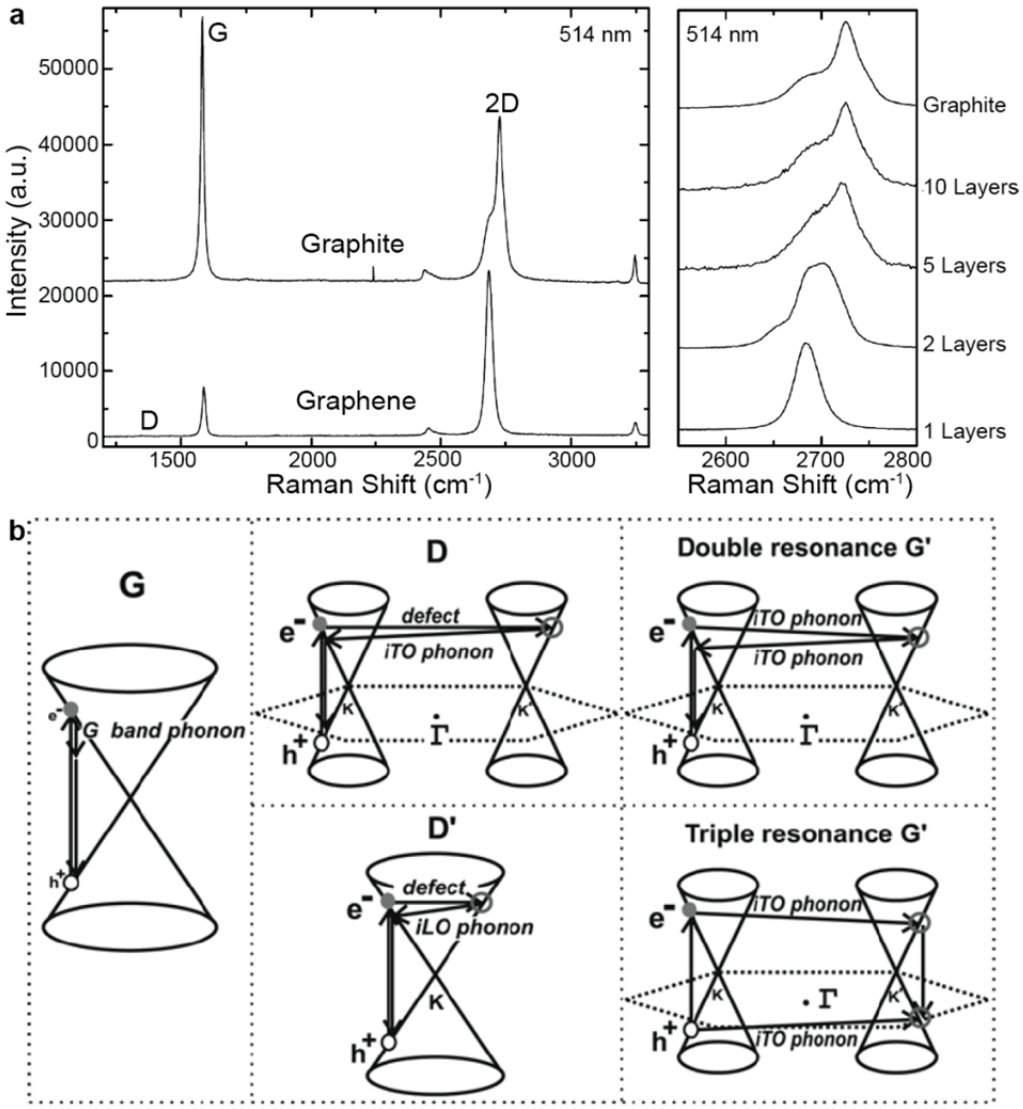

Figure 2.1 | Raman spectra of graphite and graphene. a, Left: ideal spectra of graphite (top) and graphene (bottom), showing the distinct differences between the two. As the D-band is only present when there are defects, ideal graphite/graphene do not exhibit this peak, however it's approximate location is indicated. Right: 2D band as a function of layer thickness. As fewer layers of AB stacked graphene are present, the 2D band changes from a multipeaked lineshape to a single Lorentzian. Modified from Ref. 2. **b**, Processes of the Raman peaks present in **a**. The G-band is the only major first-order process, whereas the D and 2D (labeled G' here) are both second-order intervalley processes. Reproduced from Ref. 3.

The last peak, positioned at ~2700 cm^{-1}, is known as the 2D peak. Despite the name, this second order intervalley process does not involve a defect and is named

solely because it appears at roughly twice the D-band. For this reason, some researchers choose to refer to it as the G' peak as it comes purely from the graphite structure. The 2D band is particularly helpful as the lineshape changes dramatically as a function of layer number[2]. As the system changes from bulk graphite down to single layer graphene, the lineshape shifts from a multi-peaked structure to a single Lorentzian shape (see Figure 2.1a, right). While this is incredibly helpful, it is important to note that this change only occurs if the layers are strongly coupled and stacked in an AB ("Bernal") fashion. If the layers are decoupled, or are rotated by some degree, the changes are vastly different[4,5].

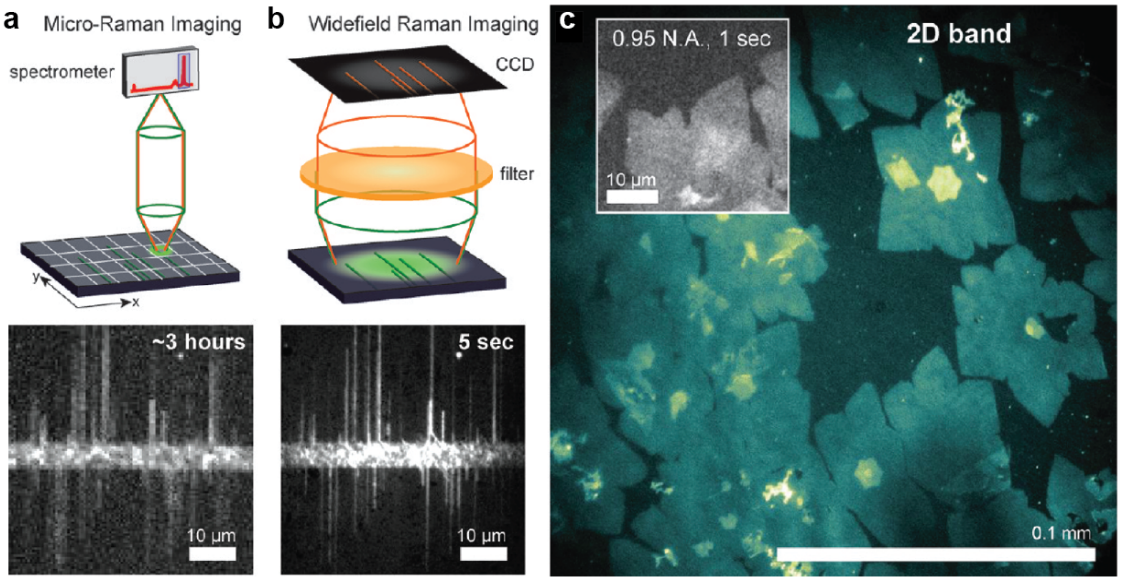

Figure 2.2 | Imaging materials with Raman spectroscopy. a, Conventional imaging of a carbon nanotube sample using a confocal geometry versus **b**, Widefield Raman setup. **c**, False color image of the 2D-band for a sample of graphene (bright areas). Reproduced from Ref. 8.

In addition to providing information on the number of layers, the positions of the peaks can play a helpful role in determining the effect of dopants on the graphene

sheet. Observation of a blue shift in the G-band position as well as red shift of the 2D-band is indicative of *n*-type doping, whereas a blue shift in both the G and 2D peaks suggests *p*-type doping[6]. By combining these measurements with D/G peak ratios it is possible to generate an estimate of both dopant type and density[7], although one must be careful to account for external effects as well. This analysis can therefore be useful when attempting to tailor the chemical and electrical properties of graphene sheets.

Most Raman measurements are taken using a confocal setup, making the mapping of a material time-consuming. This is primarily due to the fact that the excitation laser must be raster scanned across the material, and spectra must be acquired at each point. An alternative to this is to instead employ a wide-field illumination geometry (Figure 2.2b), and choose filters on the collection end that correspond to specific Raman peaks. This allows for rapid verification of film integrity and diffraction limited spatial mapping[8]. This is particularly helpful for locating and characterizing 2D films that are on substrates where their white-light contrast is low or there are multiple types of materials. One such image is shown in Figure 2.2c, where the islands of graphene (bright areas) are clearly visible with high resolution, despite a short acquisition time (~300 s). Thus, this method enables quick judgment over the success or failure of growths and patterning.

X-ray Photoelectron Spectroscopy (XPS)

As was introduced in 2.1, XPS is a spectroscopic technique that quantitatively detects elemental composition, and thus provides information on the empirical formula of the material in question. As the name suggests, this technique utilizes the

photoelectric effect by exposing the surface to a monochromatic beam of X-rays. In turn, the surface ejects electrons with specific kinetic energies, from which their binding energy can then be calculated. Importantly, only surface electrons (<10 nm) can escape elastically, making this technique helpful in the analysis of atomically-thin sheets. As each element has characteristic binding energies that correspond to their electron configuration, the data can be used to determine both the composition and bonding state of the atoms constituting the film. This technique has limited use in the analysis of graphene—due to the fact that C is a ubiquitous contaminant and dopants will typically be below the detection limit of 0.1%—but can be very helpful in verifying the composition and stoichiometry of both *h*-BN or TMD samples[9–12].

Electron Energy Loss Spectroscopy (EELS)

EELS is another tool that enables the elemental analysis of materials. Samples are first subjected to a beam of electrons with known kinetic energy. A small fraction of these particles can experience inelastic scattering, with the amount of energy lost being related to atomic composition, bonding structure, and several other properties. As opposed to other electron spectroscopies, like EDS, EELS is well suited for elements with low atomic numbers—such as C or common dopant elements like B, P, and N. Like in XPS, each element has characteristic signatures that are related to their bonding nature. It is therefore possible to use this technique to not only differentiate between different C allotropes (including diamond, graphite, and amorphous C)[13], but also confirm that dopant atoms are embedded into the structure of the material as opposed to being loosely bound to the surface. While the resolution afforded by this

measurement is much higher than that of XPS (Angstrom versus millimeter scale), sample preparation is more cumbersome, as they must be either suspended or milled to a thickness of ~30 nm in order to allow the electron beam to pass through.

2.3 | Structural Analysis

While spectroscopic tools can provide detailed information on the atomic composition of thin films, they do not explicitly indicate their structural properties. Although certain information, such as the bonding state of the atoms, can be gleaned, in order to directly determine how the atoms come together other techniques must be used. The approaches discussed below enable the visualization of atomic defects and grain boundaries, and thus provide a physical context for spectroscopic data.

Scanning Tunneling Microscopy (STM)

STM is a tool that enables atomic resolution images by operating on the principle of electron tunneling. A small bias is applied to an atomically-sharp probe that is lowered close enough to the sample surface so as to induce a measurable tunneling current. This current varies as a function of the local density of states (LDOS) of the sample, as well as the tip voltage and position, allowing for a precise mapping of atomic positions on a surface. The resulting topographic maps of the material can then be combined with scanning tunneling spectroscopy (STS) measurements in order to provide a detailed look at the spatial dependence of the materials electronic structure. In STS measurements, the tip is parked at a particular point while sweeping the bias, inducing a change in current—thus probing the LDOS. This makes STM a powerful tool for investigating materials that are atomically-thin.

The conducting nature of graphene makes it particularly well-suited for study, hence STM has been employed to analyze various properties ranging from the effects of charge puddles[14], Moiré patterns and the emergence of superlattice Dirac points[15], and—most importantly to this work—the structure and impact of local defects.

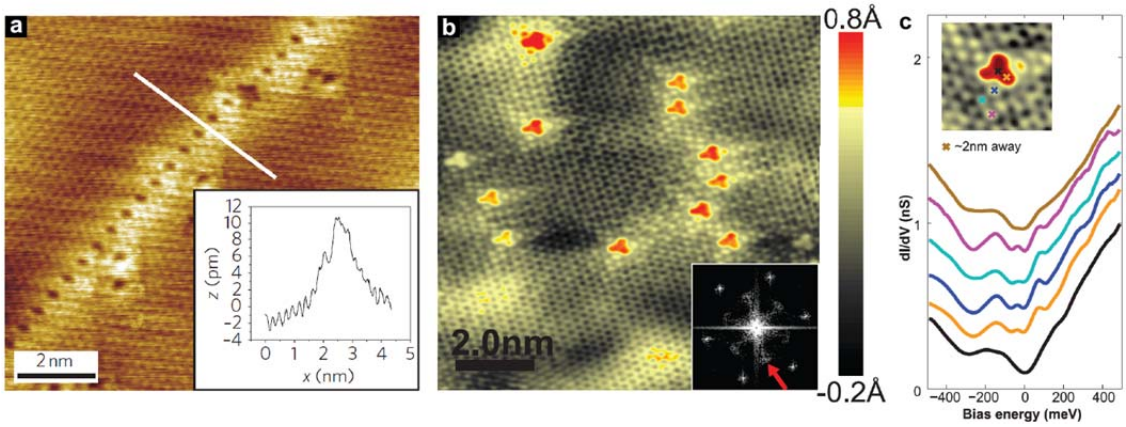

Figure 2.3 | Imaging structural defects with STM. a, STM image of a grain boundary in CVD graphene grown on a Ni substrate. The grain boundary consists of a series of two 5-membered rings joined to an 8-member ring. From Ref. 16. **b**, Topographic STM image of a graphene sheet with substitutional N dopant atoms (red regions). **c**, Scanning tunneling spectroscopy (STS) at different locations near a N dopant. The dip present at ~300 meV indicates *n*-type doping behavior. **b** and **c** reproduced from Ref. 17.

STM was used to provide the first look at grain boundaries in CVD graphene[16] (Figure 2.3a), as well as the first visualization of intentional dopant atoms in the graphene lattice[17] (Figure 2.3b). These data yielded the first understandings of the role of these defects in effecting the electronic structure of graphene, suggesting that grain boundaries can act as one-dimensional wires and providing insight into the *n*-type doping nature of N atoms (see Figure 2.3c). These studies have in turn influenced our abilities to control the structural and chemical properties of graphene by suggesting compatible dopant atoms as well as narrowing the parameter space within which to

search.

Annular Dark-Field Scanning TEM (ADF-STEM) and Dark-Field TEM (DF-TEM)

As introduced in Chapter 1, TEM offers the powerful ability to identify atomic structure and placement in thin films. One specific technique, known as annular dark-field (ADF) scanning TEM, enabled the first direct observation of a grain boundary in CVD graphene grown on Cu[18], shown below in Figure 2.4a. This finding was enormously important to the field—confirming the predicted 5-7 ring structures and giving support to various theoretical works—but the experiment was difficult to perform and, like STM, the technique is relatively slow and requires extremely clean samples. Contrary to ADF-STEM, regular dark-field (DF) imaging can be used to rapidly identify grain orientations and map out their locations, even on films supported by a thin membrane[18].

This high throughput technique operates by isolating intensity from only one orientation of crystal grains. Due to the six-fold symmetry of graphene, a set of six spots is generated in electron diffraction measurements. Additionally, any real-space rotation of a graphene grain will correspond to a rotation of the diffraction points in reciprocal-space. This property allows researchers to, by using a selective aperture, collect electrons that result from the diffraction of a single orientation. This results in a real-space image that highlights only grains that correspond to a single (or narrow spread) alignment. An example of this is shown in Figure 2.4b, where the three bright regions correspond to the grain orientation selected in the inset. One can then repeat this process several times in order to generate a false color image (Figure 2.4c) that

maps out individual grains over areas >100 μm^2. This method is a critical step of several works that will be presented in this thesis, and has now been used to study the influence of growth parameters on the grain structure for not only graphene, but for *h*-BN[19] and various TMD[11,20] materials as well.

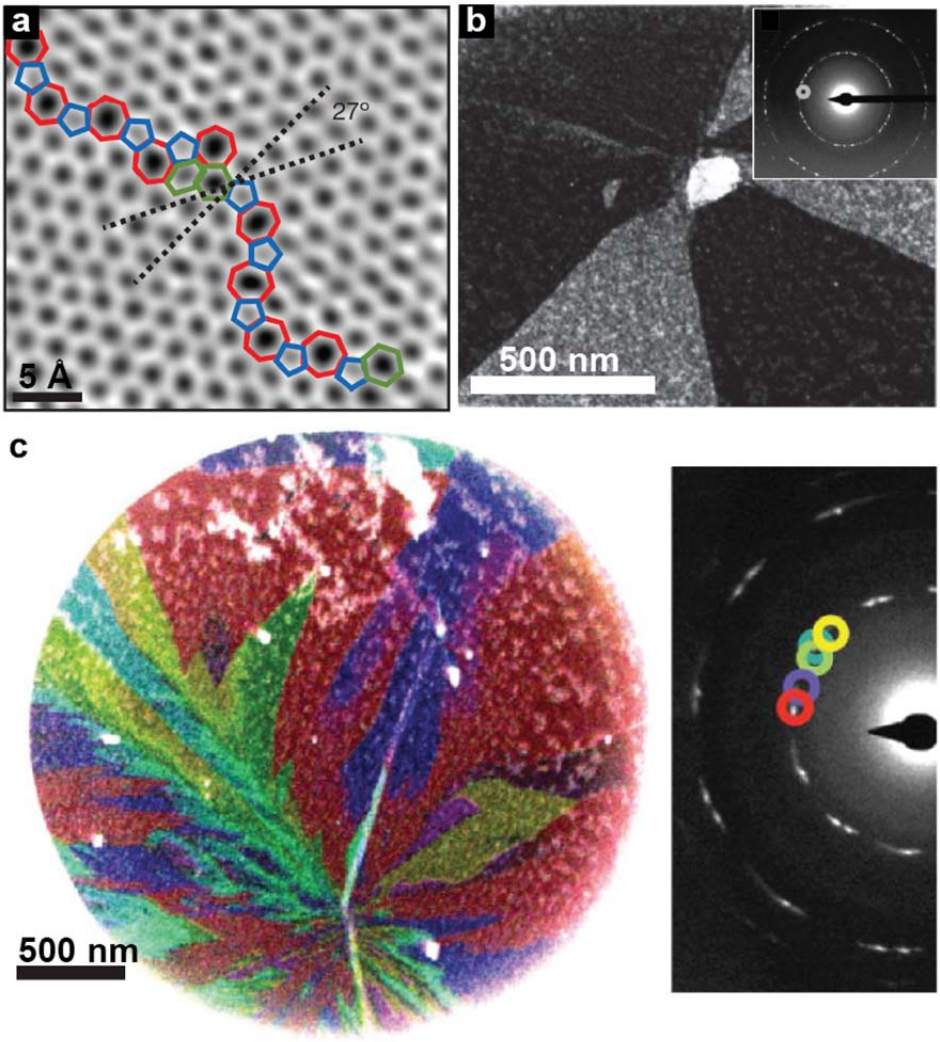

Figure 2.4 | TEM Imaging of suspended graphene films. a, ADF-STEM image of a grain boundary in CVD graphene grown on Cu foil. Unlike the Ni CVD graphene case, this boundary consists of a series of pentagons and heptagons. **b**, DF-TEM image of a single grain orientation, as shown selected in the inset. **c**, By repeating the process in **b** for a series of grain orientations and then color coding (right), a false color image depicting the grain structure of the film can be generated (left). Figures adapted from Ref. 18.

2.4 | Field Effect Transistors (FETs)

Method of Operation

In this work, the vast majority of electrical characterization is performed on field effect transistor (FET) devices. This type of system is one of the basic units of modern electronics, enabling the tuning of channel conductivity through the use of an electric field. Fundamentally, FETs all follow the same general structure and method of operation. The most basic device has three electrodes, or terminals—the source and drain (S and D) of the conducting channel, and the gate (G). By convention, carriers are injected into the channel through the S electrode, and collected at the D. The G electrode rests atop a layer of dielectric material, isolating it from the conducting channel completely. A voltage can therefore be applied to G (V_g), generating an electric field which enables modulation of the current flowing through the device below. An example schematic for a graphene-based FET is shown in Figure 2.5. This capability, in combination with careful control of the channel's materials properties, allows the "turning off" ("turning on") of devices by pinching off (increasing) the conducting channel to the point where current cannot (can) flow.

Graphene FETs

Graphene is a unique material to use in a traditional FET geometry as the band structure has several unusual characteristics. Most notably, the valence and conducting bands touch—but do not overlap—at six points, known as the Dirac points (see Figure 2.6). Around these regions, the density of states linearly and symmetrically approaches zero[21], giving rise to several of graphene's unique properties, including the uniform

white light absorbance[22] and the exhibiting of an anomalous quantum Hall effect[23,24], as well as causing the ambipolar nature of graphene based electrical devices[25]. Despite the advantages that this material offers, it is impossible to turn graphene FETs (GFETs) completely off. While the DOS does go to zero at the Dirac point, graphene has been shown to have a minimum conductivity of roughly $4e^2/h$, thought to be an outcome of the presence of local charge puddles on the substrate or other external effects[25]. As a result, a great deal of effort has been made to experimentally induce a bandgap in bilayer graphene, which could increase the practical utility of such devices.

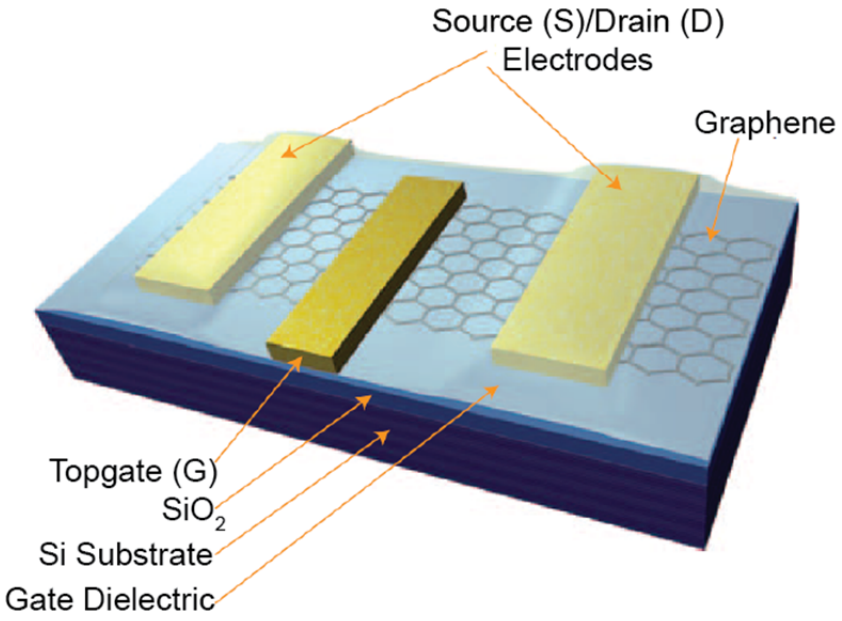

Figure 2.5 | Schematic of a standard graphene field effect transistor (GFET). Typical devices consist of at least three terminals, the source (S), drain (D), and gate (G) electrodes. Current is injected (collected) by at the S (D) terminal, and the level of current is modulated by applying a bias to the G electrode. Modified from Ref. 26.

Nevertheless, fabricating GFETs has become a standard method of characterizing the electrical properties of graphene films. Specifically, the Dirac point

resistance and low-field mobility are the most commonly used metrics. These values are directly related to the integrity of the graphene sheet and overall device quality, as any defects can decrease the mean free path of the carriers. As the measured resistance value of a GFET varies as a function of applied gate voltage, it is most fair to compare devices at the Dirac point. Complicating things, however, is the fact that there is always some degree of doping of the graphene layer, typically due to substrate or

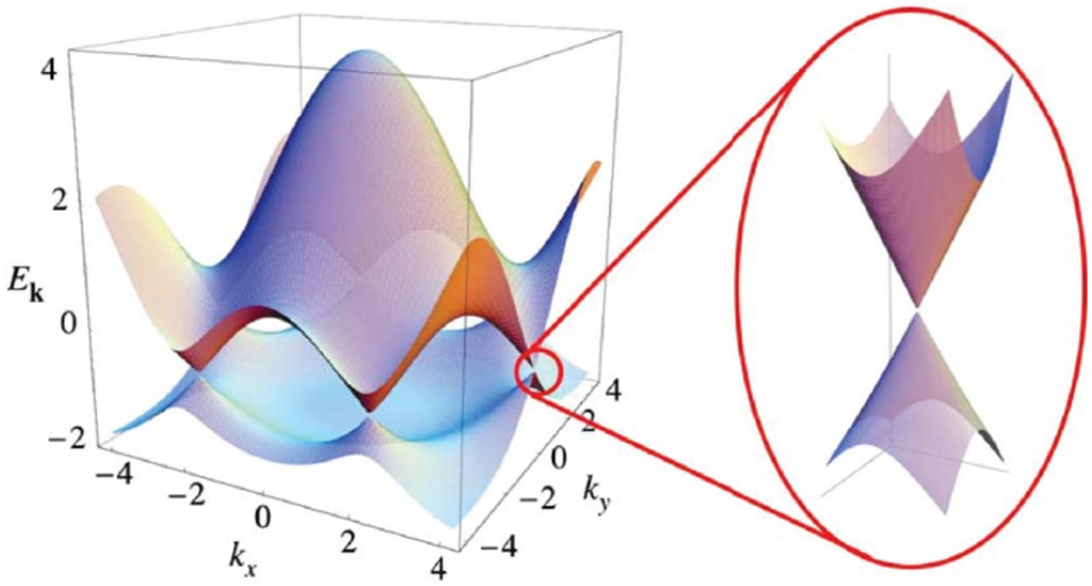

Figure 2.6 | Band structure of graphene. Many of the unique properties of graphene are a result of the linear dispersion relation in the region where the valence (lower) and conduction (upper) bands touch at a single point (Dirac point). Reproduced from Ref. 21.

adsorbate effects. Thus, one must first sweep the gate voltage in order to tune the system to the point of charge neutrality. The resistance at this point can then be extracted and normalized for the device area. It is interesting to note that resistivities for graphene are normally given in units of Ω/□, as unlike other materials graphene is taken to have "no thickness." Data collected from such measurements can then be

used to calculate the GFET mobility as well, giving the other metric by which devices are typically compared.

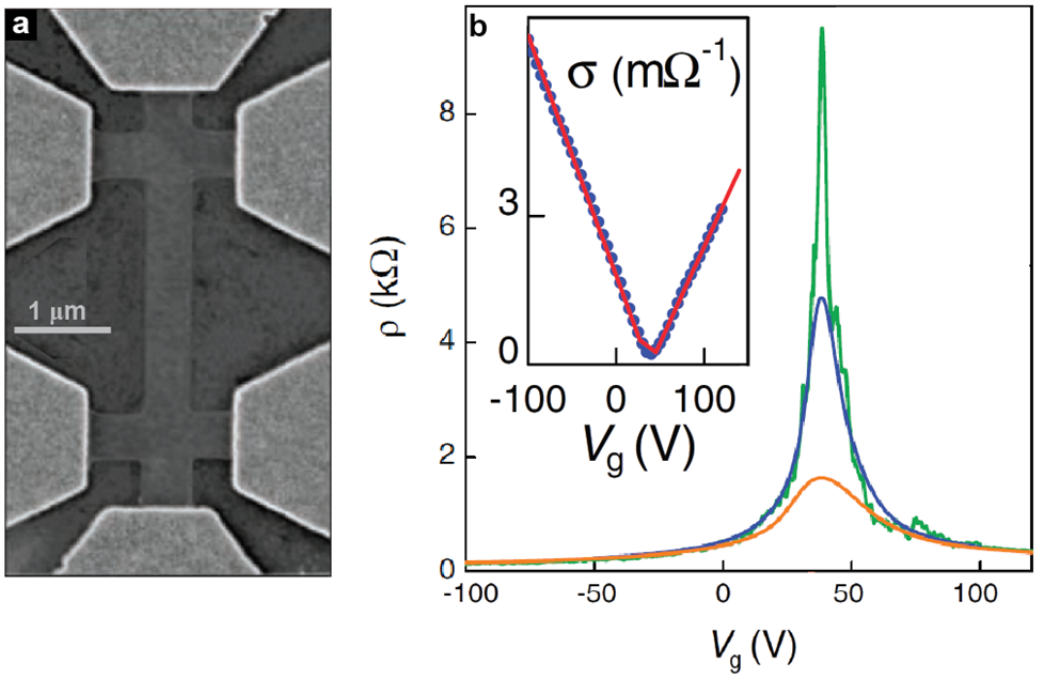

Figure 2.7 | Gate dependence of GFET devices. a, SEM image of the first GFET, fabricated from exfoliated few layer graphene. **b**, Resistivity as a function of gate voltage at different temperatures (5, 70, and 300 K top to bottom) for the device shown in **a**. Inset: Conductivity as a function of gate, showing a non-zero minimum at the Dirac point. From the slope of this data, carrier mobility can be extracted.

Electron (hole) mobility, μ_e (μ_h), is defined as how much the carrier can move under the influence of an electric field. This value is extracted from the change in device conductance (G) as a function of V_g and normalized for the capacitance of the gate dielectric (C_g), as the following equation indicates[26]:

$$\mu = \frac{1}{C_g} * \frac{dG}{dV_g}$$

Both electron and hole mobilities can be determined by merely tuning the device to either side of the Dirac point in order to change the majority carrier (see Figure 2.7b,

inset). For exfoliated graphene, these values can be extraordinarily high, with reports of suspended sheets at low temperature giving values >200,000 $cm^2/V \cdot s$[27]. Substrate effects and other defects decrease these numbers, yet devices with mobilities ~40,000 $cm^2/V \cdot s$—more than twenty times greater than that of Si—can still be easily fabricated.

2.5 | Outlook

The tools and techniques introduced in this chapter enable the basic characterization of atomically-thin materials. Throughout the remainder of this thesis, we will show that by employing these methods it is possible to create a more complete understanding of the chemical and physical properties of such films. Although many of these techniques were utilized extensively in the study of exfoliated graphene stacks, it is imperative that they also be used to understand the properties of CVD generated materials. Due to the scalable nature of this process, it is these films that show promise for their widespread integration into existing technologies. The macroscopic understanding of these films also highlights the potential for novel applications and scientific studies that are otherwise impossible using the conventional exfoliation method.

Once we have identified the innate properties of CVD films, we will then turn these characterization tools around, and use them to help guide us towards methods altering the chemical makeup and structure of graphene in a spatially defined and well-controlled manner. This capability then opens up the door for a wide variety of other experiments and device systems, ranging from the production of ultraflat 3D

electronics to the formation of *p*-*n* junctions that are a single atom thick—both of which have widespread implications in the study and use of atomically-thin materials. In the following chapter we will discuss the synthesis and properties of CVD graphene films, which lays the groundwork upon which all subsequent work is based.

REFERENCES

1. Dresselhaus, M. S., Jorio, A., Hofmann, M., Dresselhaus, G. & Saito, R. Perspectives on carbon nanotubes and graphene Raman spectroscopy. *Nano Lett.* **10**, 751–758 (2010).

2. Ferrari, A. *et al.* Raman spectrum of graphene and graphene layers. *Phys. Rev. Lett.* **97**, 187401 (2006).

3. Malard, L. M., Pimenta, M. A., Dresselhaus, G. & Dresselhaus, M. S. Raman spectroscopy in graphene. *Phys. Rep.* **473**, 51–87 (2009).

4. Kim, K. *et al.* Raman Spectroscopy Study of Rotated Double-Layer Graphene: Misorientation-Angle Dependence of Electronic Structure. *Phys. Rev. Lett.* **108**, 246103 (2012).

5. Havener, R. W., Zhuang, H., Brown, L., Hennig, R. G. & Park, J. Angle-resolved Raman imaging of interlayer rotations and interactions in twisted bilayer graphene. *Nano Lett.* **12**, 3162–3167 (2012).

6. Iqbal, M. W., Singh, A. K., Iqbal, M. Z. & Eom, J. Raman fingerprint of doping due to metal adsorbates on graphene. *J. Phys.: Condens. Matter* **24**, 335301 (2012).

7. Cancado, L. G. *et al.* Quantifying defects in graphene via Raman spectroscopy at different excitation energies. *Nano Lett.* **11**, 3190-3196 (2011).

8. Havener, R. W. *et al.* High-throughput graphene imaging on arbitrary substrates with widefield Raman spectroscopy. *ACS nano* **6**, 373–380 (2012).

9. Song, L. *et al.* Large scale growth and characterization of atomic hexagonal boron nitride layers. *Nano Lett.* **10**, 3209–3215 (2010).

10. Shi, Y. *et al.* Synthesis of Few-Layer Hexagonal Boron Nitride Thin Film by Chemical Vapor Deposition. *Nano Lett.* **10**, 4134–4139 (2010).

11. Zhan, Y., Liu, Z., Najmaei, S., Ajayan, P. M. & Lou, J. Large-area vapor-phase growth and characterization of MoS_2 atomic layers on a SiO_2 substrate. *Small* **8**, 966–971 (2012).

12. Liu, K.-K. *et al.* Growth of large-area and highly crystalline MoS_2 thin layers on insulating substrates. *Nano Lett.* **12**, 1538–1544 (2012).

13. Chu, P. K. & Li, L. Characterization of amorphous and nanocrystalline carbon films. *Mater. Chem. Phys.* **96**, 253–277 (2006).

14. Xue, J. *et al.* Scanning tunnelling microscopy and spectroscopy of ultra-flat graphene on hexagonal boron nitride. *Nature Mater.* **10**, 282–285 (2011).

15. Yankowitz, M. *et al.* Emergence of superlattice Dirac points in graphene on hexagonal boron nitride. *Nature Phys.* **8**, 382–386 (2012).

16. Lahiri, J., Lin, Y., Bozkurt, P., Oleynik, I. I. & Batzill, M. An extended defect in graphene as a metallic wire. *Nature Nanotech.* **5**, 326–329 (2010).

17. Zhao, L. *et al.* Visualizing individual nitrogen dopants in monolayer graphene. *Science* **333**, 999–1003 (2011).

18. Huang, P. Y. *et al.* Grains and grain boundaries in single-layer graphene atomic patchwork quilts. *Nature* **469**, 389–392 (2011).

19. Levendorf, M. P. *et al.* Graphene and boron nitride lateral heterostructures for atomically thin circuitry. *Nature* **488**, 627–632 (2012).

20. Van der Zande, A. M. *et al.* Grains and grain boundaries in highly crystalline monolayer molybdenum disulphide. *Nature Mater.* **12**, 554–561 (2013).

21. Castro Neto, A. H., Peres, N. M. R., Novoselov, K. S. & Geim, A. K. The electronic properties of graphene. *Reviews of Modern Physics* **81**, 109–162 (2009).

22. Nair, R. R. *et al.* Fine structure constant defines visual transparency of graphene. *Science* **320**, 1308 (2008).

23. Novoselov, K. S. *et al.* Two-dimensional gas of massless Dirac fermions in graphene. *Nature* **438**, 197–200 (2005).

24. Zhang, Y., Tan, Y.-W., Stormer, H. L. & Kim, P. Experimental observation of the quantum Hall effect and Berry's phase in graphene. *Nature* **438**, 201–204 (2005).

25. Geim, A. K. & Novoselov, K. S. The rise of graphene. *Nature Mater.* **6**, 183–191 (2007).

26. Meric, I. *et al.* Current saturation in zero-bandgap, top-gated graphene field-effect transistors. *Nature Nanotech.* **3**, 654–659 (2008).

27. Bolotin, K. I. *et al.* Ultrahigh electron mobility in suspended graphene. *Solid State Commun.* **146**, 351–355 (2008).

CHAPTER 3

CHEMICAL VAPOR DEPOSITION GRAPHENE: SYNTHESIS AND STRUCTURE

3.1 | Introduction

The discovery of CVD graphene has enabled the expansion of graphene research into many other fields, including electrochemistry, biology, and organic chemistry. This is a direct consequence of this newfound ability to generate an essentially limitless supply of this material. While this has been revolutionary for this area of research, it also introduces several new questions regarding the quality and uniformity of CVD graphene. Namely, are CVD samples of as high quality as exfoliated graphene and, if not, are the advantages in sample size enough to make up for the deficiencies in properties. Thus, it is of utmost importance that we understand the properties, and therefore limitations, of CVD graphene before we explore more complicated experiments. Several of these were hinted at in the previous chapters, including the polycrystalline nature of CVD films (section 2.3), which we will explore in greater detail here.

In this chapter we will first discuss the process of synthesizing graphene on Cu and subsequently transferring the film to an arbitrary substrate. Despite the simplicity of this method, a great deal of control is available to the user. For example, slight changes in things as mundane as the H_2:hydrocarbon ratio can lead to drastic changes in the size and structure of graphene gains. After detailing the growth parameters, the resulting structures will be presented. Specifically, we will address how average grain

size can be increased and the general types of grain boundaries that exist in CVD graphene films. Immediately after, we will try to understand how these differences affect the electrical quality of these films. This section, which is largely adapted from a paper to which I was a contributing author, will address the question as to whether or not the defects and grain boundaries present in typical growths are detrimental to the performance of CVD graphene devices. Lastly, we will present the work I completed with C. S. Ruiz-Vargas on the integration of these growth techniques with standard thin-film methods. This research simplifies the processing that is required to make truly wafer-scale graphene, as well as eliminates the need for a cumbersome transfer step. Much of the final section is adapted from Ref. 14.

3.2 | Synthesis and Transfer of Cu-Catalyzed CVD Graphene

In Section 1.3 we presented the general method of synthesizing graphene using a CVD process. While several metal catalysts were mentioned, throughout the rest of this work we will be utilizing copper as our growth substrate. This is primarily due to our desire to focus on monolayer graphene on a larger-scale, but also because the experimental setup requires common, inexpensive lab equipment and uses easily purchased Cu foils[1]. The basic process using Cu is shown in Figure 3.1a below, however growth on Ni is similar[2]. Growths are typically performed on 99.8% Cu foils ~25 μm thick. Prior to graphene growth the native Cu oxide is removed using a combination of etching and/or exposure to a reducing environment of H_2 while heating to ~1000 ºC. Methane (or another carbon source) is then introduced at the reaction temperature leading to a catalytic decomposition of the source gas and the formation

of a graphene sheet. Owing to the requirements of a clean Cu surface, and the low solubility of C in Cu[3], this process is largely self-limiting, yielding monolayer graphene sheets on the vast majority of the Cu surface. More recent studies have shown that the structural nature of these sheets can be further tailored by careful control of both the reactor pressure, as well as the various gas flow rates. This therefore allows experimentalists to modulate the graphene grain sizes and interactions, as will be discussed in more detail below. After the growth, the presence of graphene is verified using Raman spectroscopy and, in the case of partial growths, SEM imaging.

Once the desired synthesis is complete, the graphene can be easily removed from the Cu surface by a number of techniques. Typically, a supporting layer of PMMA or other polymer support is deposited onto the graphene and the Cu is wet etched from the back (see Figure 3.1b for an example using PDMS). This etch is commonly either a dilution of iron (III) chloride ($FeCl_3$) or ammonium persulfate ($(NH_4)_2S_2O_8$) in water, followed by a rinse in deionized water. While $FeCl_3$ has been the most popular method, recent work has found that $(NH_4)_2S_2O_8$ results in cleaner sheets[4]. To further eliminate such contamination, other cleaning steps can be performed on the PMMA/graphene stack. Popularly, a dilute standard clean 2/standard clean 1 (SC2/SC1; also known as an RCA clean but in reverse) sequence can be used[5]. In this case, the SC2 consists of a 20:1:1 mixture of water:ammonium hydroxide (NH_4OH):hydrogen peroxide (H_2O_2) and is performed at room temperature for ~15 minutes. The SC1 step is similarly performed but with hydrochloric acid (HCl) as opposed to NH_4OH. These etches help eliminate metal nanoparticles as well as less

stable organic molecules, cleaning the surface of the graphene. When combined with a thorough cleaning of the target substrate, this method can yield large arrays of devices with a relatively uniform Dirac point voltage (V_{Dirac}) distribution. While these steps are compatible with pure graphene, if other compositions are being investigated one must take care to confirm their stability in these chemicals. This is particularly important if multiple 2D materials are being used, where each etch process must be compatible with everything present.

The cleaned PMMA/graphene stack can now be transferred to the desired substrate. Due to the hydrophobicity of PMMA (495k in anisole), it is known that the PMMA side is always on top when floating on water. This allows experimentalists to scoop out the film onto their target. After thorough drying, the PMMA can be removed using a standard acetone/isopropanol (IPA) wash sequence. This technique is versatile, and is used to deposit graphene on a huge number of different types of substrates, including Si/SiO_2 wafers, TEM chips with and without silicon nitride membranes, and flexible plastics. The downside, unfortunately, is that there is quite clearly a strong capillary force that is exerted on the film as the acetone/IPA dries. Although this does not usually effect the integrity of supported graphene layers, it can be detrimental to the yield of suspended sheets. Critical point drying has been successfully employed[6], however currently the preferred method is to merely burn off the PMMA in a calcination procedure[7]. Using this procedure, researchers are able to selectively remove the PMMA and related residue in a more gentle way, greatly increasing sample yield.

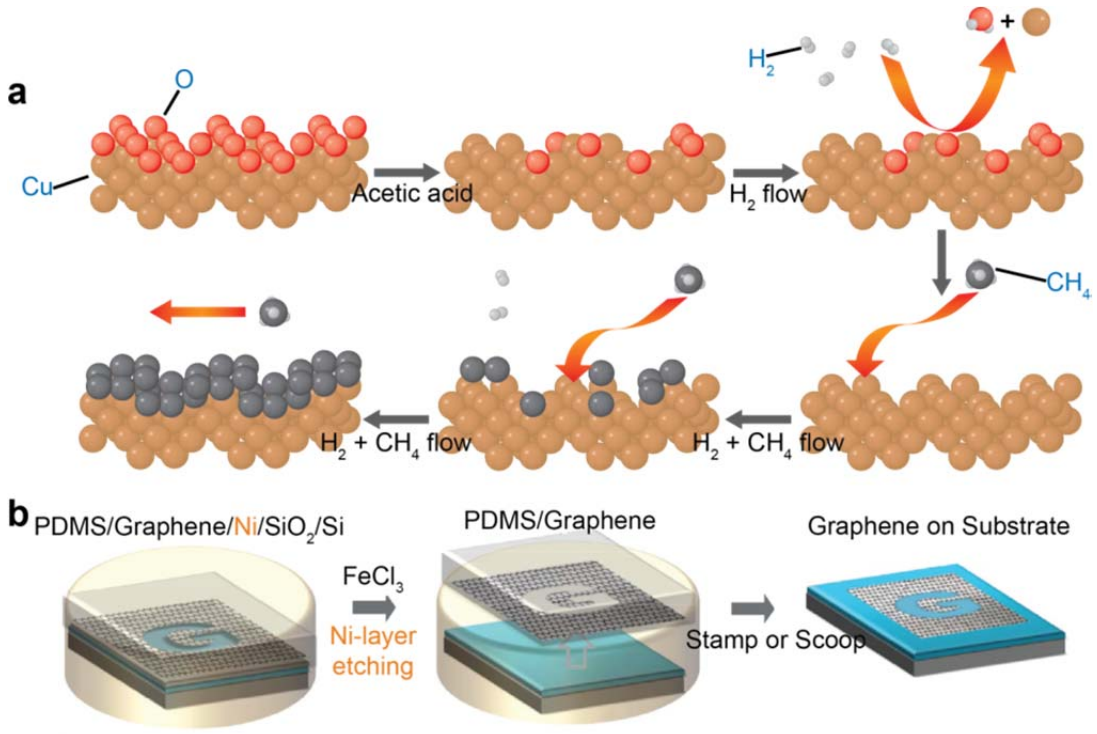

Figure 3.1 | CVD synthesis of graphene on Cu and transfer methods. a, Cu oxide is removed in a reducing environment in order to expose the bare Cu surface. A carbon source is then introduced at a high temperature, leading to the decomposition of the source and formation of graphene on the Cu surface. Reproduced from Ref. 14. **b**, Example of a transfer technique. Typically a polymer support layer, here PDMS, is deposited on the top graphene surface. This stack is then released after etching the catalytic metal layer. Finally, the target substrate is used to scoop out the polymer/graphene stack, after which the support layer is removed. Modified from Ref. 2.

3.3 | Altering the Structure of Graphene Sheets

In order to understand the macroscopic properties of any material, it is imperative that one knows the precise structure of what is being studied. In the case of CVD graphene this is even more important, as the qualities of these sheets rarely matched those of exfoliated samples. The first report of growth on Cu merely presented electrical data and Raman maps which, while they confirmed the presence

of graphene, did not provide any insight as to why their results deviated from those of exfoliated sheets. Although it was commonly suggested that the resulting films are likely polycrystalline, experimental confirmation of this was only recently reported. Using the DF-TEM technique discussed in 2.3, researchers were able to rapidly map out the grain structure of CVD graphene films—definitively proving that the resulting sheets are polycrystalline[7]. Notably, the grains of these films were small, on the order of a few micrometers. Consequently, a large number of grain boundaries existed in these growths, breaking the lattice periodicity of the film. This finding thus opened up two potential future routes: (1) exploiting DF-TEM as a feedback tool for investigating the growth of CVD graphene films—enabling tailoring of their grain size and structure—and (2) using these images to help study the effects of grain boundaries on the electrical properties.

Controlling Grain Shape and Size

Intuition states that growing macroscopic monocrystalline sheets of graphene is the ideal situation, and as such many recent studies have focused on these efforts. Through this work, reports have shown that it is possible to synthesize films with single grains up to hundreds of microns—or even millimeters—in size[8–10]. The reasons for this are beginning to be understood, as researchers have empirically found that the H_2:hydrocarbon (C_xH_y) ratio[11], the overall system pressure, and the presence of oxygen are critical in determining the grain structure of graphene films. These parameters have direct influence over the nucleation density, thus influencing the maximum grain sizes[10].

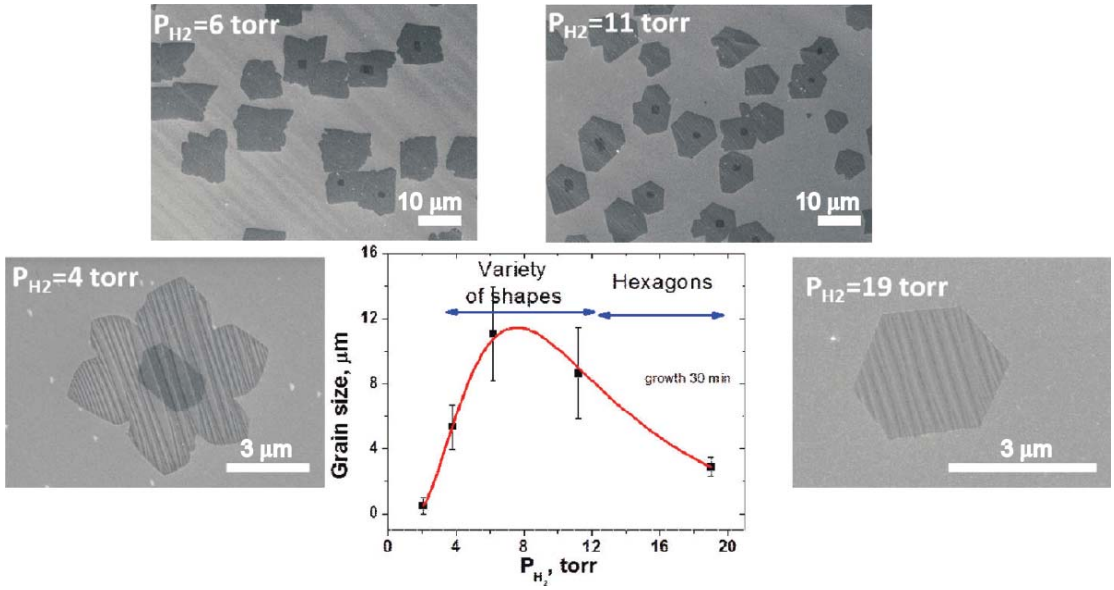

Figure 3.2 | Role of hydrogen in graphene growth. As the partial pressure of H_2 is increased, the etch rate of the graphene nucleation sites is altered. When the H_2:hydrocarbon ratio is carefully controlled graphene islands form in hexagonal shapes—typically indicative of single crystal domains. Reproduced from Ref. 11.

H_2 gas has several important roles in the CVD graphene process. The gas not only acts as the reducing agent for the Cu native oxide, but it also acts as an effective O_2 scrubber by reacting with rogue molecules to form H_2O and prevent burning of the graphene sheet. It is also known that H_2 can etch graphene at a much more controllable rate than O_2, and thus the nucleation and growth rate of graphene crystals can be altered by carefully controlling the H_2:C_xH_y ratio. As demonstrated in Figure 3.2, this can then cause graphene islands form in nearly perfect hexagons—which is usually indicative of single crystals (slight defect shapes can be polycrystalline, however, see Figure 3.4b). Furthermore, this behavior has been observed at both ambient and low pressures, suggesting that it is a general mechanism that is broadly applicable. Unfortunately, this procedure does not provide much control over the

density of graphene nucleation sites, which in turn places an inherent limit on the size a grain. Therefore while changing the H_2:hydrocarbon ratio grants some control over the shape of individual crystals, it is not sufficient for maximizing domain size.

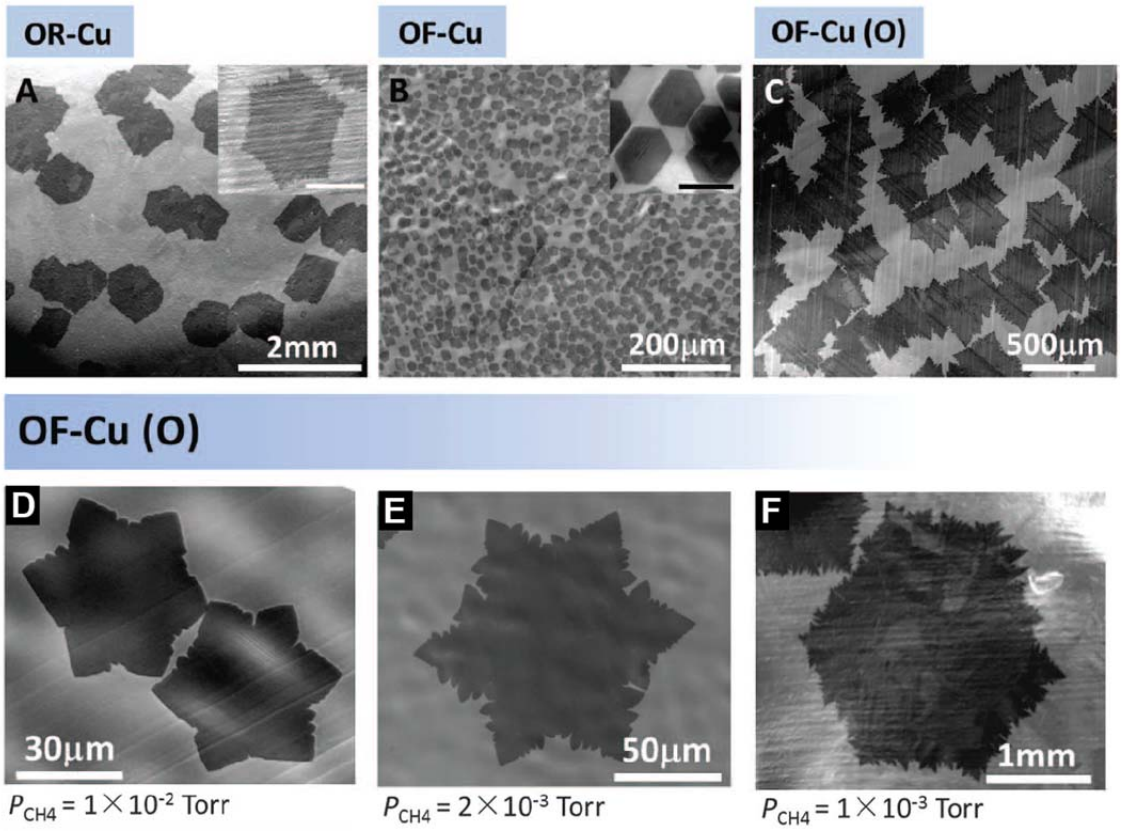

Figure 3.3 | Role of oxygen and hydrocarbons in graphene growth. a-c, Graphene domain sizes vary strongly as a function of surface O concentration, decreasing from mm scale on oxygen rich Cu (OR-Cu), to 100s of μm on O exposed oxygen free Cu (OF-Cu (O)), down to micron-scale grains on OF-Cu. **d-f**, Grain shape changes strongly as a function of the partial pressure of hydrocarbon source, approaching a hexagonal structure—consistent with Figure 3.2. Modified from Ref. 10.

More recent experiments have shown that this nucleation density is reliant on the presence of oxygen on the surface of the Cu substrate[10]. The presence of O atoms suppresses the exposed active sites where graphene can nucleate, thus promoting growth at islands that have already started to form. As we have just discussed the role

of the H_2:hydrocarbon ratio in synthesis, clearly a balance must be struck between the presence of H, C, and O atoms in order to provide complete control over grain size and shape. If these ratios are carefully tuned, however, one can promote the synthesis of large (mm scale) polygonal graphene domains, as is shown in Figure 3.3.

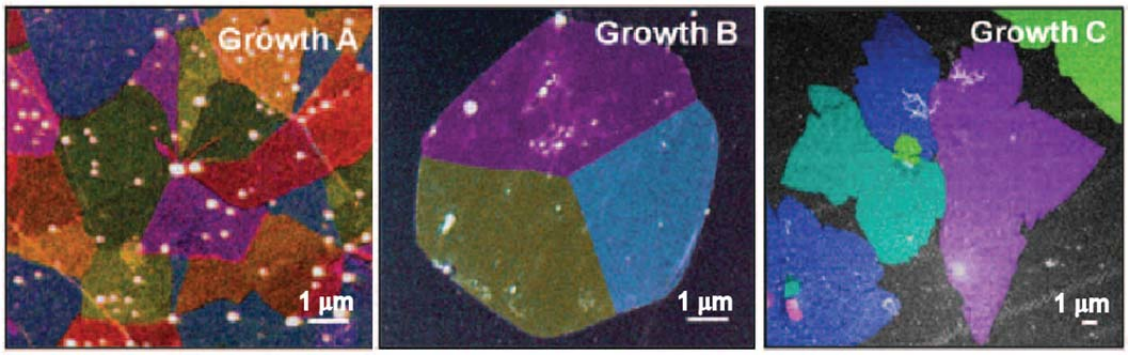

Figure 3.4 | DF-TEM images of increasing grain size. Changing the reaction parameters can have a strong influence on the grain shape and size. Growth A (left) was synthesized in a highly reactive environment (surplus of reactants), yielding grains ~ 1μm. Growth B (middle) utilized conditions similar to those shown in Figure 3.2, however this grain is polycrystalline—emphasizing the importance of verification under DF-TEM images. Growth C (right) was performed using the "pita pocket" method, resulting in the largest grains, ~50 μm. Modified from Ref. 12.

Continuity in Graphene Sheets

Although the previously discussed method facilitates the formation monocrystalline graphene islands that are extraordinarily large[9,10], grain size is not the only important factor. As many applications require a continuous sheet of graphene, how these grains come together is also important to understand. Perhaps surprisingly, however, when trying to maximize individual grain size, we have found that they do not seem to coalesce in a uniform fashion—with gaps existing even for very long growths. This suggests that a more reactive environment is needed in order to promote intergrain stitching (Figure 3.4a)[12]. In order to mitigate the negative effects of gapped

grains while maximizing the positive aspect of large crystals (the details of which will be discussed in the following section), some scientists have proposed a two-step mechanism to form complete sheets whereby large grains are grown in a low pressure environment followed by exposure to a large amount of reactants.

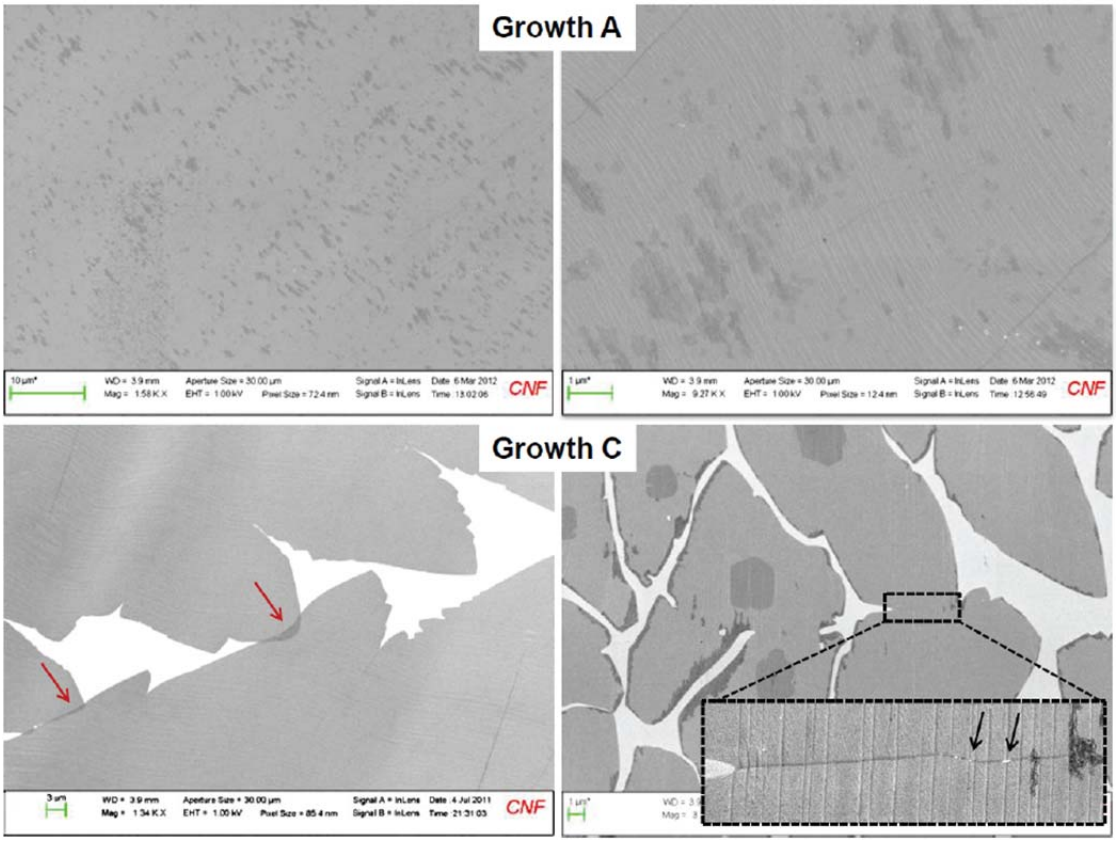

Figure 3.5 | SEM images of different types of grain boundaries. Growth conditions can affect grain boundary formation as well as domain size and shape. For Growth A, the Cu surface is completely covered, however Growth C has many gaps and overlaps. The lower right image shows that even areas where two domains appear to come together cleanly show overlapped (darker) and gapped (bright) "grain boundaries" under higher magnification (inset). Modified from Ref. 12.

3.4 | Influence of Structure on Electrical Properties

As suggested in 3.3, the general motivation towards increasing graphene grain size was largely because it seemed intuitively obvious that reducing the amount of

grain boundaries would correspond to an improved electrical performance. This conjecture, however, was not supported by macroscopic experimental results. In fact, the first DF-TEM paper showed almost no correlation with carrier mobility and grain size[7]. This was later supported by macroscopic studies on large grains, where mobility values showed nearly the same spread for graphene domains of 6 μm versus 20 μm[8]. From these findings it was clear that the influence of individual grains on the electrical properties of whole sheets was not well understood. In order to determine whether or not it is worth the effort of synthesizing larger grains, it is critical to identify the role of individual grain boundaries in device performance. In this section we will summarize work that was done by our group towards isolating this contribution and understanding the impact they have on large-scale devices. All figures in this section are reproduced or modified from Ref. 12.

Types of Grain Boundaries

One of the most important findings of this work is that not all grain boundaries are identical. This study found that the way graphene films come together is highly dependent on the growth conditions of the sheet, and that environments that yield larger individual grains are counterproductive in terms of forming a continuous sheet of graphene. When two domains meet under low reactive conditions (deemed "Growth C," see Figure 3.4c), we discovered that the grains either overlap or leave a gap behind. While some gaps/overgrowths may be obvious under lower magnification images, the lengthscales can often approach the tens of nanometers, making such interfaces seem like well-stitched boundaries. This is vastly different from growths

performed with a surplus of reactants ("Growth A," see Figure 3.4a), where these domains formed traditional grain boundaries, similar to those shown in Chapter 2. This is shown most clearly in the SEM images presented in Figure 3.5. The top half of the image shows a Growth A sample, where the sheet completely covers the Cu surface. The slightly darker regions are most likely bilayer or small wrinkles in the film, but no distinctive gaps are seen. This is in stark contrast to Growth C shown in the lower half. Here there are clear boundaries where the grains refused to come together, and a few places where they continued to grow over/under one another. The zoomed-in portion shows an example of a region that appears to be a homogenous grain boundary that is in fact a combination of gapped and overlapped regions.

Interestingly, we also found that even geometric shapes of graphene islands can have multiple grain boundaries within them (see Figure 3.4b). This is important to note, as previous studies used this characteristic as an indication of single crystal islands[13]. The evidence shown in this study, however, emphasizes the importance of characterizing these films under DF-TEM, or some other similarly definitive measurements.

Cross-Domain Measurements

Due to the major differences in these three types of grain boundaries—continuous, gapped, and overgrown (see Figure 3.6d)—it seems clear that they will have different influences on the electrical integrities of devices. In order to investigate this directly, Tsen *et al.* fabricated custom TEM chips with alignment marks on a supporting SiN_x membrane. The location of grain boundaries could then be

determined by combining DF-TEM data with the known alignment marks. Afterwards, electron-beam lithography was used to locally define transistors that contained precisely one grain boundary of known type. These devices were next investigated using four-terminal measurements, as is shown in Figure 3.6.

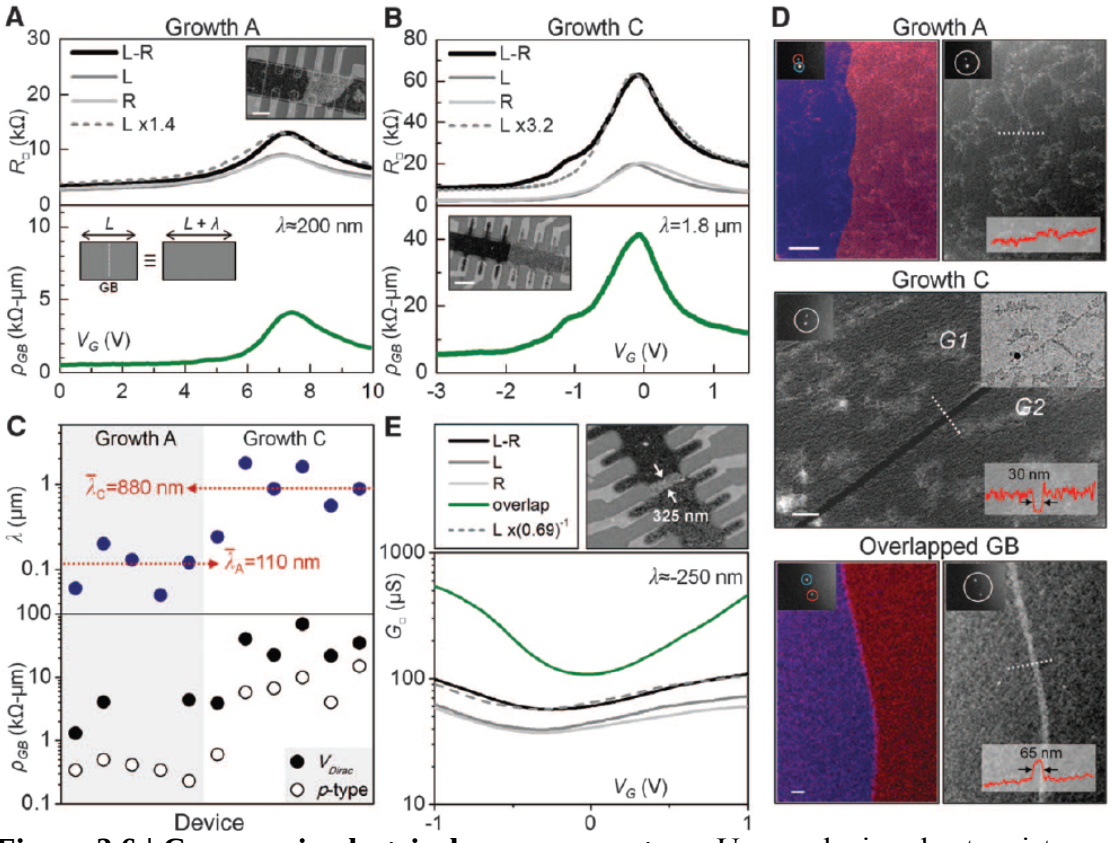

Figure 3.6 | Cross-grain electrical measurements. a, Upper: device sheet resistance ($R_{\square}$) crossing a single grain boundary from a Growth A synthesis. Lower: Extracted grain boundary resistance (ρ_{GB}) as a function of gate voltage (V_G). The grain boundary is found to effectively extend the channel length (λ) by ~200 nm at all V_g. **b**, Measurements for a gapped growth C boundary. The extracted λ here is ~1.8 μm, indicating these types of boundaries are much more resistive. **c**, Distribution of extracted λ and ρ_{GB} for growths A and C. Boundaries from growth C are nearly ten times worse than those from growth A. Scale bars are all 1 μm. **d**, DF-TEM images of grain boundaries from growth A and C. Growth A (upper) exhibits better stitching than growth C, which shows both gapped (middle) and overlapped (lower) junctions. Scale bars are all 100 nm. **e**, Measurements of an overlapped region shows an effective shortening of the channel, leading to a negative λ (-250 nm).

Our experiments found that all three types of graphene grain boundaries act as an effective change in the length of the conducting channel, thus affecting the resistance of the device. This value is deemed $\lambda = \rho_{GB}/\rho_{\square}$, where ρ_{GB} is the grain boundary resistance and $\rho_{\square}$ is the sheet resistance of the pure graphene grain. Thus, when a grain boundary is present in a device with length L and width W, the intrinsic resistance is altered from $R = \rho_{\square}(L/W)$ to $R' = \rho_{\square}(L + \lambda)/W$. Surprisingly, we found that each type of grain boundary has a different characteristic length-scale for this adjustment (see Figure 3.6c). We determined that well-formed grain boundaries contributed a modest ~100 nm increase in channel length, whereas gapped junctions exhibited effective increases of nearly 1 μm. Contrary to this, overlapped grains led to an effective "shortening" of the device channel, leading to lower-than-expected resistance values. Our findings thus provided detailed insight into the precise engineering of graphene-based electronics by demonstrating the importance of grain boundaries versus crystal size.

Macroscopic Implications

Although it is clear that electronic devices fabricated from single grains of graphene will perform the best, our results proved that the presence of well-stitched grain boundaries may not significantly degrade the overall quality of the device. It thus follows that highly-reactive growths may be preferred to larger grain growths, as resulting device arrays will show a greater degree of uniformity. This is due to the fact that, while there may be fewer boundaries in these larger growths, their impact is significantly higher—especially at typical device sizes (~5 μm; see Figure 3.7a). In

order to investigate this, we generated a large array of more macroscopic devices using highly-polycrystalline sheets (grain sizes < 5 μm), which we show in Figure 3.7b.

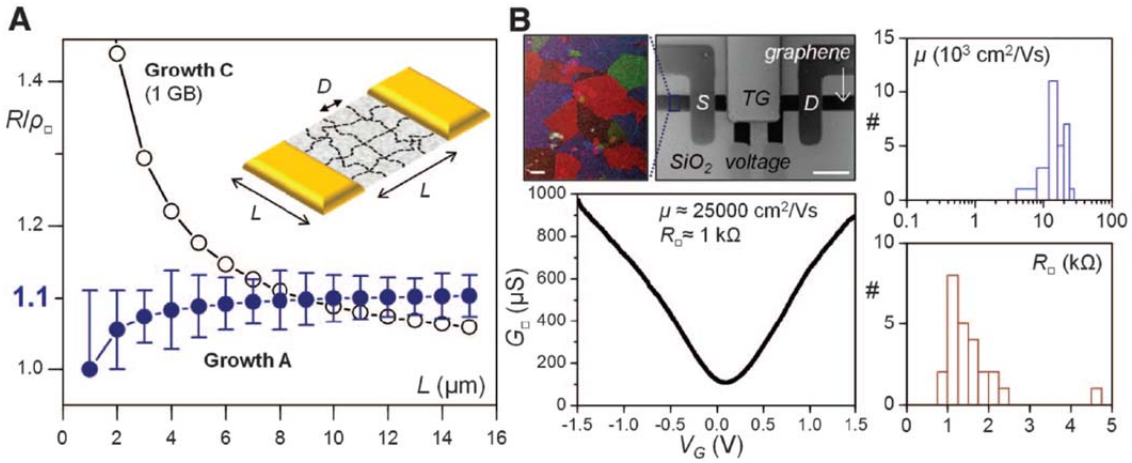

Figure 3.7 | Effect of grain boundaries on macroscopic devices. a, Resistance as a function of channel size (*L*) for both A and C growths. The effect of one grain boundary on devices made from growth C causes large changes in device resistance, whereas growth A (with expected number of grain boundaries) displays uniform performance for many different sizes. **b**, Top left: DF-TEM of growth used in the device shown in the SEM image. Bottom left: Gate dependence shows high carrier mobility and low resistance—comparable to exfoliated samples. Right: Histograms of low field-effect mobilities (upper) and *p*-type sheet resistance (lower) for 28 similarly fabricated devices. Both show narrow distributions with excellent values.

Despite the large number of expected grain boundaries in a given device (~5-10), the array exhibited high mobilities (> 10,000 $cm^2V^{-1}s^{-1}$) as well as narrowly distributed resistance values (see Figure 3.7b, right panels). Since sheets synthesized in this manner can also be generated more quickly and easily (as opposed to large-grain growths), there are very few downsides in utilizing such films. In this thesis we are primarily concerned with the modification or control of the macroscopic chemical properties of graphene and, for these reasons, throughout the rest of this thesis all

graphene growths are performed in highly reactive environment.

3.5 | Towards Transfer-Free Growths

The synthesis of graphene on Cu foils has proven to be enormously influential on the field of graphene research—enabling such studies as the one just presented, as well as numerous large-scale and/or destructive experiments. Despite this, the integration of graphene films with conventional fabrication methods is hindered by the transfer step that is required in order to move the sheet onto the desired substrate. This step requires a moderate degree of manual skill, and is therefore problematic to automate. In order to combat this, we have demonstrated a new method utilizing thin films of Cu catalyst, eliminating the need for the conventional wet transfer, greatly improving the synergy of this method with procedures used in thin-film processing[14].

Prior to this work, using these graphene materials for device applications often required a transfer step because the growth substrate is not compatible with device fabrication procedures. Unfortunately, this extra transfer step for depositing synthesized graphene onto the device substrate can cause a number of significant problems. First, the mechanically delicate single layers can be damaged during the transfer. Second, the alignment between the graphene film and the target substrate presents additional technical challenges. Third, these transfer procedures are often performed in aqueous solutions and it is difficult to remove the liquid residue trapped within the interfacial space between graphene and the target substrate.

Here we discuss a new technique for producing large scale (> 1 cm) single layer graphene (SLG) and fabricating transistor arrays with uniform electrical

properties directly on the device substrate. While the basic mechanism is similar to the one recently reported by Li *et al.*[1], we use an evaporated copper film instead of a copper foil. This is a significant technological improvement and allows us to directly fabricate uniform transistor arrays without a transfer process. This finding leads to a low device failure rate (< 5%) and uniform electrical properties. We determined several key characteristics from our SLG devices including (1) a good carrier mobility, (2) mechanical and electrical continuity over a large distance (> 0.5 mm), and (3) current saturation and a promising transconductance (~ 8 μS/μm). Furthermore, our technique is easily scalable to larger dimensions, limited only by the size of the substrate and growth chamber, and is compatible with conventional thin film technologies.

Substrate and Initial Characterization

Our growth substrate is a copper film of varying thickness with a thin Ni adhesion layer, both directly evaporated onto a silicon wafer covered with 285 nm of thermal oxide. Before graphene growth, strips of the wafer are cleaved and then immersed in acetic acid at 35 °C for 10 minutes in order to remove most of the copper oxide[15]. Even though the copper oxide would be stripped under the reaction environment, removal prior to growth eliminates the need for a lengthy anneal which can deteriorate the quality of the copper film. The actual synthesis largely follows the procedures outlined in Section 3.2, however methane is introduced immediately upon reaching the reaction temperature. After ~10 minutes of growth the substrates are then cooled for characterization. We found that one of the key variables is the thickness of

the Cu film. While graphene grows continuously on Cu films thicker than 500 nm, poor film quality at high temperatures for thinner Cu films prohibits such growth. Below, we use 500 nm thick Cu as our growth substrate. Ni was added as an adhesion layer for subsequent fabrication procedures, which does not affect the quality of the grown graphene as confirmed by Raman spectroscopy.

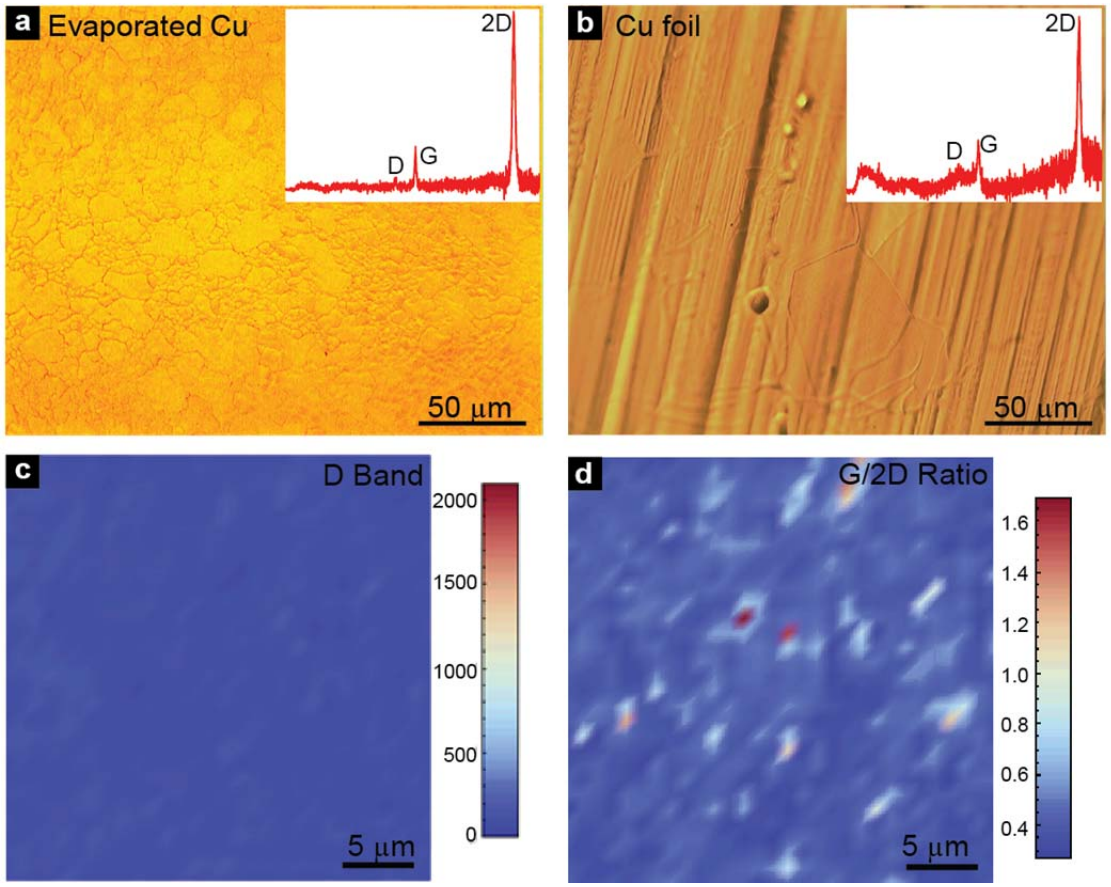

Figure 3.8 | Growth of graphene on Cu thin films. a, Cu thin film and **b**, Cu foil contrast enhanced optical images (100x, NA = 0.9) of typical samples after synthesis of graphene. Copper oxide is present at grain boundaries if care is not taken to etch it before growth. Insets: representative Raman spectra of substrates after growth (Cu background subtracted). **c**, Map of the D-band intensity of a graphene sample (grown on Cu thin film) transferred onto a Si/SiO_2 substrate. The signal is uniformly low, indicating high quality graphene. **d**, Map of the G/2D ratio for as grown graphene, which suggests at least 93% single layer graphene coverage.

Figure 3.8a shows a contrast enhanced brightfield image of a typical sample substrate after growth. Despite the presence of grains which are smaller than those found on Cu foils, we find that graphene is continuous across these visible Cu features as confirmed by Raman and electrical measurements (see below). The inset to Figure 3.8a presents a Raman spectrum that is representative of the grown graphene. A single symmetric 2D peak (full width at half maximum ~ 36 cm^{-1}), a small G/2D ratio, and a small D peak are observed, which strongly suggest that our graphene is a single layer and the quality of the sheet is not significantly affected by the visible features of the Cu film[16]. The growth of SLG was further investigated via spatially resolved two-dimensional Raman spectroscopy. Figure 3.8d shows a map of the Raman G/2D ratio which exhibits consistently small values (0.40 ± 0.06) except for a few localized spots. From a histogram of the G/2D ratio we estimate the SLG coverage to be a minimum of 93%. The counts for the D peak were universally low (Figure 3.8c) and did not present any visible structures, which is consistent with high quality graphene synthesis. We note, however, that if care is not taken to strip the oxide beforehand, or if a slight leak into the reaction chamber is present, the quality of the SLG is reduced considerably. If this step is taken, virtually no difference in film quality (as determined by Raman spectroscopy) is observed between graphene grown on a Cu thin film versus on a Cu foil (see Figure 3.8b).

Transfer-Free Fabrication

Our SLG uniformly grown on a Cu coated Si wafer substrate allows the fabrication of a large scale device array with a simple photolithography process. A

schematic of our device fabrication method is shown in Figure 3.9a. Our device design consists of two large pads connected by a thin strip, patterned using standard photolithography techniques. The photoresist covering the devices acts as a protective layer for the remaining processes. Sample substrates are subjected to a brief (30 s) oxygen plasma etch in order to remove unwanted photoresist residue and graphene.

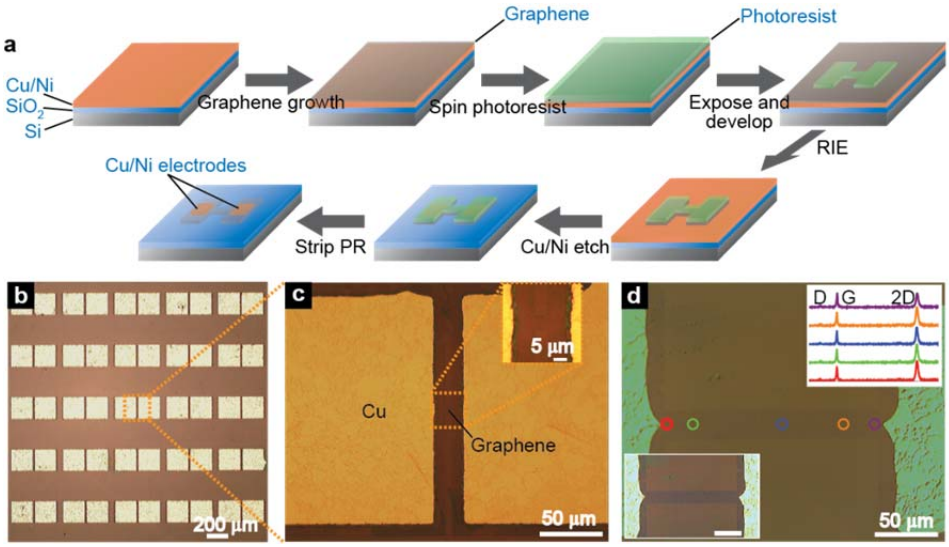

Figure 3.9 | Fabrication of SLG device array. a, Schematic of device fabrication procedure (see main text for details). **b**, 5x brightfield optical image of a typical sample substrate after fabrication. **c**, 50x brightfield image of the same sample. Graphene connecting the copper pad is just visible (boxed). Inset: 100x image of the device channel. **d**, 50x Differential interference contrast image of a longer device. Upper inset: Raman spectra across the length of the graphene strip are highly uniform. Lower inset: 20x brightfield image of the sample. All brightfield images have been contrast enhanced.

Whole samples are then exposed to a continually refreshed etch solution long enough to remove the Cu/Ni in the unprotected areas and beneath the connecting photoresist/graphene strips. This results in two large pads of SLG/Cu/Ni connected by a narrow channel of SLG all protected by photoresist. Lastly, the photoresist is stripped leaving the graphene channel resting on the substrate connected to the two

pads. We find that the order of the last two steps is important. If the photoresist is instead removed first, extensive damage of the graphene sheet can occur. One must also take care to remove the photoresist correctly, as not doing so can leave behind a layer of photoresist residue, hardened by the plasma etching step.

Our fabrication process simultaneously produces a large array of devices. Figure 3.9b shows the optical image of the resulting array where each pair of pads forms a single SLG device. A zoomed-in image of one device is shown in Figure 3.9c which exhibits a clear undercut around the edges of the Cu/Ni as well as the intact SLG channel (more clearly visible in the inset). The differential interference contrast image of a long SLG channel is also provided in Figure 3.9d. Here it confirms that the surface of the device channel is very clean without any visible residue underneath it, an important improvement over devices produced by a wet transfer process. Significantly, the resulting graphene channel has a uniform Raman signature even over large areas, as shown in the upper inset of Figure 3.9d.

One key advantage of our fabrication process described above is its high yield and uniform electrical properties. In order to show this we fabricated 95 devices on a single substrate over a large area (~ 3×6 mm) with varying channel length and width (see Figure 3.10 caption). A device schematic is shown in Figure 3.10a. Only 3 out of 95 devices are visibly broken (example shown in the inset of Figure 3.10c). All other devices were conductive, representing a 97% success rate. Two terminal resistance measurements showed that nearly 80% of conducting devices have resistances of less than 10 kΩ, as can be seen from the cumulative probability plot for device resistance (Figure 3.10c). In addition we observe that median device resistance (R_{median}) increases

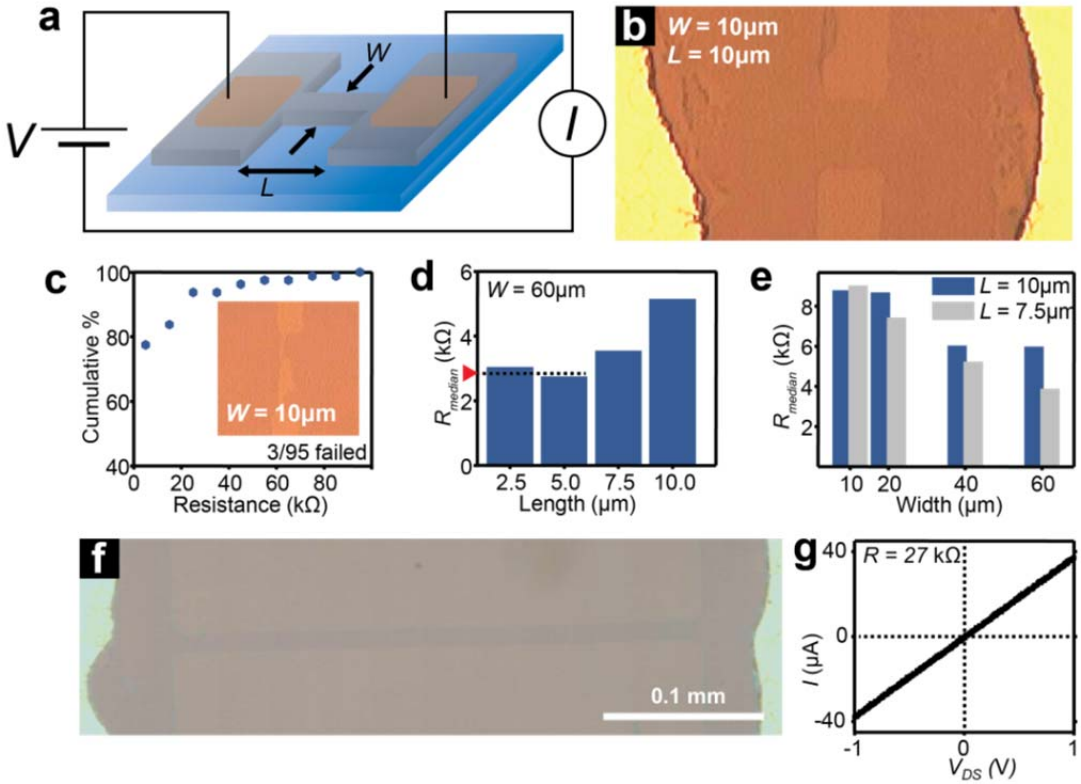

Figure 3.10 | Electrical characteristics of SLG devices. a, Schematic of device, with patterned Cu/Ni electrodes contacting graphene from below. **b**, Optical microscope image, taken with a 50x objective, of a SLG graphene device (width (W) = 10 μm, length (L) = 10 μm). **c**, Cumulative probability plot of device resistance. 97% of the devices were found to be conductive, and 80% were found to have resistance less than 10 kΩ. Inset: Broken device, likely damaged during photoresist stripping. **d**, Median resistance (R_{median}) for those devices with R_{median}< 10 kΩ, as a function of length (W = 60 μm). **e**, and as a function of width for L = 10 μm (blue) and 7.5 μm (grey). **f**, Optical image, taken with a 20x objective, of a ~0.33 mm long SLG device and ~10 μm in width. **g**, Even though length of this graphene strip is at least an order of magnitude greater than the typical grain size in the evaporated copper film, this device exhibits high conductance, with R =27 kΩ.

with increasing channel length and decreasing channel width (Figure 3.10d and 3.10e). From these we estimate the sheet resistivity of our SLG to be 25 kΩ with total contact resistance on the order of 3 kΩ (denoted by an arrow in Figure 3.10d). Remarkably, we find that our process allows the fabrication of devices with much longer SLG channels (as long as 0.5 mm). One device with a 0.33 mm long channel (fabricated

from a different batch) is shown in Figure 3.10f, which has an exceptionally low two terminal resistance of ~27 kΩ.

The uniform Raman features shown in Figure 3.9d and the high yield of conductive devices discussed above is consistent with continuous growth of SLG over a large area. We also note that the dimensions of the devices studied above far exceed the typical feature size visible in Figure 3.8a. Therefore our SLG allows fabrication of more complicated devices with uniform performance characteristics over a large area, a key step towards integrating graphene into existing technology.

Device Arrays

We can utilize this method for large-scale integration, which we demonstrate in Figure 3.11, where we show an array of field effect transistors fabricated with our SLG. Each transistor has an individually addressable top gate electrode made with Cr(5 nm)/Au(45 nm) defined on top of 100 nm thick film of SiO_2 gate oxide (evaporated directly onto SLG). A close up image of the SLG channel with the top gate (TG) is shown in Figure 3.11a with a schematic cross section of the device.

In Figure 3.11c, the low bias conductance, g_{DS}, as a function of the top gate bias (V_{TG-S}) measured from one of our devices is shown. The minimum conductance was observed near V_{TG-S} = 0.5 V, which corresponds to the Fermi level being at the Dirac point of the SLG. The electron mobility was estimated to be approximately 700 $cm^2/(V \cdot s)$ using $1/C_{TG}*(dg_{DS}/dV_{TG-S})$, where C_{TG} is the top gate capacitance. The true value can be larger if we consider the fact that the actual top gate capacitance tends to be smaller than the ideal value of 34.5 nF/cm^2 for 100 nm SiO_2 used in our estimate.

Unlike in our topgated devices, we observe that the device conductance show much weaker backgate dependence.

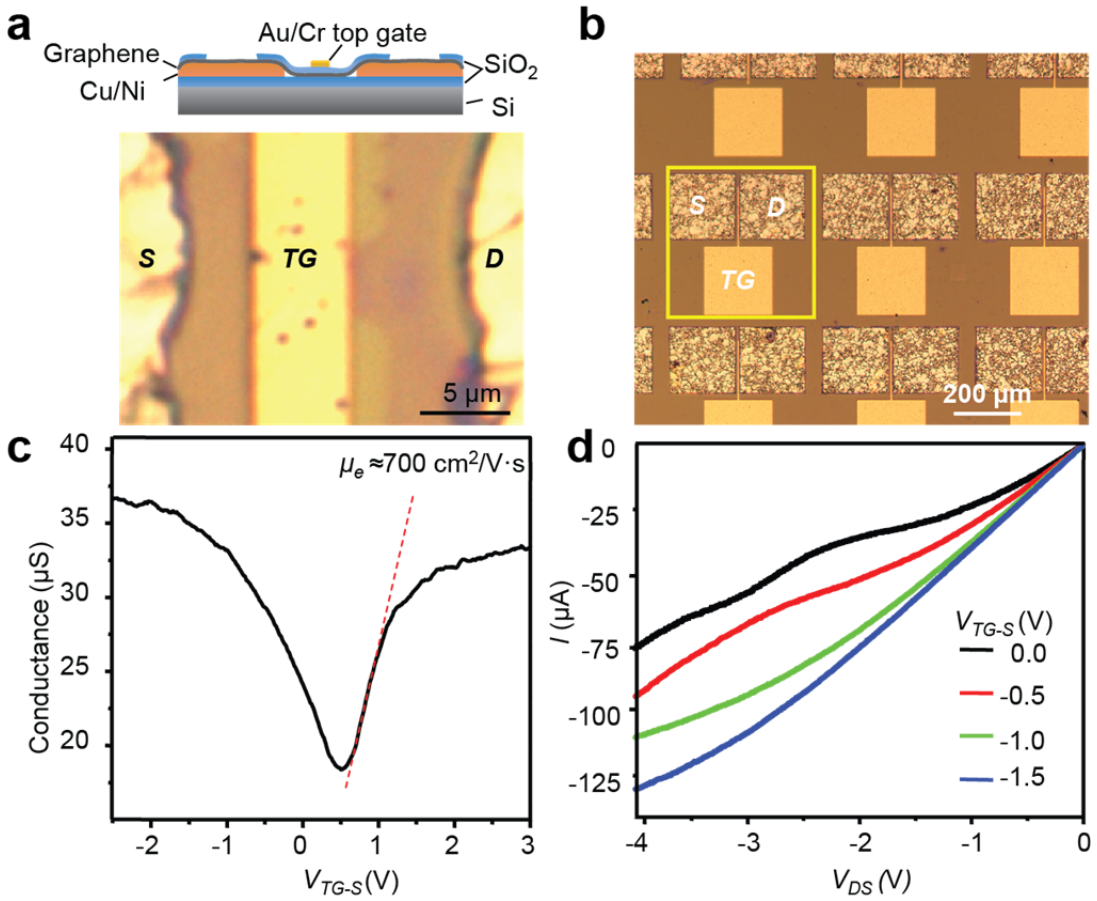

Figure 3.11| Gate dependence of SLG transistors. a, Top: Cross view schematic of top gated SLG transistor. Bottom: Optical image of the top gated (*TG*) graphene channel, taken with a 50x objective. **b**, Large area view of a region arrayed with SLG transistors in a top gate geometry. **c**, Gate dependence for representative device with an electron mobility (μ_e) of ~700 $cm^2/V{\cdot}s$ for V_{DS}=100 mV. **d**, Saturation current observed for negative *DS* bias (V_{DS}), and a transconductance of ~8 μS/μm.

While this mobility value is significantly smaller than the one reported by Li *et al.*[1], it is smaller by only a factor of two in comparison to the mobility reported for exfoliated graphene used in a similar device geometry by Meric *et al.*[17]. The latter study also showed current saturation and a large transconductance, a key characteristic

for many RF and high power device applications. Surprisingly, we observe similar current saturation from many of our devices at relatively low V_{DS}. Data from the same device in Figure 3.11c is shown in Figure 3.11d. As we decrease $V_{TG\text{-}S}$, regions of current saturation become more prominent with a transconductance of at least 8 μS per 1 μm of channel width. Use of a thinner (20 nm) and more efficient gate oxide, such as HfO_2, can thus increase the transconductance by a factor of 20. Considering this, the transconductance from our device could be comparable to the best value reported by Meric *et al*.

We again note that the SLG synthesis and device fabrication method discussed here is compatible with standard thin film technologies and does not involve any nonconventional and delicate steps such as liquid based transfer. Thus it can allow SLG to be integrated into large scale electronics circuitry with only minor steps that can easily be streamlined and automated. We anticipate that additional synthesis optimization and materials characterization will further improve already promising electrical and physical characteristics of large scale SLG.

3.6 | Summary

In this Chapter we introduced two major synthetic methods as well as the influence of growth parameters on the grain structure of the resulting graphene films. We found that by controlling the parameters carefully, it is possible to tailor the crystal domain size of graphene islands from hundreds of nanometers all the way up to hundreds of microns. We further delved into the impact that grain boundaries have on the overall qualities of graphene-based electronics, as well as how these influences are

related to the grain structures previously introduced. These experiments showed that, perhaps counter-intuitively, it may be preferred to synthesize graphene under reactive conditions, yielding highly polycrystalline sheets, as many well-stitched grain boundaries are in total better than one gapped junction. These techniques and developed expertise will be utilized in the following chapter, where we will now exploit the intrinsic chemical properties of graphene in new and unique ways.

REFERENCES

1. Li, X. *et al.* Large-Area Synthesis of High-Quality and Uniform Graphene Films on Copper Foils. *Science* **324,** 1312–1314 (2009).

2. Kim, K. S. *et al.* Large-scale pattern growth of graphene films for stretchable transparent electrodes. *Nature* **457,** 706–710 (2009).

3. Li, X., Cai, W., Colombo, L. & Ruoff, R. S. Evolution of graphene growth on Ni and Cu by carbon isotope labeling. *Nano Lett.* **9,** 4268–4272 (2009).

4. Lee, G.-H. *et al.* High-strength chemical-vapor-deposited graphene and grain boundaries. *Science* **340,** 1073–1076 (2013).

5. Liang, X. *et al.* Toward clean and crackless transfer of graphene. *ACS Nano* **5,** 9144–9153 (2011).

6. Zande, A. M. Van Der *et al.* Large-Scale Arrays of Single-Layer Graphene Resonators. *Nano Lett.* **10,** 4869–4873 (2010).

7. Huang, P. Y. *et al.* Grains and grain boundaries in single-layer graphene atomic patchwork quilts. *Nature* **469,** 389–392 (2011).

8. Li, X. *et al.* Graphene films with large domain size by a two-step chemical vapor deposition process. *Nano Lett.* **10,** 4328–4334 (2010).

9. Li, X. *et al.* Large-area graphene single crystals grown by low-pressure chemical vapor deposition of methane on copper. *J. Am. Chem. Soc.* **133,** 2816–2819 (2011).

10. Hao, Y. *et al.* The Role of Surface Oxygen in the Growth of Large Single-Crystal Graphene on Copper. *Science* **342,** 720–723 (2013).

11. Vlassiouk, I. V *et al.* Role of Hydrogen in CVD Growth of Large Single Crystal Graphene. *ACS Nano* **5**, 6069-6076 (2011).

12. Tsen, A. W. *et al.* Tailoring Electrical Transport Across Grain Boundaries in Polycrystalline Graphene. *Science* **336,** 1143–1146 (2012).

13. Yu, Q. *et al.* Control and characterization of individual grains and grain boundaries in graphene grown by chemical vapour deposition. *Nature Mater.* **10,** 443–9 (2011).

14. Levendorf, M. P., Ruiz-Vargas, C., Garg, S. & Park, J. Transfer-Free Batch Fabrication of Single Layer Graphene Transistors. *Nano Lett.* **9,** 4479–4483 (2009).

15. Chavez, K. L. & Hess, D. W. A Novel Method of Etching Copper Oxide Using Acetic Acid. *J. Electrochem. Soc.* **148,** G640 (2001).

16. Ferrari, A. *et al.* Raman spectrum of graphene and graphene layers. *Phys. Rev. Lett.* **97,** 187401 (2006).

17. Meric, I. *et al.* Current saturation in zero-bandgap, top-gated graphene field-effect transistors. *Nature Nanotech.* **3,** 654–659 (2008).

CHAPTER 4

TAILORING THE CHEMICAL STRUCTURE OF CVD GRAPHENE

4.1 | Doping Thin Films

Doping is the process of introducing intentional impurities into a semiconductor crystal. Controlling the density and type of these defect atoms, or dopants, yields a significant degree of control in terms of modulating the electronic structure of the semiconductor. By creating additional allowed states near the conduction (or valence) band, these dopants induce free carriers in the system. For silicon (Si), the most common dopants are boron (B), which yields holes (*p*-type), and phosphorus (P), which results in electrons (*n*-type). These atoms can be inserted into bulk Si systems via two major ways: dopant diffusion and ion implantation. Dopant diffusion is accomplished by enriching the solid Si environment with the dopant atom in solid liquid or vapor form. Heating this system then results in a slow movement of these atoms into the Si bulk. Ion implantation takes a starkly different approach, whereby dopant atoms are forcefully inserted into the Si crystal using an accelerated ion source. By controlling the energy of this beam, the penetration depth can be carefully tuned, providing a highly reproducible result. Through masks, etching steps, and other bulk techniques, these processes can be controlled in a spatial manner, thus enabling the rational production of various junctions—including *p*-*n* junctions which are critical in the formation of modern electronics.

When reducing this system down to 2-dimensions it becomes clear that these

industrial techniques are no longer easily applied. Ion implantation is known to cause a large degree of damage to thin sheets of carbon, whereas dopant diffusion is not possible due to the lack of a bulk mass. The importance of having this control, however, has catalyzed numerous studies which we will introduce and discuss in this chapter. We will first present the initial approaches researchers have taken towards doping graphene, including using surface adsorbates and reactions, as well as edge functionalization. These works laid the basis for our use of molecular chlorine as will be shown in the following section. Lastly, our efforts to introduce B as a substitutional *p*-type dopant will be described. This final work, when combined with a previously reported synthesis of Nitrogen (N)-doped graphene gives researchers powerful methods in customizing the chemical and electrical properties of graphene which will be fully exploited in Chapter 5.

4.2 | Prior Works: Surface Control and Edge Functionalization

Much work has been done towards controlling carrier type and density in isolated graphene. The vast majority of reported studies use the most direct method of electrostatic doping using gate electrodes. These electrodes can be either global back gates[1–3], any number of local top gates[4], or a combination of these two[5]. While this approach provides a great deal of precision and reproducibility, they inherently remove the 2-dimensionality of the material. Thus, although the information gleaned from these experiments is helpful in characterizing the behavior of these sheets, they also eliminate the advantage of having such a thin film. Further, changes under a gate bias are typically transient in nature, stressing the need for a more permanent solution.

In this section we will present some prior works that have attempted to solve this problem.

Molecular Adsorbates

Immediately after isolating graphene—whether exfoliated or CVD—external effects induce a significant degree of charge inhomogeneity. Trapped charges on the surface of SiO_2 can form local "charge puddles[6]" that induce local gating effects, contributing to the inability to turn graphene devices "off[7]." Beyond this, ambient air molecules, most notably O_2, can become physisorbed to the graphene surface resulting in a similar behavior. In this case, however, the gating effect almost always causes a *p*-type doping[8,9], which is the reason nearly all graphene transistors exhibit a Dirac point at a positive voltage under normal experimental conditions.

This observation has helped generate one tactic for controllably doping graphene sheets. The adsorbed molecules can be removed under mild annealing in a low pressure environment—after which the surface can be exposed to a sensibly chosen molecule (see Figure 4.1)[10,11]. Depending on the characteristics of the molecule, different degrees and types of local doping can be induced (Figure 4.1b-d). Furthermore, these molecules can be designed to be at least partially aromatic—increasing adherence to the conjugated surface of graphene. The advantage of this scheme is that it essentially converts the graphene layers into a uniformly doped sheet, yet remains largely reversible. This is because this method does not require any covalent bond and relies solely on the van der Waals interactions for stability. Such molecules are also typically unstable at moderate temperatures relative to graphene,

making it trivial to revert back to "undoped graphene."

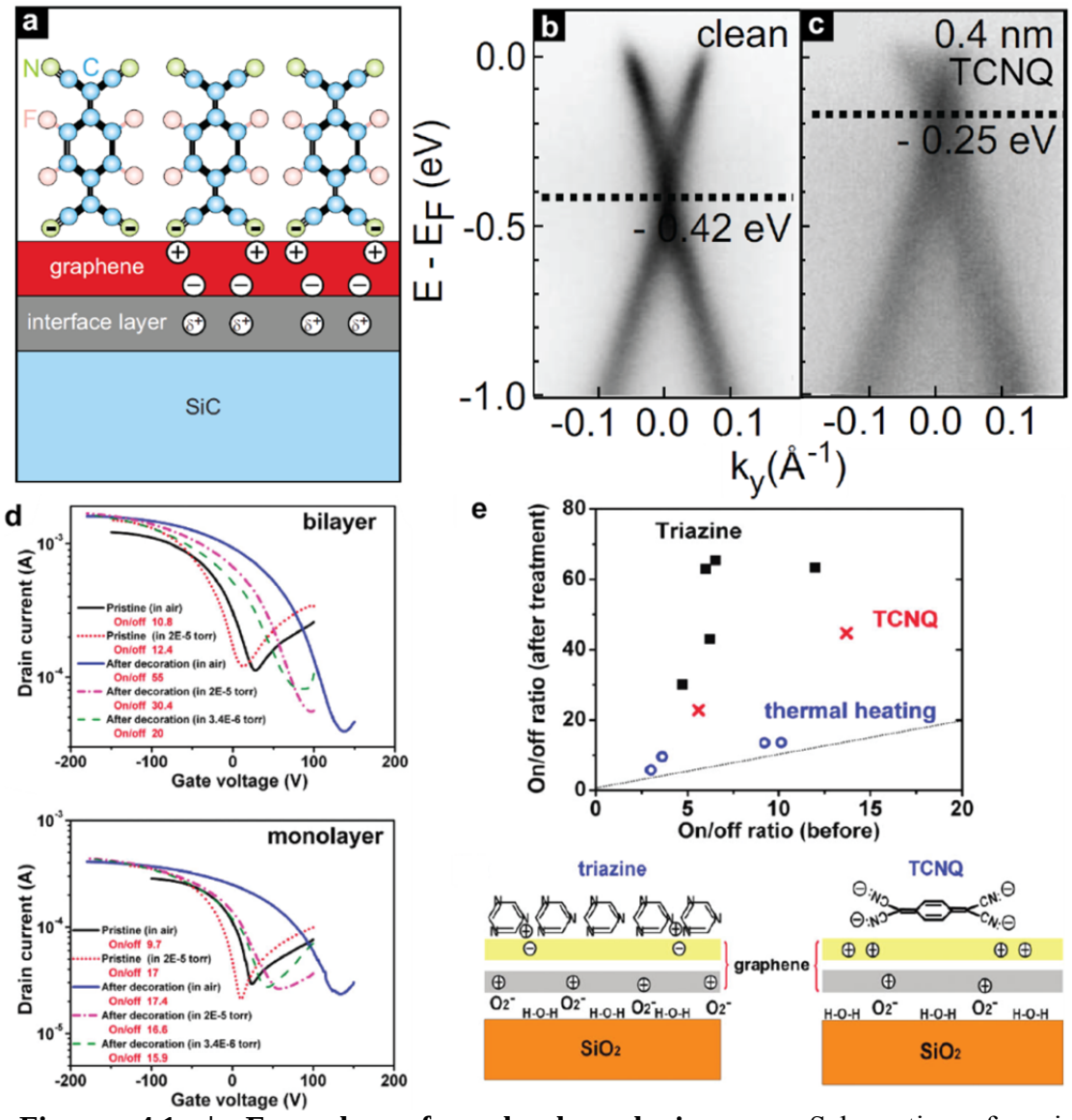

Figure 4.1 | Examples of molecular doping. **a**, Schematic of using tetracyanoquinodimethane (TCNQ), a common charge transfer salt, in order to dope graphene on SiC. **b**, ARPES measurements of a pristine graphene sheet (left), and **c**, doped with 4 nm of TCNQ (right) showing a significant shift in the energy of the system. **d**, Molecular doping of mono- and bi-layer graphene using triazine. Similar to TCNQ, this molecule induces a p-type shift in the behavior of the graphene. **e**, Upper: The presence of these molecules also results in higher on/off ratios, as opposed graphene flakes merely annealed at 150 ºC. Lower: schematic of molecular doping of exfoliated graphene layers. **a**, **b,** and **c** reproduced from Ref. 10, **d** and **e** reproduced from Ref. 11.

Unfortunately, the benefits of reversibility come at the expense of consistency in long-term performance. Moreover, by introducing additional molecules one is again losing the advantage of an atomically-thin film—adding a few angstroms in the best case scenarios[10], as seen in Figure 4.1a and c. For these reasons, other methods involving the direct chemical modification of the graphene surface have dominated recent research.

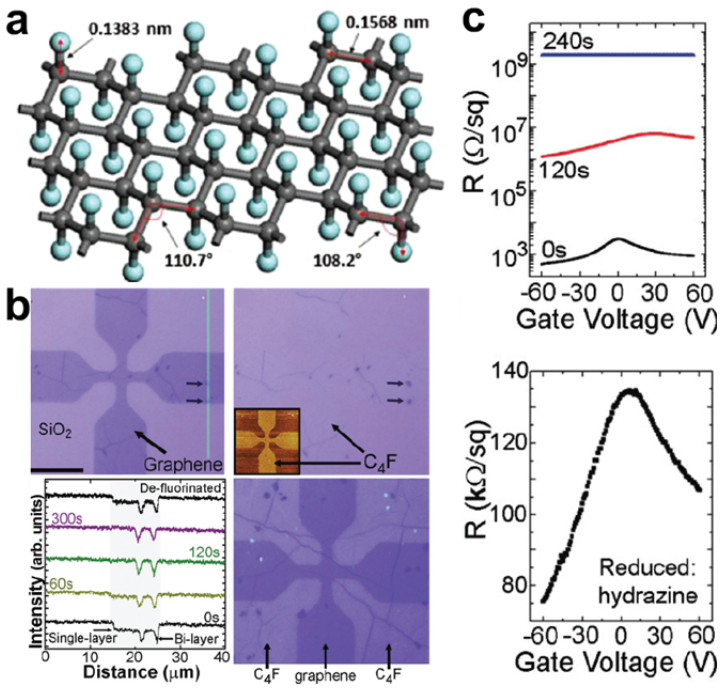

Figure 4.2 | Properties of fluorinated graphene. a, The structure of GrF is generic for halogenated graphene as well as graphane. F atoms bond to the exposed surface, converting C atoms from sp^2 to sp^3 hybridization. Due to the staggered nature of the atoms, however, complete saturation requires exposure to both sides of the sheet. Reproduced from Ref. 13. **b**, Optical images of patterned CVD graphene transferred onto a SiO_2 substrate before (top left) and after (top right) fluorination. The AFM height image (top right inset) proves the presence of the patterned film, despite the loss in optical contrast. Lower left: Green light intensity shows distinct absorption for unexposed graphene (bottom), which disappears upon fluorination. Lower right: This contrast is recoverable upon annealing in hydrazine, which converts the film back into graphene. **c**, Electrical measurements of GrF show insulating behavior at single-sided fluorination. This conductivity is partially recovered after reducing in hydrazine (lower). **b** and **c** reproduced from Ref. 12.

Fluorinated Graphene

First reported in 2010, fluorinated graphene (GrF) has become a popular material for electrically and thermally isolating graphene pathways[12,13]. The material is formed by simply exposing a graphene surface to XeF_2 for a significant period of time. This induces a reaction between the fluorine (F) ions and the carbon (C) lattice, leading to new covalent bonds. The F atoms arrange themselves in a similar fashion to the predicted "graphane[14]" (a hydrogen saturated graphene system, exhibiting all sp^3 bonds; see Figure 4.2a) meaning that both sides of the graphene sheet must be directly exposed in order to fully saturate the system with F (forming CF)—whereas single-sided exposure saturates at ~ 25% (resulting in C_4F). It follows that using a protective layer also allows spatial patterning of GrF/graphene sheets. Introducing these new atoms into the lattice causes a dramatic change in the properties of the graphene sheets. Instead of merely doping the material, the electronic structure is changed completely—leading to insulating properties[15]. As one might infer, this also changes the optical characteristics drastically, resulting in a film that is transparent in the visible regime (see Figure 4.2b). Interestingly, XeF_2 is also commonly used as a Si etchant in CMOS processing. This method, therefore, also enables simultaneous suspension of large areas of graphene and creation of GrF areas.

Surprisingly, the formation of GrF is also reversible, opening up the exciting potential for fabricating devices that can be effectively modulated between insulating and conducting states. As presented in Figure 4.2c, researchers have shown that recovered graphene yields electrical properties that are only moderately worse, and are consistent with the expected disorder resulting from defluorination, as supported by

Raman spectroscopy measurements[12].

Edge Doping Graphene: Ammonia

It is well known that the edge states in pristine graphene based devices are the most reactive sites, largely due to the deviation of the crystal structure at these positions[16]. Typically, this leads to a lack of control in the termination of these edges, which can deviate from the expected hydrogen (H) atoms. For macroscopic devices, the effects of these edge states can be largely ignored, but when scaled down to form graphene nanoribbons (GNRs), it becomes extremely important to precisely control these sites.

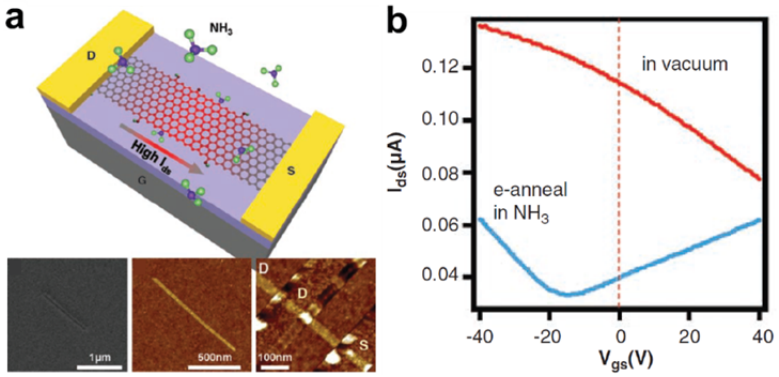

Figure 4.3 | Functionalizing nanoribbon edges with ammonia. a, Schematic of functionalization process, involving joule-heating in the presence of ammonia gas. This leads to a distribution of N-termination along the graphene nanoribbon edges. **b**, Gate dependence of devices show *p*-type doping originally, but exhibit *n*-type behavior after introducing N atoms (blue). Reproduced from Ref. 17.

To combat this, experimentalists have demonstrated an ability to induce site selective reactions with ammonia, yielding uniform chemical terminations with the added benefit of *n*-doping the devices[17]. This is performed via an electrothermal reaction (see Figure 4.3a), whereby GNRs are subjected to a high amount of current in

a NH_3 rich environment. This first cleans the GNRs via joule heating, and then helps catalyze a reaction between the ammonia and the edges of the GNRs, with most of the reaction occurring at the center of the device (where the temperature is the highest). This causes a significant shift from strongly *p*-type to moderately *n*-type behavior, as denoted in Figure 4.3b[17].

Although this method provides a great deal of control if the graphene sheets are defect free, it is not necessarily useful for CVD graphene sheets—where grain boundaries and pinholes can lead to an undetermined number of reaction sites[18,19]. Furthermore, it has recently been reported that the precise bonding structure of N dopants can lead to dramatic changes in the effects of these atoms, with some arrangements inducing *n*-type doping and while others are *p*-type[20].

4.3 | Reversible Doping with Molecular Chlorine (Cl_2)

The use of Cl_2 in doping graphene is intriguing due to its *p*-type nature. Despite the fact that Cl has additional valence electrons relative to C, its extreme electronegativity yields an efficient electron acceptor—inducing hole carriers into the graphene system. Although intrinsic graphene devices are *p*-type under ambient conditions, utilization of Cl atoms should provide a greater degree of tunability to this behavior. Additionally, given the reports of N introduction inducing *n*-type behavior, Cl_2 could potentially round out the capabilities necessary to make meaningful electrical devices out of graphene sheets.

In essence, Cl_2 exposure is extremely similar to functionalizing graphene with F and H—indeed if steps are taken to fully saturate the graphene surface with Cl

atoms, similar characteristics to GrF are observed[21]—namely a significantly reduced conductivity. Cl_2 is somewhat unique, however, in that it can react with the graphene structure under relatively low temperatures and with extremely slow kinetics. This allows researchers to incorporate only a small number of Cl atoms, which is much more consistent with traditional doping techniques.

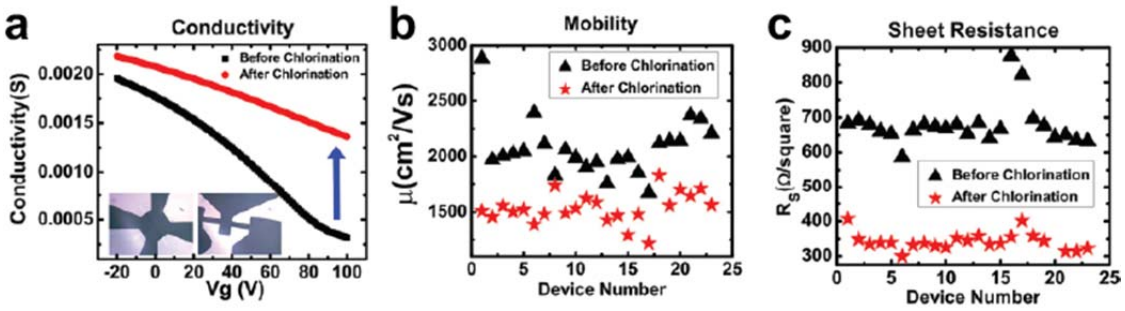

Figure 4.4 | Transport properties of chlorinated graphene. a, Gate dependence of pristine (black) and chlorinated (red) graphene devices show a significant positive shift of the Dirac point—indicating heavy *p*-doping. This results in a large increase in the observed conductivity at $V_G = 0$. **b**, Mobility values show a moderate decrease after chlorinatation, whereas **c**, sheet resistance shows a reduction of over 50%. Modified from Ref. 23.

Other groups have taken advantage of this by exposing GNRs and/or large sheets to a controlled Cl_2 plasma[22,23], finding that this process creates covalent bonds between Cl and C atoms preferentially at defect sites and edge states[24]. From the data shown in Figure 4.4, it is clear that Cl exposure led to a strong positive shift in the Dirac point, and thus a significant increase in the zero-gate conductivity is observed. Both of these effects should be expected under heavily *p*-doped GNRs and graphene transistors. Despite this increase in conductivity, researchers did note a moderate decline in carrier mobility, with values decreasing by ~25%. This is most likely due to the increased number of scattering sites—be it from the Cl atoms present or the

defects induced by the etching process[24].

These findings are very similar to our own results, as presented in Figure 4.5, although we have found that a plasma is not necessary for the introduction of Cl to the system. We observed uniformly low resistance values for a large number of devices following exposure to short Cl_2 pulses at a moderate temperature (~300 ºC) (see Figure 4.5a and 4.5c). Furthermore, we find that despite these drastic changes in electrical conductivity, no obvious change is observed in the Raman spectra of exposed devices (Figure 4.5b), despite confirmation of the presence of Cl atoms via XPS. Our devices were also recovered upon brief anneals in a H_2 environment, with resistance values reverting to their baseline numbers. While we were able to induce this recovery upon exposure to slightly higher temperatures (~350 ºC), we note that the devices were extremely stable under ambient conditions.

In spite of these advantages, reliance on defects as the primary reaction site is not an ideal situation. Not only does this place an initial upper bound on the atomic percent of dopant atoms, it will also result in extremely different results for CVD graphene sheets grown under different conditions. As the Cl_2 needs to react at vacancies, grain boundaries, or edges, highly polycrystalline growths will yield heavily doped devices, whereas large grains will exhibit correspondingly low doping values. Furthermore, the process must be critically timed, as overexposure can lead to a slow etching of the graphene film, further reducing electrical performance and reliability. While certain techniques, such as photochemical reactions, alleviate the need for defect sites, they too are largely uncontrollable and quickly convert graphene into an insulating sheet[21]. Therefore, in order to produce samples with maximal

reproducibility and control, most of the field has instead turned their focus towards the introduction of substitutional dopants during growth.

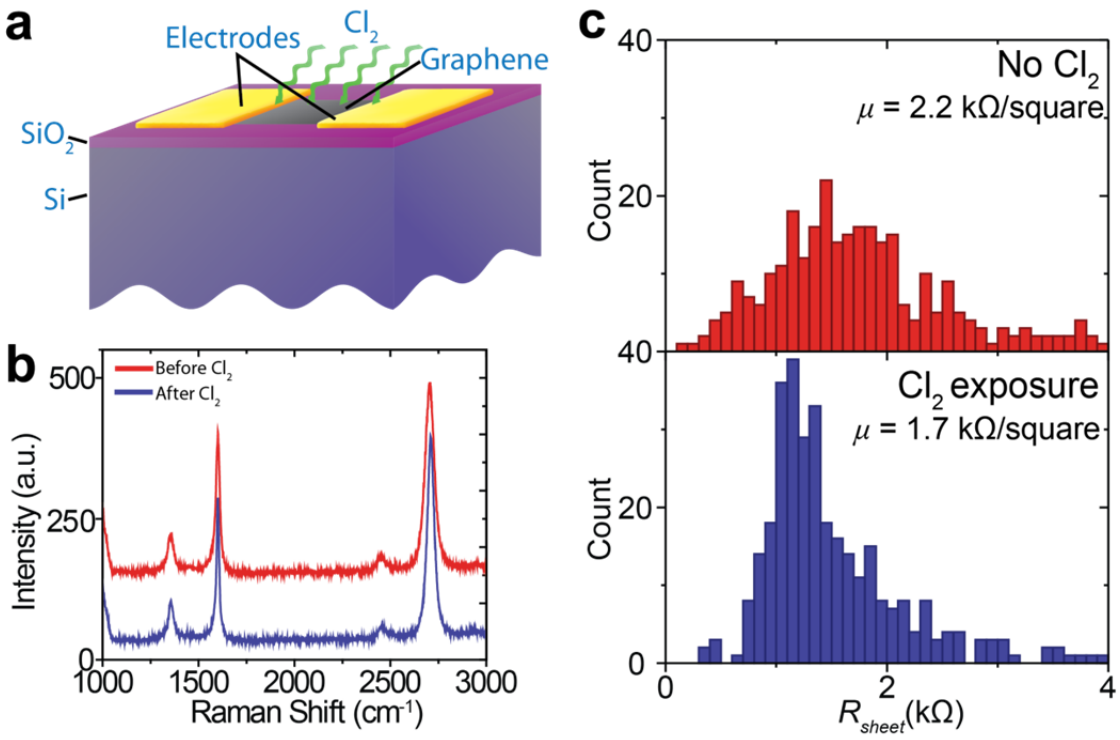

Figure 4.5 | Effects of Cl doping CVD graphene. a, Schematic of the doping process. Prefabricated graphene devices are placed in a reactor furnace and exposed to Cl_2 at moderate temperatures (<300 ºC) for a short time. **b**, Due to the dilute nature of the gas, as well as the short exposure time, virtually no change is seen in Raman spectroscopy before (red) and after (blue) chlorination. **c**, Histograms of device sheet resistance (R_{sheet}) at V_G = 0 V show a significant decrease following chlorination. Levendorf, *et al.* unpublished, 2010.

4.4 | Substitutional Dopants

Substitutional dopants are the ideal form of chemical modifications in atomically thin sheets. By definition, such "defects" should not alter the bonding structure of neighboring atoms, and should only change the local lattice constants by a small amount. This provides a perfect setting, as by not introducing other effects, such

as enlarged vacancy areas or line/flower defects, the global reactivity of the sheets should be largely maintained. This is critical for the stability of any devices that are to be made using this technique. Unfortunately, in order to create such a system, the dopant gases must be introduced during the growth stage, as subsequent exposures would rely on knocking out C atoms from the lattice—an inherently destructive process to 2-dimensional materials[25,26]. The first direct verification of successful synthesis was published in 2011, where N was used as the dopant atom[27]. We will first introduce the results of this paper, after which we will present our similar research on B-doped graphene layers.

Nitrogen Doping Graphene

Introducing substitutional dopants into the graphene lattice is conceptually simple, in that the dopant atoms should merely be present during synthesis. Researchers at Columbia University first showed this is possible with N atoms by flowing small amounts of ammonia gas (NH_3) during regular CVD growth on Cu. They found that if the partial pressures were within a narrow range of values, typically < 0.1 Torr in a 2 Torr environment, N atoms would insert into the lattice substitutionally—that is, maintaining the sp^2 bonding nature of the surrounding C atoms.

These foils were first confirmed to be doped under careful STM studies where point-like defects were seen peppered throughout the samples, as is clearly shown in Figure 4.6c. Importantly, near these defects there appeared to be a shift in the Dirac point energy to negative bias values, consistent with the expected *n*-type doping of N

atoms. Raman spectroscopy measurements were also consistent with the introduction of a significant amount of defects, leading to a large D peak and the emergence of the D' peak[28] (see Figure 4.6a). The experiments further showed that the doping profile of these sheets was highly uniform, with the spatial variation of the Dirac point being narrowly distributed about ~ -270 meV (Figure 4.7a). This synthesis also proved to be reproducible for a relatively large variance of NH_3 partial pressures—enabling a great degree of control over the number of N atoms present.

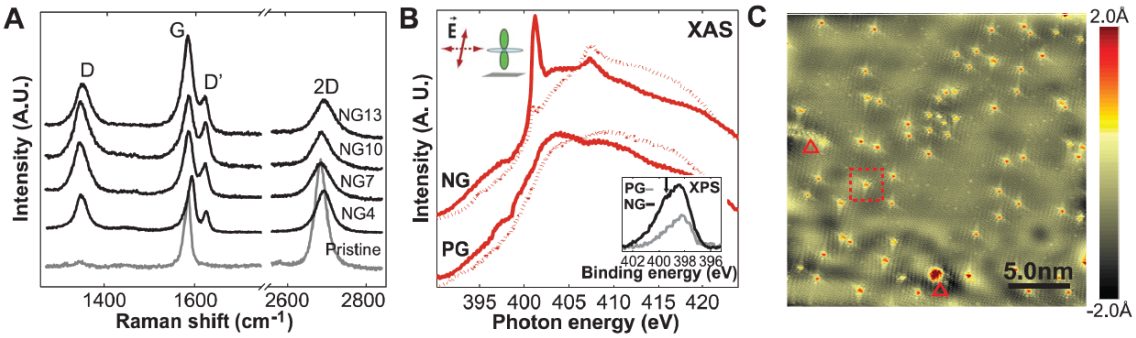

Figure 4.6 | Confirmation of substitutional N dopants. a, Raman spectra show significant increases in the D peak, as well as the emergence of the D' peak with increasing pressures of ammonia. **b**, X-ray absorption spectroscopy (XAS) measurements indicate the presence of N atoms. Further, a strong polarization dependence is observed, with an enhanced peak height for out of plane polarization—suggesting in-plane configuration of graphitic N. **c**, STM image of an N-doped graphene sheet over a large area showing a considerable number of point-like dopants (red spots). Reproduced from Ref. 27.

While these data are both evidence for the presence of *n*-type dopants, they are not necessarily indicative of N atoms being the root cause. This is because both Raman and scanning tunneling spectroscopies are not sensitive to atom type or bonding order. While defects cause changes in both types of spectra, these can arise from many different structures, including vacancies or other types of atoms. In order

to explicitly verify that these dopants are N, and beyond that are in an sp^2 configuration, near-edge x-ray absorption fine structure (NEXAFS) spectroscopy was performed. This experiment, shown above in Figure 4.6b, gives detailed information on the local structure of thin films. Here, it is clear that in pristine graphene (PG), no N signal is observed, whereas a large peak is seen in the N doped graphene (NG). Furthermore, the position of this peak as well as the strong polarization dependence suggests an in-plane C-N bonding structure with the N in an sp^2-bonded graphitic form[29].

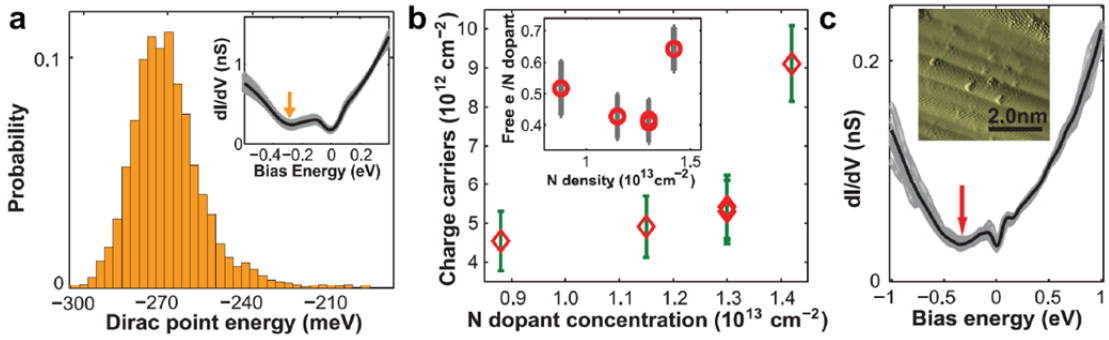

Figure 4.7 | STS measurements of NG films. a, Histogram of Dirac point energies showing the spatial variance (1600 nm^2 area). Inset: spatially averaged (black line) *dI*/*dV* spectra and variation (grey band). **b**, Spatially averaged charge carriers versus N dopant concentration suggests an average of ~ 0.5 free electrons per N atom (inset). **c**, STS and STM (inset) of a NG sheet transferred onto Si/SiO_2. Although some areas show behavior consistent with as grown NG sheets, the bonding formation is sensitive to the harshness of the transfer process and can result in unexpected doping behaviors (see Figure 4.9f below). Arrows indicate Dirac point energies. Modified from Ref. 27.

The importance of these findings is clear, given that this method provides a direct route for altering the electronic structure of graphene in a bottom up approach. It is also imperative, however, that the stability of these structures be confirmed. This is particularly important in the case of N-doped graphene, as the various bonding

possibilities of the N atom can have drastically different effects on its doping viability. Indeed, a follow up study on these N-doped graphene films found that, if the N atom is either pyridinic or nitrilic as opposed to graphitic, it causes strong *p*-type behavior in the sheets (see Figure 4.9f below). Furthermore, they found that the graphitic N can be nudged into these bonding forms through even moderately abrasive processes—including most standard transfer techniques. Although certain areas may escape undamaged, as evidenced by the data shown in Figure 4.7c, a significant percentage of the remaining area can be severely altered by the process[20]. Consequently, complete implementation of this synthetic technique must still be augmented with improvements of all other aspects of 2D material processing—a challenging but necessary endeavor.

Boron Doping

Similar to the N work, our group has investigated the introduction of B directly into the graphene lattice in collaboration with the Pasupathy group at Columbia University[30]. B dopants should theoretically provide a controllable degree of *p*-doping, as opposed to the *n*-type behavior of N. Like N, B can also substitutionally insert into the lattice[31], as the bonding structure of the atom is preferentially trigonal. As stated earlier in this chapter, these two elements should together provide a complete palette of graphene "flavors," enabling production of *p*- and *n*-doped layers, in addition to intrinsic (*i*-) graphene sheets. If combined with spatial control, it should then be possible to fabricate atomically-thin junctions, thus leading to bipolar transistors (*n*-*p*-*n* or *p*-*n*-*p*) and *p*-*i*-*n* diodes at the ultimate thickness limit. While recent works have

been published on the synthesis of B-doped graphene[32–35], none of these previous results enable production using standard gaseous feedstocks or conventional CVD processing, which we focus on here. Many alternative methods focus on using precursors with B atoms already present. While this leads to relatively consistent results, it severely limits the tunability of the growth—requiring new custom designed molecules in order to change the relative atomic percent of B.

The synthesis of B-doped graphene is very similar to the growth techniques already discussed. Instead of performing the reaction in an ammonia rich environment, however, the graphene growth is performed in a B-rich atmosphere. While conceptually identical to the N-doped synthesis, practical realization of this is surprisingly difficult. Most graphene growths are performed at 1000 °C on Cu foil, which is already very close to the melting point of Cu (~ 1083 °C). In conventional growths this is not normally an issue, and is actually beneficial to the growth of large grains of graphene, however in a B-rich environment different kinetics come into play. It turns out that at these temperatures B and Cu can form an alloy with a depressed melting point—known as a eutectic alloy—that saturates at roughly 13% B by atomic weight[36]. This in turn causes two direct problems with graphene growth. The first is that the Cu surface can be significantly disrupted, leading to a "poisoned catalyst" that either prevents graphene growth or yields significantly defected graphene sheets. The second is that the B also dissolves into the residual Cu that begins to line the reactor tube. This B can then evolve out during subsequent growths, leading to uncontrolled exposures in later syntheses.

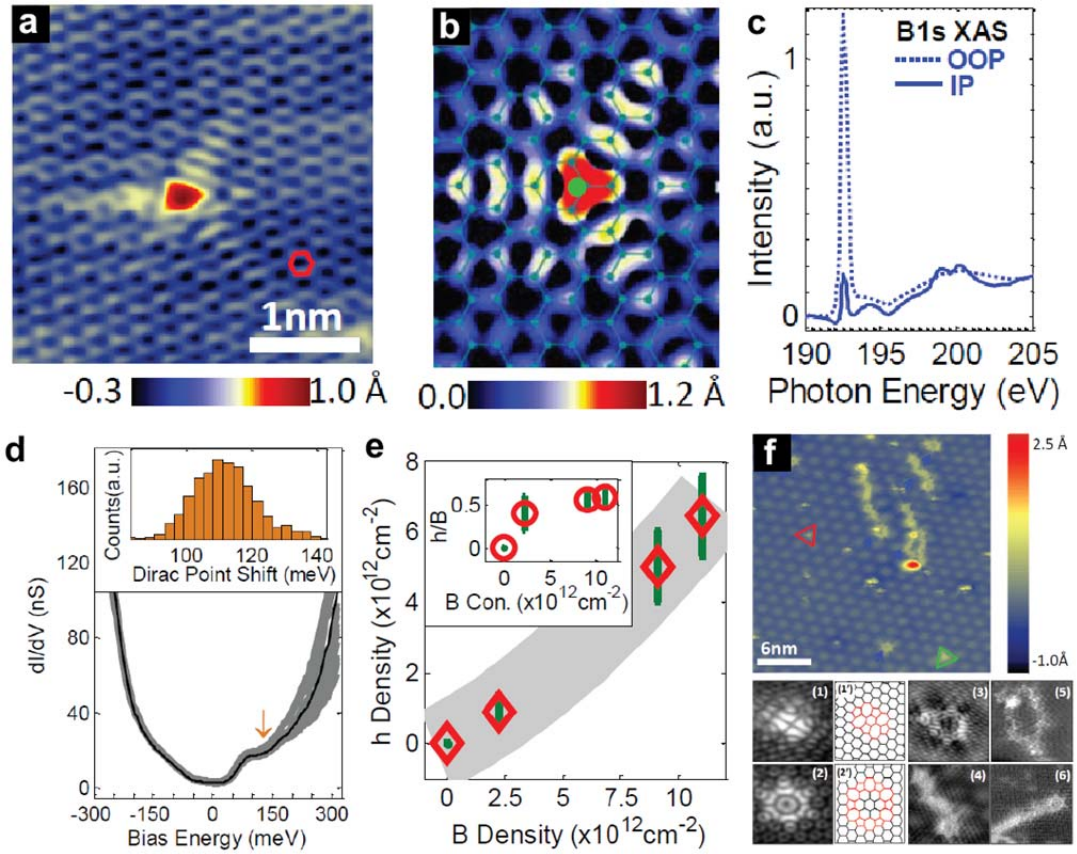

Figure 4.8 | STM and XAS of B doped graphene. a and **b**, STM images show point-like defects in the graphene lattice, very similar to the NG case discussed in the previous section. **c**, XAS measurements confirm the existence of graphitic B, again showing strong polarization dependence suggesting an in-plane conformation. **d**, Upper: Dirac point energies show another narrow distribution but with a *p*-type shift. Lower: STS scans again show a moderate spatial variation (grey band) from the average (black line). **e**, B also displays similar free carrier behavior, with slightly under 0.5 holes per B atom. **f**, Unlike the case of NG, BG has a large number of non-B defects. Line defects (4, 6) and ringed 5-7 defects are commonly observed (1-3, 5). Reproduced from Ref. 30.

These difficulties can be lessened by rigorous reproduction of the experimental procedures. To this end, we first start with a new quartz tube. Following a standard anneal procedure, we perform an initial "dummy" reaction with a piece of Cu foil in the center of the reactor. For this exposure we do not flow a C source, and instead only flow H_2 and diborane (B_2H_6) at the standard growth temperature. This causes the

sidewall deposition of Cu to be rich in B, which will then be exploited in the ensuing "real" growths. The dummy Cu foil is then discarded and a fresh piece is placed back into the tube and a normal graphene synthesis is performed—*i.e.* without flow of B_2H_6. By using fresh reactor tubes each time, an extremely dilute B_2H_6 feedstock (< 1000 ppm B_2H_6 in H_2), low flow rates, and consistently sized Cu foils we can then reproduce the environment of the ensuing growths.

In order to learn if and how B is inserting into the lattice, we worked in conjunction with the Columbia group to perform experiments similar to their N-doping report. After confirming a defected structure with Raman, STM was employed to investigate the existence of trigonal defects in the lattice, which can be seen in Figure 4.8. Under STS measurements, this defect structure was confirmed to cause *p*-doping in the material, with an energy shift of the Dirac from 0 meV to ~120 meV (Figure 4.8d). Unlike N, however, the introduction of B seemed to correlate with the presence of other defects in the lattice. These ranged from lengthy line defects to flower formations of 5-7 defects, as shown in Figure 4.8f. As yet, it is unclear as to whether the presence of B—either on the surface of the Cu catalyst or in the forming graphene lattice—directly contributes to the formation of these defects.

As with the previous study, the observation of such defects is not sufficient to identify B as the dopant. This is particularly important for such triangular defects that exhibit *p*-type doping, as many formations can lead to this effect. Again, NEXAFS was therefore performed on B-doped graphene (BG) as grown on Cu. As expected, it was determined that the BG exhibited an intense B peak that showed strong polarization dependence—consistent with in-plane bonding for the B (see Figure

4.8c). This bonding formation was not observed, however, for samples transferred onto SiO_2 substrates, again indicating that alternative transfer methods should be generated in order to maximize yield and maintain the desired characteristics.

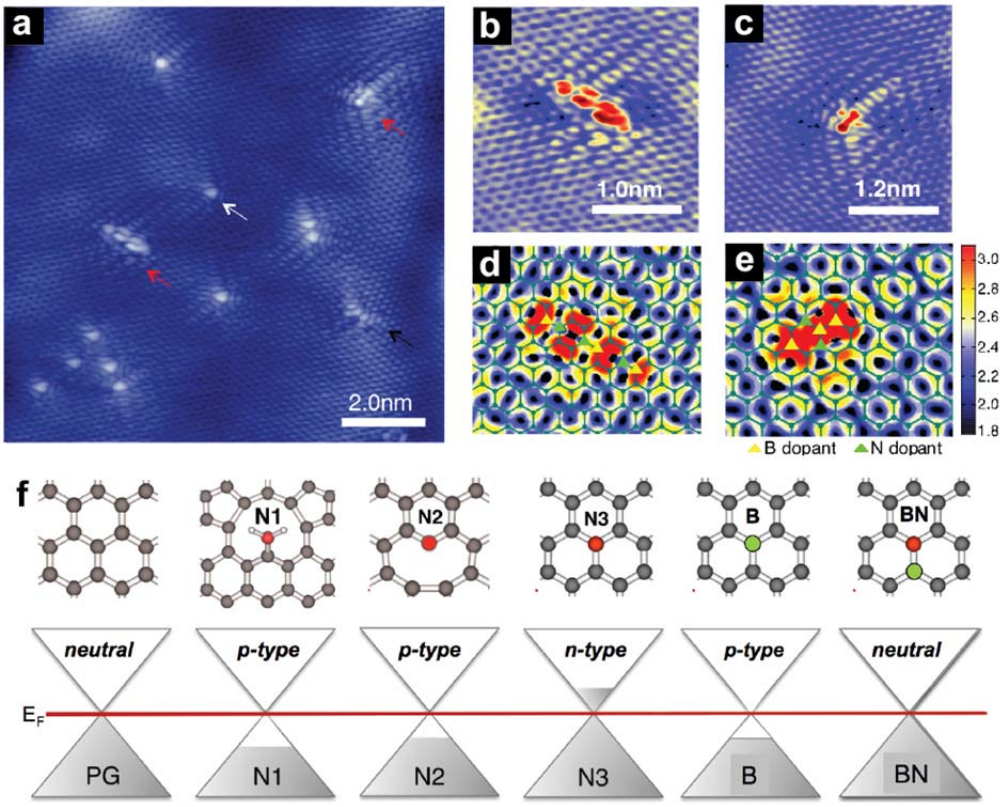

Figure 4.9 | B-N pairs in graphene sheets. a, Large-area STM image of a graphene sheet with B-N insertion pairs (red arrows), as well as lone B (white arrow) and N (black arrow) dopants. **b**, **d** and **c**, **e**, High resolution STM images of the B-N pairs shown in **a**, showing differing configurations. **f**, Doping type as a function of N bonding structure, and presence of B versus B-N pairs. These findings emphasize the need for precise growth and transfer techniques in order to create uniformly doped layers. Reproduced and modified from communications with T. Schiros (Columbia University) as well as Ref. 30.

While individual samples showcased decidedly uniform behavior, BG growths were found to have a much larger spread of results. This is primarily due to the difficulty of precisely reproducing reaction environments; however the presence of

ambient impurities also caused markedly different behavior. Interestingly, any residual N in the reaction system was found to result in B-N dimers inserting into the graphene lattice, which can be seen in the STM scans shown in Figures 4.9a-e. These pairs of atoms decrease the quality of the graphene films but, given their offsetting electronegativities and valence characteristics, result in no doping effects (see Figure 4.9f). It is therefore of utmost importance that the reactor environment be completely controlled and cleaned, preventing any outside impurities—including from the Cu catalyst—in order to produce BG reliably and efficiently.

4.5 | Summary

In this chapter we briefly introduced some methods of altering the electronic properties of single layer graphene through doping. Although further refinement of these processes is necessary—particularly in the uniformity of results across growths and transfers—these techniques still provide a broad set of tools to rationally modify the characteristics of graphene. With the exception of fluorination, however, the results of these studies have produced sheets with spatially homogeneous properties. As we discussed in Chapter 1, the ability to control single layers of graphene is not sufficient for the production of complex 2d electronics, which requires spatial control on top of compositional manipulation. In the following chapter we will utilize the techniques and expertise we have developed in Chapters 3 and 4 to solve this issue.

REFERENCES

1. Novoselov, K. S. *et al.* Electric field effect in atomically thin carbon films. *Science* **306,** 666–669 (2004).

2. Novoselov, K. S. *et al.* Two-dimensional gas of massless Dirac fermions in graphene. *Nature* **438,** 197–200 (2005).

3. Zhang, Y., Tan, J. W., Stormer, H. L. & Kim, P. Experimental observation of the quantum Hall effect and Berry's phase in graphene. *Nature* **438,** 201–204 (2005).

4. Williams, J. R., Dicarlo, L. & Marcus, C. M. Quantum Hall effect in a gate-controlled p-n junction of graphene. *Science* **317,** 638–641 (2007).

5. Meric, I. *et al.* Current saturation in zero-bandgap, top-gated graphene field-effect transistors. *Nature Nanotech.* **3,** 654–659 (2008).

6. Xue, J. *et al.* Scanning tunnelling microscopy and spectroscopy of ultra-flat graphene on hexagonal boron nitride. *Nature Mater.* **10,** 282–285 (2011).

7. Geim, a K. & Novoselov, K. S. The rise of graphene. *Nature Mater.* **6,** 183–191 (2007).

8. Ryu, S. *et al.* Atmospheric Oxygen Binding and Hole Doping in Deformed Graphene on a SiO_2 Substrate. *Nano Lett.* **10,** 4944–4951 (2010).

9. Wehling, T. O. *et al.* Molecular doping of graphene. *Nano Lett.* **8,** 173–177 (2008).

10. Coletti, C. *et al.* Charge neutrality and band-gap tuning of epitaxial graphene on SiC by molecular doping. *Phys. Rev. B.* **81,** 235401 (2010).

11. Zhang, W. *et al.* Opening an electrical band gap of bilayer graphene with molecular doping. *ACS Nano* **5,** 7517–7524 (2011).

12. Robinson, J. T. *et al.* Properties of fluorinated graphene films. *Nano Lett.* **10,** 3001–3005 (2010).

13. Huang, W., Pei, Q.-X., Liu, Z. & Zhang, Y.-W. Thermal conductivity of fluorinated graphene: A non-equilibrium molecular dynamics study. *Chem. Phys. Lett.* **552,** 97–101 (2012).

14. Elias, D. C. *et al.* Control of graphene's properties by reversible hydrogenation: evidence for graphane. *Science* **323,** 610–613 (2009).

15. Nair, R. R. *et al.* Fluorographene: a two-dimensional counterpart of Teflon. *Small* **6,** 2877–2784 (2010).

16. Jiang, D., Sumpter, B. G. & Dai, S. Unique chemical reactivity of a graphene nanoribbon's zigzag edge. *J. Chem. Phys.* **126,** 134701 (2007).

17. Wang, X. *et al.* N-doping of graphene through electrothermal reactions with ammonia. *Science* **324,** 768–771 (2009).

18. Huang, P. Y. *et al.* Grains and grain boundaries in single-layer graphene atomic patchwork quilts. *Nature* **469,** 389–392 (2011).

19. Kim, K. *et al.* Grain boundary mapping in polycrystalline graphene. *ACS Nano* **5,** 2142–2146 (2011).

20. Schiros, T. *et al.* Connecting dopant bond type with electronic structure in N-doped graphene. *Nano Lett.* **12,** 4025–4031 (2012).

21. Li, B. *et al.* Photochemical chlorination of graphene. *ACS Nano* **5,** 5957–5961 (2011).

22. Wu, J. *et al.* Controlled chlorine plasma reaction for noninvasive graphene doping. *J. Am. Chem. Soc.* **133,** 19668–19671 (2011).

23. Zhang, X. *et al.* Impact of chlorine functionalization on high-mobility chemical vapor deposition grown graphene. *ACS Nano* **7,** 7262–7270 (2013).

24. Khachatryan, L. & Dellinger, B. Formation of chlorinated hydrocarbons from the reaction of chlorine atoms and activated carbon. *Chemosphere* **52,** 709–716 (2003).

25. Cançado, L. G. *et al.* Quantifying defects in graphene via Raman spectroscopy at different excitation energies. *Nano Lett.* **11,** 3190–3196 (2011).

26. Wang, H. *et al.* Doping monolayer graphene with single atom substitutions. *Nano Lett.* **12,** 141–144 (2012).

27. Zhao, L. *et al.* Visualizing individual nitrogen dopants in monolayer graphene. *Science* **333,** 999–1003 (2011).

28. Malard, L. M., Pimenta, M. a., Dresselhaus, G. & Dresselhaus, M. S. Raman spectroscopy in graphene. *Phys. Rep.* **473,** 51–87 (2009).

29. Shimoyama, I., Wu, G., Sekiguchi, T. & Baba, Y. Evidence for the existence of nitrogen-substituted graphite structure by polarization dependence of near-edge x-ray-absorption fine structure. *Phys. Rev. B* **62,** R6053–R6056 (2000).

30. Zhao, L. *et al.* Local atomic and electronic structure of boron chemical doping in monolayer graphene. *Nano Lett.* **13,** 4659–4665 (2013).

31. Menetrier, M., Shirasaki, T., Derre, A., Tressaud, A. & Flandrois, S. Synthesis and characterization of boron-substituted carbons. *Thin Film.* **38,** 1461–1467 (2000).

32. Wu, Z.-S., Ren, W., Xu, L., Li, F. & Cheng, H.-M. Doped graphene sheets as anode materials with superhigh rate and large capacity for lithium ion batteries. *ACS Nano* **5,** 5463–5471 (2011).

33. Panchakarla, L. S. *et al.* Synthesis, Structure, and Properties of Boron- and Nitrogen-Doped Graphene. *Adv. Mater.* **21,** 4726–4730 (2009).

34. Wu, T. *et al.* Nitrogen and boron doped monolayer graphene by chemical vapor deposition using polystyrene, urea and boric acid. *New J. Chem.* **36,** 1385 (2012).

35. Wang, H. *et al.* Synthesis of boron-doped graphene monolayers using the sole solid feedstock by chemical vapor deposition. *Small* **9,** 1316–1320 (2013).

36. Chakrabarti, D. J. & Laughlin, D. E. The B−Cu (Boron−Copper) system. *Bull. Alloy Phase Diagrams* **3,** 45–48 (1982).

CHAPTER 5

SPATIAL CONTROL OF 2D MATERIALS: FORMING HYBRID SHEETS

5.1 | Overview

The overarching theme of this thesis has been skewed towards the eventual production of useful devices utilizing 2-dimensional films. Up to this point, we have focused on the challenges with merely generating usable materials but have not addressed the second major issue presented in Chapter 1: that exact spatial control over the properties of these materials is an ability that is critical to their successful implementation. Until recently, researchers have largely tackled this issue in heavy-handed ways—typically exploiting molecular dopants or destructive processes like ion bombardment. As introduced in section 4.2, fluorinated graphene allows for patterned films, but this process relies on the destruction of the conjugated nature of graphene—and thus is not a technique that can be used for a broad swath of 2D materials. Given the limitations of these methods, controlled fabrication of lateral heterostructures in these truly atomically thin systems has not been achieved.

In this chapter, which is largely adapted from Ref. 8, we will present our findings on integrating various atomically-thin materials into a single, continuous hybrid sheet. Graphene/*h*-BN interfaces are of particular interest to us, as it is known that areas of different atomic compositions may coexist within continuous atomically thin films[1,2] and that, with proper control, the bandgap and magnetic properties can be

precisely engineered[3–5]. However, previously reported approaches for controlling these interfaces have fundamental limitations and cannot be easily integrated with conventional lithography[6,7]. The method we have developed to address this issue, which we call "patterned regrowth," is a scalable process that allows for the spatially controlled synthesis of lateral junctions between electrically conductive graphene and insulating *h*-BN, as well as between intrinsic and substitutionally doped graphene[8]. We will demonstrate that our resulting films form mechanically continuous sheets across these heterojunctions. Our conductance measurements confirm laterally insulating behavior for *h*-BN regions, while the electrical behavior of both doped and undoped graphene sheets maintain excellent properties, with low sheet resistances and high carrier mobilities. Our results represent an important step towards developing atomically thin integrated circuitry and enabling the fabrication of electrically isolated active and passive elements embedded in continuous, one atom thick sheets, which could be manipulated and stacked to form complex devices at the ultimate thickness limit.

5.2 | Combining 2D Materials: Patterned Regrowth

Figure 5.1a summarizes our approach for the patterned regrowth and characterization. After growing the first film of graphene (G^1, superscript representing the growth order) we then deposit a protective layer of photoresist and pattern away unwanted areas. Next we grow a second layer of graphene or *h*-BN (G^2/*h*-BN^2) and transfer the hybrid film onto the desired substrate for further characterization. All of our growths are performed on 25 μm thick Cu foil using standard literature recipes for

both graphene and *h*-BN growths[1,9,10] and are performed in a He leak checked semiconductor grade tube furnace. Introducing dopant gases during any graphene growth stage allows us to produce both intrinsic graphene (*i*-G; H_2 + CH_4) and *n*-doped graphene (*n*-G; NH_3 + H_2 + CH_4) in a single process run. For intrinsic graphene (*i*-G) flow rates are typically H_2: 100 sccm, CH_4: 6 sccm, whereas for *n*-doped graphene (*n*-G) the flow rates are H_2: 100 sccm, CH_4: 2 sccm NH_3: 7 sccm. Prior to the first growth Cu substrates are annealed in H_2 at T = 1000 °C for 1 hour before introducing CH_4, as is done conventionally. Photolithography is then performed directly on the Cu substrate in order to pattern a protective layer of photoresist. An O_2 reactive ion etch is then used to remove the unwanted graphene from the surface, after which the patterned Cu is thoroughly cleaned of residual photoresist.

After drying, substrates are immediately placed back into the reaction chamber for the second graphene or *h*-BN growth. For the second growths samples were exposed to growth reactants upon reaching the growth temperature in order to maintain the integrity of the pattern. *h*-BN syntheses were carried out for 5 to 15 min by sublimation of the ammonia-borane, as in Ref. 10. For the "slow" growth *h*-BN (discussed later in this chapter; see Figure 5.3a), the effective flow rate from the precursor was ~1 sccm. For the "fast" growth, the flow rate was increased to ~4 sccm. We find that the use of an additional carrier gas leads to thicker films, limiting the usefulness for our method. Figure 5.1b shows optical images of the Cu growth substrate at different steps of the process. After patterning the first graphene layer, the substrate was heated to 135°C in air in order to enhance the contrast, as is shown in Figure 5.1b (left); the areas of Cu protected by *i*-G[1] remain unoxidized whereas the

unprotected areas do not[11]. Figure 5.1b (right) shows the same foil after reduction of CuO_x and subsequent synthesis of the second graphene, and demonstrates the homogeneity of the Cu/graphene substrate. Prior to further characterization, the presence of graphene is confirmed using micro Raman spectroscopy.

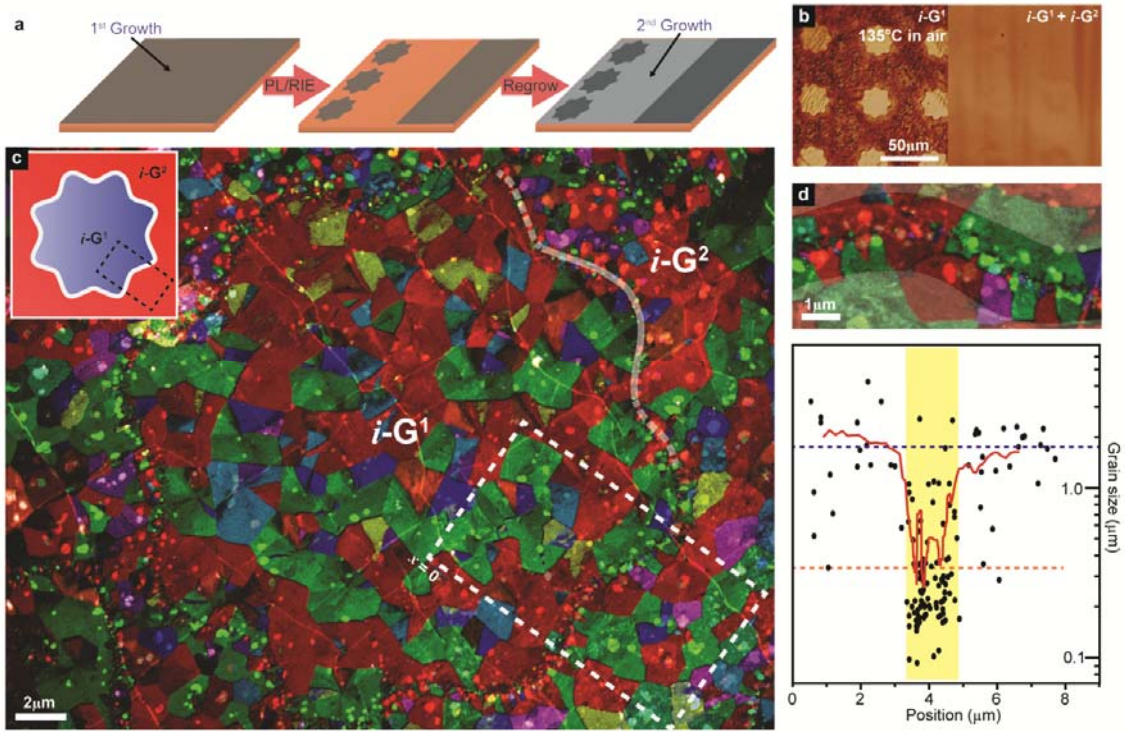

Figure 5.1 | Process schematic and DF-TEM characterization of graphene heterostructures. **a**, Schematic for formation of atomically thin lateral heterojunctions. See main text for details. **b**, Left: optical image of a patterned Cu/ G^1 foil oxidized in order to enhance contrast (Cu: dark areas). Right: optical image after reduction of CuO_x and subsequent growth of intrinsic-G^2 (*i*-G^2). **c**, False color DF-TEM image of an *i*-G^1/*i*-G^2 patterned area (schematic in inset). **d**, Zoomed-in image of the junction region. **e**, Plot of grain size vs position in the box outlined in c.

5.3 | Structural Properties of Hybrid Films

The fidelity of the transferred pattern and the quality of the junctions formed

by our method were studied using dark field transmission electron microscopy (DF-TEM), as discussed previously in Chapter 2[12,13], where use of a specific objective aperture filter allows imaging of areas with corresponding lattice orientations. Multiple such images can then be colored and overlaid to form a complete map of the film, resolving the grain structure and number of layers with nanometer scale resolution, near and away from the junction area. Figure 5.1c shows a composite image of a graphene sample that includes both the first and second grown areas as well as the junction between the two. For this, growths of *i*-G^1/*i*-G^2 were transferred onto 10 nm thick Si_3N_4 TEM membranes. Both G^1 and G^2 regions (see Figure 5.1c inset) are comprised of single crystals of similar sizes, which indicates that the polycrystalline structure of the graphene is mainly determined by the synthesis conditions rather than the growth order, and also that the structure of the first grown graphene is unaffected by our patterned regrowth. Significantly, the location of the junction closely follows the designed pattern within the resolution of our instrument (Figure 5.1c, partially outlined).

The grain boundary measurements presented in Section 3.4 have shown that a more reactive growth environment produces graphene-graphene grain boundaries with high quality lateral connections and minimal interdomain electrical resistance[14], while a less reactive one results in poorly-connected or even overlapped junctions. In our pattered regrowth process, we thus use highly reactive growth conditions. This knowledge, in combination with our DF-TEM data, suggests that the junction between G^1 and G^2 areas should be laterally connected. This is further confirmed by electrical measurements which will be presented later in this chapter (see Section 5.4). DF-TEM

images of the junction areas indeed show high quality, continuous growth of graphene between G^1 and G^2 areas (Figure 5.1d), indicating that the crystallinity is maintained uniformly across this region without amorphous carbon or voids, within the spatial resolution of DF-TEM (~10 nm).

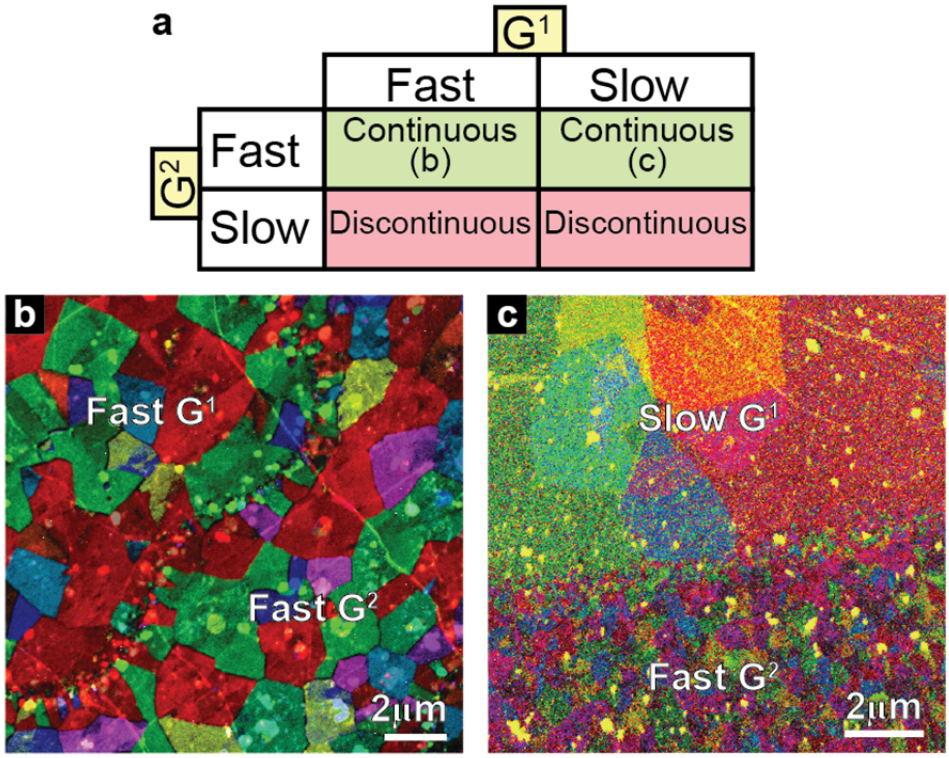

Figure 5.2 | Comparisons of fast and slow growth orders. a, Table showing successful (green) and unsuccessful (red) growth orders. The second growth must be performed in a highly reactive environment or films do not join. **b**, and **c**, DF-TEM images of two continuous graphene samples with different first growth reactivities.

In Figure 5.1e, we plot grain size as a function of position within the box indicated in 5.1c. While both G^1 and G^2 regions show average grain sizes of ~1.7 μm, near the junction they are much smaller (mean ~0.33 μm). The moving average (Figure 5.1e, red line) shows that the width of this area with smaller grains is

approximately 2 μm, comparable to the average G^1 and G^2 grain size. This, in addition to the increased density of small bilayer areas (bright spots, see Figure 5.1c and d), suggests that the junction between G^1 and G^2 is formed by graphene nucleated and grown in the junction area rather than by direct stitching between grains nucleated away from it. This suggests edge nucleated growth, which is similar to a "seeding" effect reported previously[15,16]. In contrast, regrowth under less-reactive conditions that provide slower growth do not produce well connected junctions in both graphene/graphene and graphene/*h*-BN films (see table in Figure 5.2a). In Figure 5.2 below we show DF-TEM images of zoomed in images of successful growth orders of fast/fast (Figure 5.2b, reproduced from Figure 5.1) and slow/fast (Figure 5.2c) growth orders—both resulting in continuous films.

The technique described above is also applicable to the formation of insulator-metal lateral junctions using graphene and *h*-BN (Figure 5.3), which we now discuss. Figure 5.3a shows a false color DF-TEM image of a single layer *h*-BN sheet—as confirmed by Raman spectroscopy and X-ray photoelectron spectroscopy—with relatively large domains in excess of 1 μm. Electron diffraction also shows that the film consists of single crystals with hexagonal lattice structures (Figure 5.3a, inset). This *h*-BN growth, however, yields films that are mechanically discontinuous, as indicated by the dark lines in Figure 5.3a (indicated by white arrows). Instead, *h*-BN grown under more reactive conditions (higher precursor flow rate) results in a continuous film, while exhibiting all the known characteristics of *h*-BN sheets. This is confirmed by the XPS data in Figure 5.3c (upper; B and N in a 1:1.08 atomic ratio) and Raman spectroscopy (lower; *h*-BN G peak).

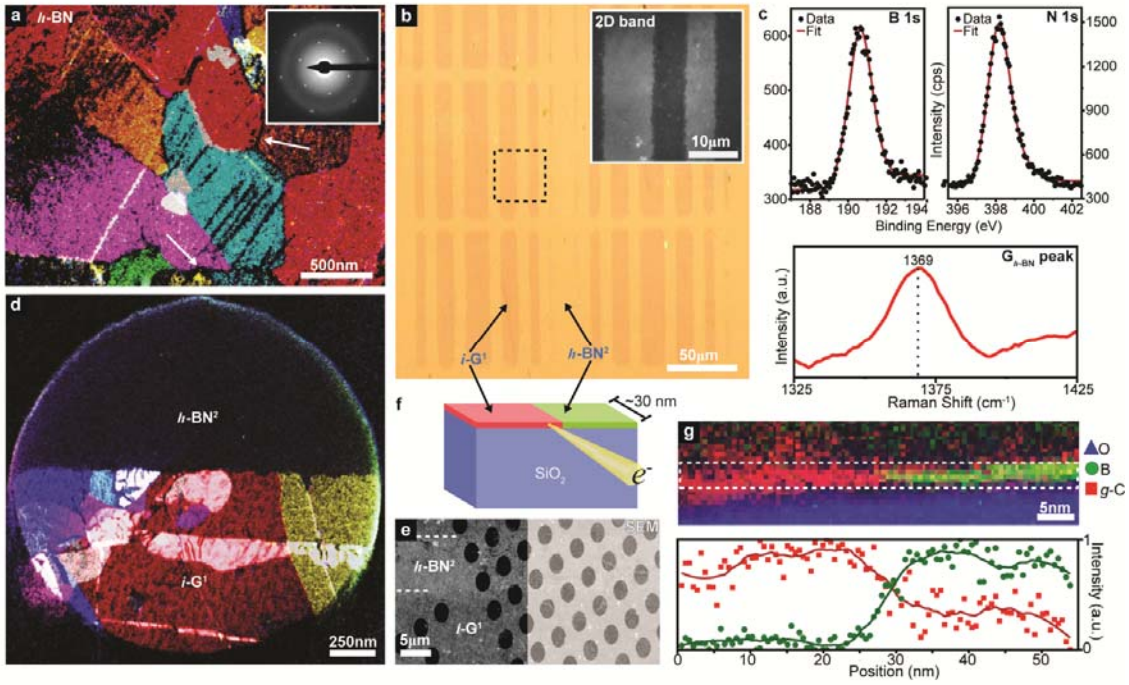

Figure 5.3 | *h*-BN/graphene heterostructure synthesis and structural characterization. a, False color DF-TEM image of a *h*-BN sheet grown in an environment of low reactivity with domains >1 μm. Arrows indicate regions where the *h*-BN film failed to connect. Inset: representative diffraction image taken from the *h*-BN sheet indicating hexagonal crystal structure. **b**, Optical image of an *i*-G^1 (darker areas)/*h*-BN^2 (lighter areas) on a Si/SiO_2 substrate. Inset: Raman graphene 2D band showing a stark contrast between the regions. **c**, XPS data (upper) for an *i*-G^1/*h*-BN^2 sheet (*h*-BN^2 grown in a more reactive environment relative to a), showing a 1:1.08 B:N atomic ratio. Raman spectroscopy (lower) confirms the presence of the *h*-BN G peak. **d**, False color DF-TEM image of a suspended *i*-G^1/*h*-BN^2 sheet with the junction region visible. **e**, SEM image of *i*-G^1/*h*-BN^2 film suspended over 2 μm sized holes. Higher contrast (left) highlights *i*-G^1/*h*-BN^2 regions, whereas lower contrast (right) shows the suspended film. **f**, Schematic for cross-sectional STEM EELS. **g**, Upper: elemental map of an *i*-G^1/*h*-BN^2 junction region showing graphitic carbon (red; *g*-C), boron (green), and oxygen (blue). Lower: Intensity profile of *g*-C and boron, indicating no voids or overlap in the junction region.

Careful control over the length of the *h*-BN^2 growth allows for the synthesis of *i*-G^1/*h*-BN^2 sheets with high pattern fidelity, as shown by the optical image in Figure 5.3b. The darker regions indicate areas of *i*-G^1 (stronger absorption) whereas the lighter regions are comprised of *h*-BN^2. This, as well as the 2-dimensional Raman

image (Figure 5.3b, inset) of the graphene 2D band intensity, confirms the successful pattern transfer to the *i*-G^1/*h*-BN^2 hybrid sheet. Furthermore, DF-TEM of suspended films confirms a sharp junction, as is shown in Figure 5.3d, where the grains of the *i*-G^1 growth (lower, colored) end abruptly at the interface with the *h*-BN^2 (upper). Both the brightfield TEM and scanning electron microscopy (SEM) images (Figure 5.3e) show a mechanically continuous sheet that is cleanly suspended with no breaks or tears at the junction region, confirming the stability and integrity of these growths. We have observed similar mechanical continuity for both *i*-G^1/*i*-G^2 and *n*-G^1/*i*-G^2 growths, which can be seen in Figure 5.4 below. While the *i*-G^1/*i*-G^2 growth is similar to data shown in previous figures, the *n*-G^1/*i*-G^2 growth shows a darkened region, as the *n*-G^1 growth had a much smaller grain structure than the *i*-G^2 growth.

The composition of G/*h*-BN heterojunctions at the nanometer scale was investigated by cross-sectional imaging and chemical mapping of the *i*-G^1/*h*-BN^2 interface using an aberration corrected scanning transmission electron microscope (STEM) and electron energy loss spectroscopy (EELS). For this, using a focused ion beam, a thin (~30 ± 5 nm) slice containing a junction region is carved out from a film of *i*-G^1/*h*-BN^2 transferred onto a Si/SiO_2 substrate (see Figure 5.3f). Figure 5.3g (upper) shows the resultant EELS composition maps across a junction region, where a line heterojunction is clearly seen between two neighboring regions with homogeneous atomic concentration. The left side indicates a high level of graphitic carbon (red; *g*-C), suggesting it belongs to graphene, whereas the other side has a high concentration of boron (green) originating from *h*-BN. Significantly, an increase in intensity of B corresponds to a decrease in *g*-C, as shown by the line profiles of the

concentration of B and *g*-C in the junction region (Figure 5.3g, lower), strongly suggesting that the G/*h*-BN junction is a lateral heterojunction with a compositional transition width of less than 10 nm.

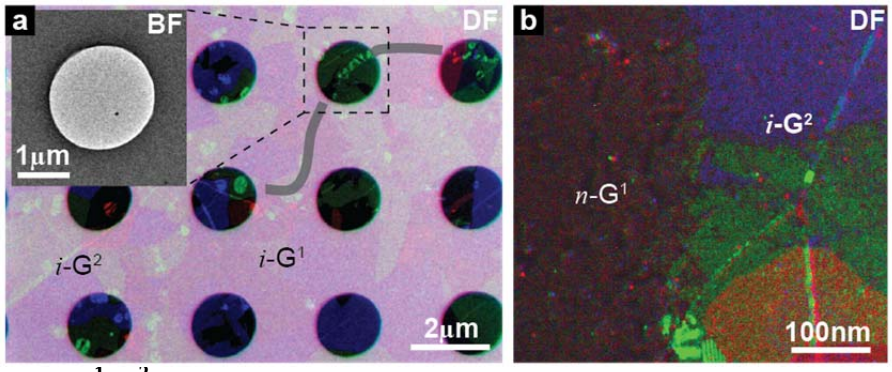

Figure 5.4 | G^1/G^2 suspended samples. a, DF-TEM image of suspended *i*-G^1/*i*-G^2 sample with pattern partially outlined. Brightfield image (inset) shows no tears in the film). **b**, DF-TEM image of suspended *n*-G^1/*i*-G^2 sample.

5.4 | Electrical Characteristics of Patterned Regrowth Devices

In order for electrically conductive heterojunctions to be useful, precise characterization and optimization of the junction resistance is essential. For this purpose, arrays of devices were fabricated that contained zero to four *i*-G^1/*i*-G^2 junctions. A false color SEM of an example cross-junction device is shown in Figure 5.5a. The sheet resistance at the Dirac point (R_{Dirac}) for each device was measured using top-gated four-terminal measurements (Figure 5.5b) and compiled for statistical comparison (Figure 5.5c). Devices with (orange; 15 devices) and without (grey; 19 devices) junctions show both narrow distributions of R_{Dirac}, as well as similar medians (no junction: 6.6 kΩ/□; cross-junction: 6.9 kΩ/□). This shows that the electrical properties of heterojunction devices are similar to that of devices without junctions,

despite the presence of many smaller grains in the junction area (Figure 5.1). Additionally, field-effect carrier mobilities near the Dirac point remain high (>10,000 $cm^2/V \cdot s$) for both types of devices, which is consistent with the properties of electrically-transparent, laterally-connected grain boundaries grown under reactive growth conditions[14].

Our method thus allows for the growth of doped heterostructures, such as *p*-*n* junctions, within a single sheet of graphene, which could enable the production of active components with mechanically and electrically continuous junctions. Figure 5.5e shows a false color optical image of a device with two differently doped graphene areas (n-G^1/i-G^2). The *n*-doped graphene area exhibits an additional D' peak (due to the presence of defects, in this case substitutional nitrogen dopants; Figure 5.5d, red curve) that is not typically seen in *i*-G growths (blue curve). The location of the junction region was thus confirmed using 2-dimensional Raman mapping of the ratio of the integrated D' and G peaks (Figure 5.5f), where the n-G^1 region is much brighter[1]. Electrical measurements within and across these regions again confirm electrical continuity across this region. Using top gates (Cr/Au 5/45 nm, 100 nm of evaporated SiO_2) we measured the gate dependence in different regions, as shown in Figure 5.5g (n-G^1/i-G^2). The device shows behavior consistent with high quality graphene, even across the junction region. The gate dependence of R_{sheet} in this area is in excellent agreement with an area weighted average of the n-G^1 and i-G^2 areas with the addition of the small resistance $\Delta R_{junction} \sim 0.15$ kΩ-μm (consistent with the small junction resistance seen in Figure 5.5c).

Multiple iterations of patterned regrowth would allow the formation of more

complex

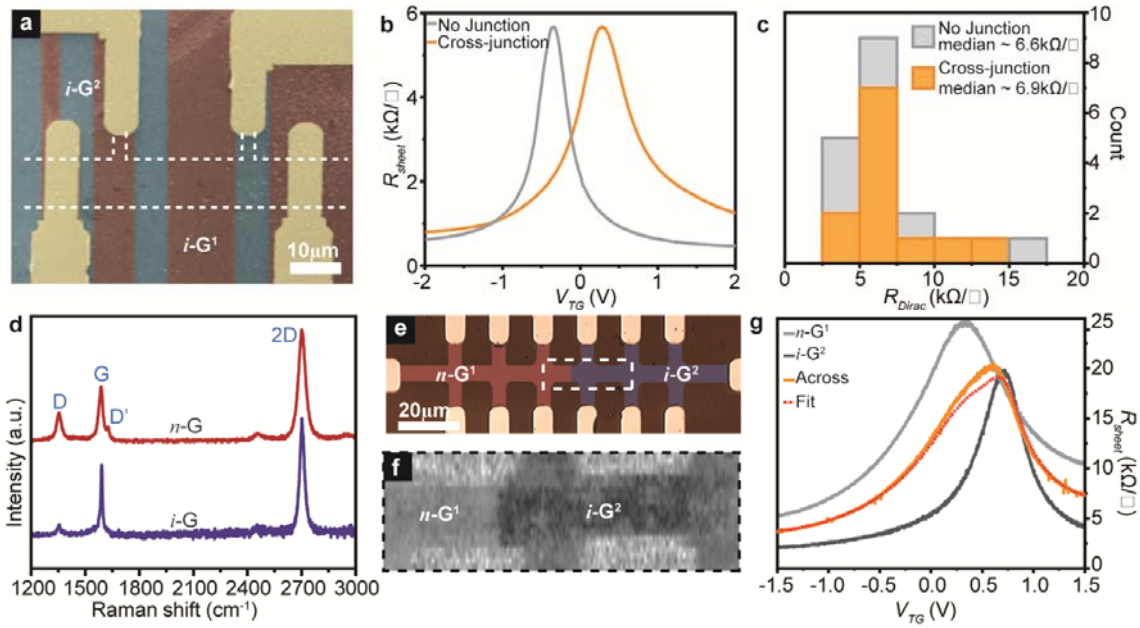

Figure 5.5 | Graphene junctions and heterostructures. a, SEM image with false color overlay of an *i*-G[1] (red)/*i*-G[2] (blue) cross-junction device before patterning. Final device area is indicated by the dashed lines. Cross-junction devices contained 1-4 junction regions. **b**, Four-terminal gate dependence for devices without (grey) and with (orange) *i*-G[1]/*i*-G[2] junctions, showing very similar peak resistances. **c**, Histograms of Dirac point sheet resistance (R_{Dirac}) for devices with and without junction regions. **d**, Raman spectroscopy of *n*-doped (*n*-G) and *i*-G growths (both synthesized in second step in order to allow direct comparison). **e,** Optical image with false color overlay of a heterojunction device. **f,** 2-dimensional Raman mapping of the ratio of the integrated D' and G peaks. **g,** Gate dependence of the junction region shows good agreement with an area weighted average of the homogenous regions (red line, $\Delta R_{junction} \sim 0.15$ kΩ-μm)

circuits connected by lateral heterojunctions, while multiple transfers of these films would produce vertical heterojunctions and interconnects for increased functionality. In order to realize more complicated structures, it is essential that the electrical properties of sheets grown at different steps are affected by the processing in a reproducible manner. In Figure 5.6, we show statistics for intrinsic (both *i*-G[1] and *i*-G[2]) and *n*-doped graphene device arrays (optical image shown in Figure 5.6a), which

exhibit high-performance electrical properties. Namely, they show high field-effect mobilities (again mean > 10,000 $cm^2/V{\cdot}s$; Figure 5.6b)[17] and low hysteresis. While we observe a slight difference between the *i*-G^1 and *i*-G^2 mobility distributions (Figure 5.6b), these values are consistent with variations seen from growth to growth (see *i*-G^2 in Figure 5.6c), suggesting that high electrical performances could be generally achieved even after multiple regrowth processes. In addition, the Dirac point shows a narrow distribution within each area for both intrinsic and *n*-doped graphene growths (see Figure 5.6b, c, insets). There is a shift of ~0.8 V between the Dirac point distribution of the *i*-G^1 and *i*-G^2 growths (Figure 5.6b, inset); however, the magnitude of this shift is reduced when the first growth is *n*-doped (~0.2 V, Figure 5.6c, inset). While this is consistent with the expected effects of *n*-doping, the overall device appears to remain *p*-type, likely due to the effects of the fabrication process. Thus, improvement in the transfer and fabrication steps should lead to increased control over not only the Dirac point distributions, but also general homogeneity[18,19].

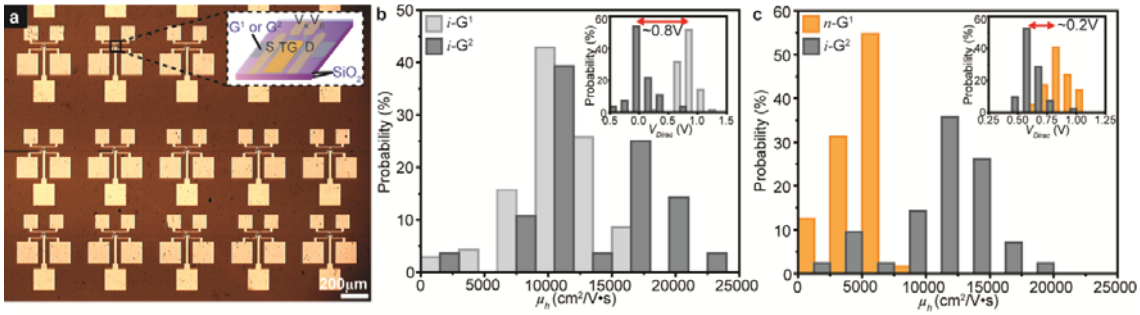

Figure 5.6 | Graphene device arrays and statistics. a, Optical image of an array of graphene transistors with device schematic (inset). **b**, Probability distribution of hole mobilities (μ_h) for *i*-G^1 (70 devices) and *i*-G^2 (28 devices) arrays. Inset: Probability distribution of the Dirac point for each array showing a difference (0.8 V) in the mean position. **c**, Probability distribution of μ_h for *n*-G^1 (orange; 65 devices) and *i*-G^2 (43 devices) regions. Inset: The Dirac point distributions are now much closer to the *i*-G^2 reference (0.2 V).

5.5 | Efforts Towards Stacked Electronics

Successful synthesis of hybrid films allows us to also fabricate electrically isolated graphene devices in a single, atomically flat sheet, which we show in Figure 5.7a. We observe conducting behavior confined to the patterned graphene areas, with the *h*-BN[2] showing no conductivity within the limits of our equipment (R_{sheet} > 400 TΩ/□). We also confirm that our *h*-BN is free of small conducting pockets of *h*-BNC that might form during the growth[2] using electrostatic force microscopy (EFM) (Figure 5.7c, right). The EFM phase shift is highly uniform within both the *i*-G[1] and *h*-BN[2] regions, however there is an abrupt change in the phase shift at the junction between *i*-G[1] and *h*-BN[2] due to the different electrical conductivities of these materials, indicating little C contamination bleeding into the *h*-BN[2] region.

These sheets are particularly useful for ultraflat 3-dimensional electronics[20], where alternating *h*-BN and graphene regions can act as a wire array connected by lateral insulators. Since such an array maintains a uniform thickness throughout, the device will remain flat even after multiple transfers of such sheets without any post processing, such as chemical mechanical polishing. We demonstrate this in Figures 5.7b and c, where we fabricated a large sheet of *i*-G[1]/*h*-BN[2] lines and performed multiple transfers onto a single substrate. After transferring the first sheet, a second was placed perpendicular to the first with each layer contacted by electrodes. Optical images (Figure 5.7b) show the structural uniformity of the final devices at different scales. The flatness and electrical properties of one such graphene-graphene crossed junction (Figure 5.7b, inset) is studied by atomic force microscopy (AFM) height (left) and EFM phase (right) measurements (Figure 5.7c). Topographically, region A (*h*-BN

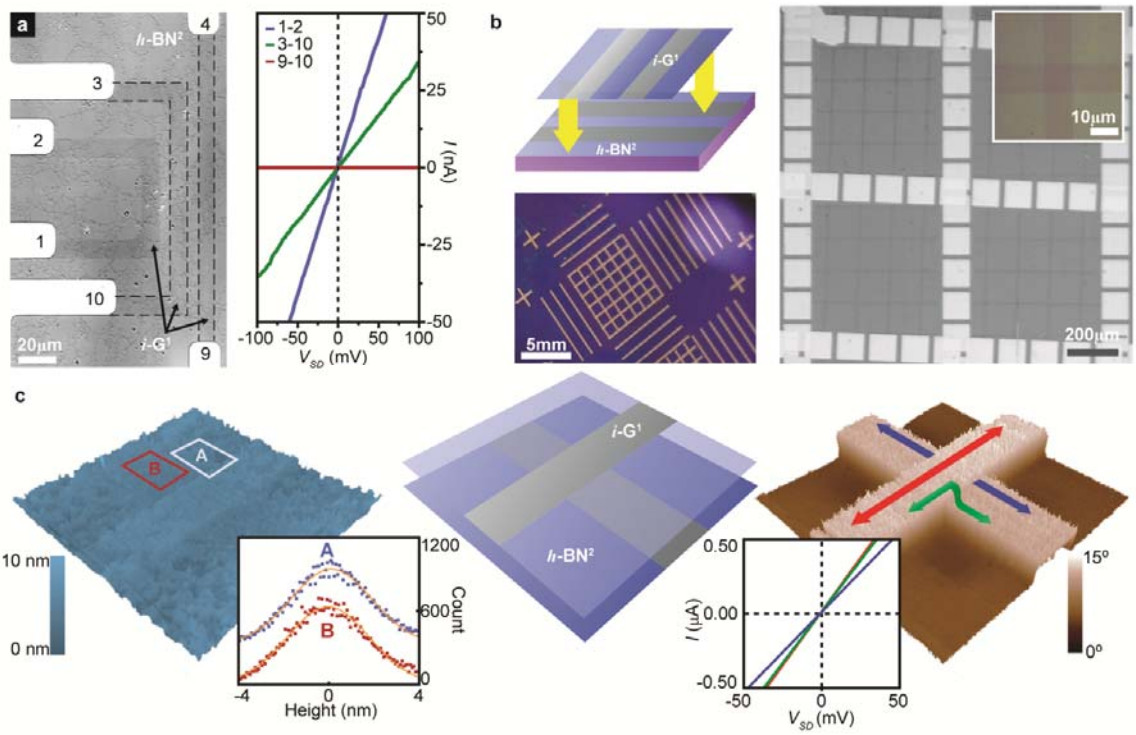

Figure 5.7 | *h*-BN/graphene electrical measurements. a, Left: optical image of an *i*-G^1/*h*-BN^2 sheet with electrodes contacting graphene strips. Right: Two-terminal *I-V* characteristics of indicated devices, with graphene showing conducting behavior and *h*-BN exhibiting insulating characteristics (R_{sheet} > 400 TΩ/□). **b**, Left, upper: schematic of a multiple transfer process for ultraflat 3-dimensional interconnects. Left, lower and right: optical images of increasing magnification of a final device substrate with each layer contacted by electrodes. **c,** Middle: schematic of a G^1-G^1 cross junction. Left: AFM height image of the cross. Region A (*h*-BN on *h*-BN) is virtually indistinguishable from region B (*h*-BN on graphene), as indicated by the histogram. Right: EFM phase image of the same junction. Both graphene strips are visible. Two-terminal *I-V* characteristics (lower; R_{sheet} < 3 kΩ/□) show no additional contact resistance due to the graphene-graphene contact.

on *h*-BN) is virtually indistinguishable from region B (*h*-BN on graphene), as shown by the height histograms from each region. This stands in stark contrast to the EFM phase image, where both the bottom and top graphene strips are detected with nearly identical phase shifts. The small difference between the EFM phases of the two areas nevertheless indicates that the *h*-BN on top of the bottom graphene strip is acting as a dielectric film. Electrical measurements (Figure 5.7c, right) of these connections show

a negligible addition of a contact resistance, confirming that such films behave as atomically flat 3-dimensional interconnects. Although the vertical tunneling current through one layer of *h*-BN is significant[21,22], few layer *h*-BN formed by additional transfers could be used to electrically isolate devices vertically as well, and allow fabrication of other passive elements, such as capacitors[23].

We propose that our patterned regrowth technique provides a versatile and scalable method for growing and integrating layered materials, beyond *h*-BN and graphene, for atomically thin circuitry. In particular, the addition of two-dimensional semiconducting materials, such as MoS_2[24], would bring together the three key building blocks (insulator, metal, and semiconductor) of modern integrated circuitry into a single, transferrable film. Furthermore, the devices made using this approach are likely to remain mechanically flexible and optically transparent, allowing transfer to arbitrary substrates for flexible, transparent electronics.

5.6 | Summary

In this chapter we presented our work on combining multiple 2D materials into an atomically-thin sheet. We confirmed that this patterned regrowth method results in mechanically continuous films, with little to no degradation of carrier mobilities and a negligible additional resistance at the junction area. Though this method is reproducible under the given parameters, we also found that the success of this process is highly dependent on the kinetics of the second growth—requiring a highly reactive environment. This process not only enables complex circuitry in a single layer, but also facilitates the production of complicated 3D electronics, where each level must be

carefully engineered. We highlighted this potential by merging graphene and *h*-BN and creating 3D interconnects with little loss of conductivity. Such structures could be used as vias in conventional stacked electronics. Finally, we believe that this general technique can be applied to other similar materials, most notably transition metal dichalcogenides (for example: MoS_2, WS_2, $MoSe_2$, and WSe_2) which will unite a semiconductor (TMDs), an insulator (*h*-BN), and a conductor (graphene) in the thinnest possible manner.

REFERENCES

1. Zhao, L. *et al.* Visualizing individual nitrogen dopants in monolayer graphene. *Science* **333,** 999–1003 (2011).

2. Ci, L. *et al.* Atomic layers of hybridized boron nitride and graphene domains. *Nature Mater.* **9,** 430–435 (2010).

3. Liu, Y., Bhowmick, S. & Yakobson, B. I. BN white graphene with "colorful" edges: the energies and morphology. *Nano Lett.* **11,** 3113–3116 (2011).

4. Pruneda, J. M. Origin of half-semimetallicity induced at interfaces of C-BN heterostructures. *Phys. Rev. B* **81,** 8–11 (2010).

5. Miyamoto, Y., Rubio, A., Cohen, M. & Louie, S. Chiral tubules of hexagonal BC2N. *Phys. Rev. B* **50,** 4976–4979 (1994).

6. Wehling, T. O. *et al.* Molecular doping of graphene. *Nano Lett.* **8,** 173–177 (2008).

7. Williams, J. R., Dicarlo, L. & Marcus, C. M. Quantum Hall effect in a gate-controlled p-n junction of graphene. *Science* **317,** 638–641 (2007).

8. Levendorf, M. P. *et al.* Graphene and boron nitride lateral heterostructures for atomically thin circuitry. *Nature* **488,** 627–632 (2012).

9. Li, X. *et al.* Large-area synthesis of high-quality and uniform graphene films on copper foils. *Science* **324,** 1312–1314 (2009).

10. Kim, K. K. *et al.* Synthesis of monolayer hexagonal boron nitride on Cu foil using chemical vapor deposition. *Nano Lett.* **12,** 161–166 (2012).

11. Chen, S. *et al.* Oxidation resistance of graphene-coated Cu and Cu/Ni alloy. *ACS Nano* **5,** 1321–1327 (2011).

12. Huang, P. Y. *et al.* Grains and grain boundaries in single-layer graphene atomic patchwork quilts. *Nature* **469,** 389–392 (2011).

13. Kim, K. *et al.* Grain boundary mapping in polycrystalline graphene. *ACS Nano* **5,** 2142–2146 (2011).

14. Tsen, A. W. *et al.* Tailoring Electrical Transport Across Grain Boundaries in Polycrystalline Graphene. *Science* **336,** 1143–1146 (2012).

15. Yu, Q. *et al.* Control and characterization of individual grains and grain boundaries in graphene grown by chemical vapour deposition. *Nature Mater.* **10,** 443–449 (2011).

16. Sun, Z. *et al.* Growth of graphene from solid carbon sources. *Nature* **468,** 549–552 (2010).

17. Meric, I. *et al.* Current saturation in zero-bandgap, top-gated graphene field-effect transistors. *Nature Nanotechnol.* **3,** 654–659 (2008).

18. Moser, J., Barreiro, A. & Bachtold, A. Current-induced cleaning of graphene. *Applied Physics Letters* **91,** 163513 (2007).

19. Liang, X. *et al.* Toward clean and crackless transfer of graphene. *ACS Nano* **5,** 9144–9153 (2011).

20. Dean, C. R. *et al.* Boron nitride substrates for high-quality graphene electronics. *Nature Nanotechnol.* **5,** 722–726 (2010).

21. Britnell, L. *et al.* Electron tunneling through ultrathin boron nitride crystalline barriers. *Nano Lett.* **12**, 1707-1710 (2012).

22. Lee, G.-H. *et al.* Electron tunneling through atomically flat and ultrathin hexagonal boron nitride. *Appl. Phys. Lett.* **99,** 243114 (2011).

23. Sanchez-Yamagishi, J. *et al.* Quantum Hall Effect, screening, and layer-polarized insulating states in twisted bilayer graphene. *Phys. Rev. Lett.* **108,** 076601 (2012).

24. Radisavljevic, B., Radenovic, A., Brivio, J., Giacometti, V. & Kis, A. Single-layer MoS_2 transistors. *Nature Nanotech.* **6,** 147–150 (2011).

CHAPTER 6

NOVEL APPLICATIONS OF GRAPHENE MEMBRANES

6.1 | Introduction

Up to now the focus of our work has been solely on controlling the electronic structure of our synthesized graphene sheets. We have discussed how to form these films, and different ways of integrating these resultant sheets with existing technologies, as well as demonstrating novel uses of hybrid systems. Although these findings highlight the potential for this material in the realm of devices, graphene has many other excellent properties as well. These range from its surprising physical strength[1]—enabling the production of electromechanical resonators[2]—to its impermeability[3]. In exploiting these other characteristics, scientists have proposed unique applications of graphene including transparent conductive windows[4], thermal conductors, and even alcohol distillation[5]. Such varied and exotic uses have not only helped generate public interest in this material, but have also highlighted the great deal of promise that graphene has outside of electronics.

Here we will introduce our work focused on some underappreciated properties of graphene. We will devote the bulk of this chapter to our experiments using graphene as an atomically-thin protective coating[6]. Despite the thinness of this material, graphene nevertheless acts as an ideal barrier, limiting the tunneling and diffusion of atoms and molecules across them, which can be advantageous towards the shielding metal surfaces from corrosive or oxidizing agents. This property can therefore be used to either protect entire sheets of metal, or to selectively expose areas

to these harsh environments. Towards the end of this chapter, we will briefly introduce the use of graphene as a platform for chemical synthesis using work done by our collaborators in the Dichtel group at Cornell University. Given the aromatic nature of the compound, graphene provides a well-controlled surface for reactions to take place on. This characteristic yields the added benefits of low reactivity and even templating effects, as we will demonstrate in this section. Both of these studies are indicative of the impact graphene can have on niche markets/fields as well, and help combat the notion that graphene is merely an interesting material for electronics. Much of Section 6.2 is reproduced from an earlier version of Ref. 6 which was completed in collaboration with the Ruoff group at the University of Texas at Austin.

6.2 | Impermeability of Graphene Films

It is well documented that, despite being only one atom thick, graphene acts as an impermeable membrane[3]. This was first reported in 2008, where it was found that gaseous molecules could be contained in SiO_2 chambers sealed by a thin film of graphene (see Figure 6.1). Decreasing the external pressure subsequently led to a pooching out of the sheet, yielding a "graphene balloon." This seal was so good, that it was found that the deflation of this balloon was actually due to the diffusing of the gas molecules through the SiO_2, instead of tunneling through graphene. Due to this exciting discovery, graphene membranes were proposed for use as a vapor-liquid barrier, such as sealing aqueous solutions in a vacuum environment and facilitating various electron microscopies[7,8]. In essence, these studies utilized graphene in order to keep liquids inside a chamber, however this property can be just as useful to keep

molecules out of a system—which is the approach we will take in this section. We will first demonstrate the general use of graphene as a protective metal coating. This capability can then be exploited to pattern metal films using otherwise global etchants.

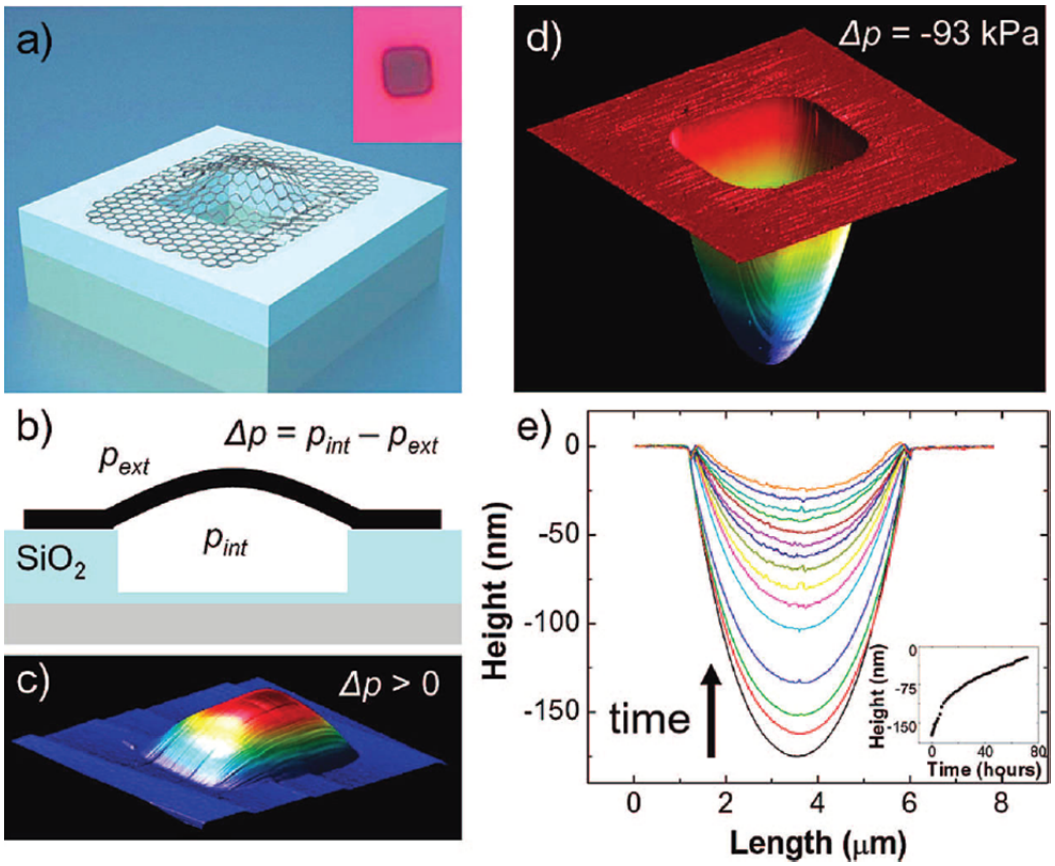

Figure 6.1 | Impermeability of graphene membranes a, Schematic of a chamber sealed by a film of graphene. Inset: optical image of a 4.75 μm x 4.75 μm x 380 nm chamber with a single layer of graphene covering it. **b**, Schematic of the chamber from a sideview. A positive pressure differential (Δp) causes the graphene to pooch out. **c**, AFM image of a microchamber with positive Δp. **d**, AFM image of a chamber with negative Δp. **e**, AFM height traces of the graphene membrane shown in the inset of **a**. Over time the deflection decreases (shown in inset). Reproduced from Ref. 3.

6.3 | Preventing Oxidation

The use of refined metals is widespread, but they are often chemically reactive, requiring protective coatings for many applications. Protecting the surface of reactive

metals has developed into a significant industry which employs many different approaches, including coating with organic layers, paints or varnishes, polymers, formation of oxide layers, anodization, chemical modification, and coating with other metals or alloys. However, these conventional approaches can suffer from a variety of limitations, such as susceptibility to damage by heat, limited chemical stability, cost, and formation of waste products. In addition, most conventional methods modify the physical properties of metals being protected. The addition of a protective coating changes the dimensions of the metal due to the finite thickness of the coating, changes the appearance and the optical properties of the metal surface, and often decreases the electrical and thermal conductivity. One important approach to overcome these problems would be to develop a novel protection coating with an exceptional chemical and thermal stability with minimum changes to the physical properties of the protected metal.

In this section, we show that graphene, both single layer and multi-layer, acts as an atomically-thin coating for various metal substrates with many of the desired properties of an ideal protection coating. The full potential of graphene as a protection layer can be easily understood based on its known physical and chemical properties. First, surfaces of sp^2 carbon allotropes form a natural diffusion barrier thus providing a physical separation between the protected metal and reactants. This can be seen from the encapsulation of various atomic species inside of fullerenes and carbon nanotubes at high temperatures and in vacuum[9]. Second, graphene has exceptional thermal and chemical stability. Under an inert environment it is stable at high temperatures (higher than 1500 ºC[10]) and it is also stable under many conditions where other substrates

would undergo rapid chemical reactions. In fact, the latter property has been the key to the processes used to separate large scale graphene from the substrates where they are grown. Combined, these two properties (impermeability and thermal/chemical stability) make graphene an excellent candidate for a novel protection layer. Furthermore, the presence of graphene adds only ~0.34 nm per layer to the total dimension of the coated metal.

In our experiments as described here, we demonstrate the ability of graphene to protect a variety of catalytic metal substrates under different reactive environments. We used CVD graphene grown directly on bulk Cu, Cu foils, Cu/Ni alloys, and evaporated Cu thin films. Samples were subjected to several reactive environments, including high temperature oxidation and corrosive aqueous environments. In all these cases we find that graphene serves as a good protection layer. First, we show outstanding oxidation resistance at metal surfaces under high temperature air anneals. We confirm this via optical microscopy, scanning electron microscopy, as well as X-ray photoelectron spectroscopy. Second, the chemical resistance of graphene itself in these environments is studied using micro-Raman spectroscopy, which suggests no changes to the majority of the graphene layer. In addition, we study the impact of imperfections in CVD deposited graphene on the degree of protection it provides. Using two-dimensional Raman spectroscopy we show that the metal surface is less protected when the graphene has a higher density of defects. Finally, we investigate other limiting factors that can weaken substrate passivation, such as weak adhesion of the graphene on the metal surface and accelerated corrosion at metal grain boundaries.

Large-area graphene samples were grown on metal substrates using previously discussed CVD techniques. Following growth, samples were cooled to room temperature and removed for testing. Prior to any studies, micro-Raman spectroscopy was performed on each sample in order to verify the presence of high quality graphene films. After growth, metal films are protected by only the graphene layer, as any metal oxides would prevent synthesis from occurring[11,12]. This property allows for direct comparison with the un-oxidized, bare metal surfaces.

In Figure 6.2 we show optical images of various metal surfaces, both graphene-coated and uncoated, after air anneals and exposure to liquid etchant. In all cases the graphene-coated metal surfaces show very little visible change, as opposed to the uncoated metals whose surfaces change appearance dramatically. More specifically, graphene-coated Cu and Cu/Ni foils show no changes after lengthy air anneals (200 ºC, 4 hours, see Figure 6.2c), whereas uncoated films exhibited a substantial darkening. In Figure 6.2d we show that even evaporated thin films of Cu can be protected by a single layer graphene coating. These samples were exposed to a more reactive environment of 30% H_2O_2, and showed minimal changes only near Cu grain boundaries. To further demonstrate the potential of graphene to function as a protection layer for bulk metal, we grew single layer graphene on a copper penny (95%Cu/5% Zn, minted 1962 - 1982). In Figure 6.2b two pennies are displayed, both of which were exposed to 30% H_2O_2 for 2 minutes. Although both pennies originally looked the same, a stark contrast arises between the graphene-coated (upper) and uncoated (lower) coins after exposure. The unprotected copper penny turned a dark shade of brown, whereas the protected coin maintained the original appearance. All

these examples show that graphene passivates the surface where it is grown which, as discussed earlier, is due to its impermeability and chemical resistance. Below we discuss these two aspects in more detail.

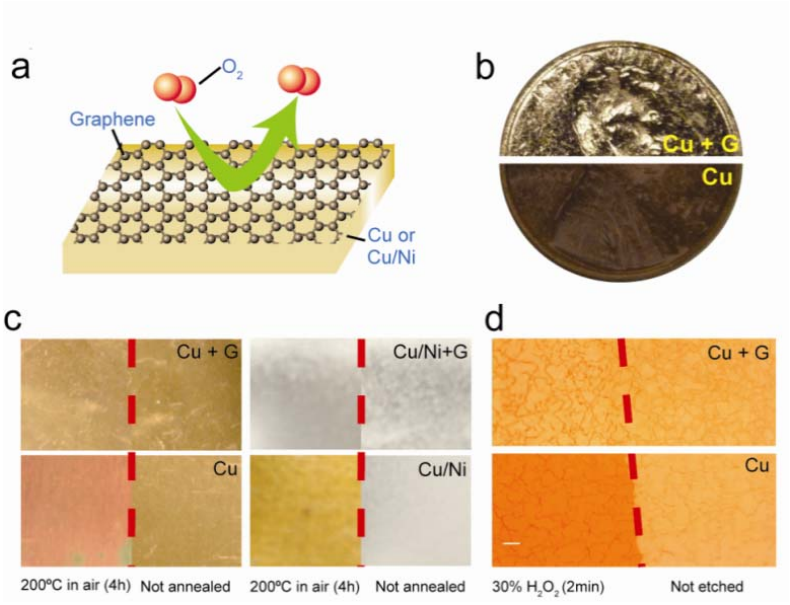

Figure 6.2 | Oxidation and corrosion resistance of graphene coated metal. a, Illustration depicting a graphene sheet as a chemically inert diffusion barrier. **b**, Photograph showing graphene coated (upper) and uncoated (lower) penny after H_2O_2 treatment (30%, 2 min). **c**, Photographs of Cu and Cu/Ni foil with and without graphene coating taken before and after annealing in air (200 °C, 4 h). **d**, Brightfield images of evaporated Cu film (500 nm thick) with and without graphene demonstrate the protection of the Cu under H_2O_2 exposure (30%, 2 min).

The graphene film can be seen as a molecular diffusion barrier, preventing the reactive agent from ever reaching the metal underneath (see schematic in Figure 6.2a). We show this in Figure 6.3 by SEM and XPS measurements of metal surfaces after air oxidation. Figure 6.3 shows a significant difference between protected and unprotected films. For both the graphene-coated Cu (Figure 6.3a) and Cu/Ni (Figure 6.3c) foils, nearly identical images are obtained before and after anneals. It is clear that

the surface morphologies are unchanged with many distinct steps and smooth surfaces, except for some minor decoration at the metal grain boundaries. This is in sharp contrast to images of unprotected metal films, which show a rough surface structure and are blurry—likely due to a charging effect from the presence of oxides.

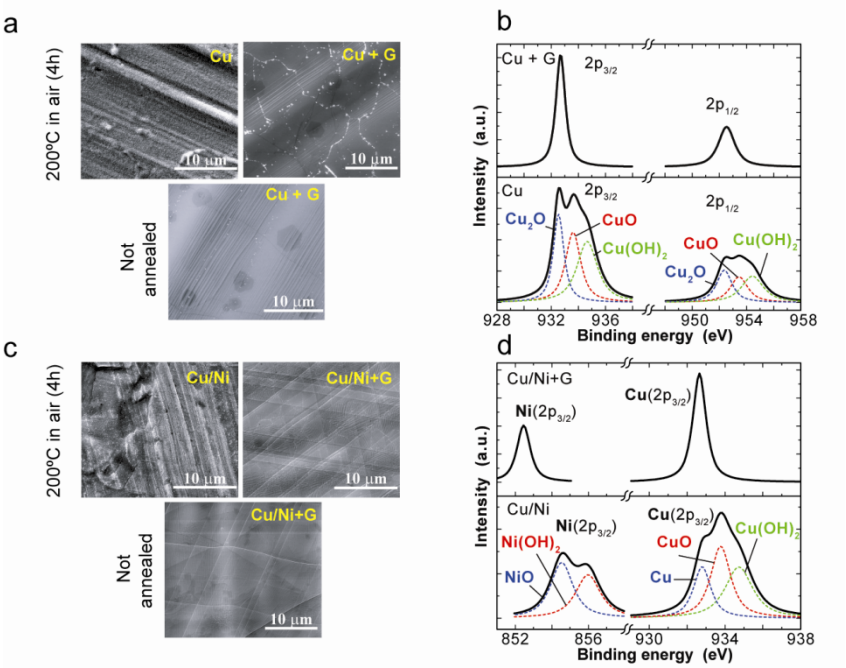

Figure 6.3 | SEM and XPS study of air annealed graphene coated films. a, SEM images of graphene uncoated and coated Cu foil taken after annealing in air (upper) compared to the coated Cu foil prior to anneal (lower). **b**, XPS core-level Cu2p spectrum of coated (upper) and uncoated (lower) Cu foil after air anneal. **c**, SEM images of Graphene uncoated and coated Cu/Ni foil taken after annealing in air (upper) compared to the coated Cu/Ni foil prior to anneal (lower). **d**, XPS core-level $Ni2p_{3/2}$ and $Cu2p_{3/2}$ spectrum of coated (upper) and uncoated (lower) Cu/Ni foil after air anneal.

XPS was then performed on these substrates in order to provide an analysis of the metal composition after heat treatment. The XPS spectrum of coated Cu foil shows two Cu peaks at binding energies of 932.6 and 952.5 eV, which correspond to $Cu2p_{3/2}$ and $Cu2p_{1/2}$[13,14] (Figure 6.3b). However, uncoated Cu foil shows broader peaks which

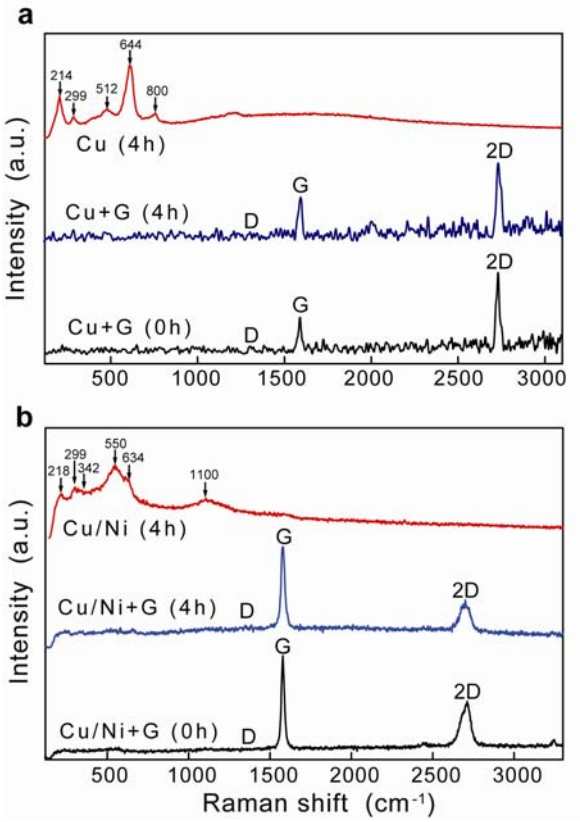

Figure 6.4 | Raman spectroscopy of air annealed graphene coated films. a, Spectra of graphene coated Cu foil taken before and after air anneal (lower, middle). Annealed Cu foil without graphene coating exhibits copper oxide peaks (upper). **b**, Spectra of graphene coated Cu/Ni foil taken before and after air anneal (lower, middle). Cu/Ni foil without graphene coating exhibits copper and nickel oxide peaks after annealing (upper).

correspond to different copper oxides, Cu_2O (932.5 and 952.3 eV), CuO (933.6 and 953.4 eV), and $Cu(OH)_2$ (934.7 and 954.5 eV). These data indicates that the graphene coating is clearly acting as a diffusion barrier, protecting the underlying copper from oxidation. Similarly, Figure 6.3d shows the XPS spectrum for the coated Cu/Ni foil. Two sharp peaks are present, corresponding to $Cu2p_{3/2}$ (932.6 eV) and $Ni2p_{3/2}$ (852.5 eV), demonstrating no change in the chemical composition of the protected metal. As before, inspection of the uncoated foil reveals two broader peaks, one is comprised of two nickel oxide peaks, NiO (854.5 eV) and $Ni(OH)_2$ (856.0 eV)[14,15], and the other is

comprised of three peaks - metallic Cu (932.6 eV) and two copper oxide peaks, CuO (933.6 eV), and $Cu(OH)_2$ (934.7 eV). These XPS spectra demonstrate that the uncoated Cu/Ni foil was oxidized to a certain extent after heat treatment. It is worth noting that the Cu/Ni alloy has some inherent corrosion resistance. The Cu/Ni alloy forms a protective film of Cu_2O with Ni compounds (*e.g.*, NiO) as minor components[16]. This oxide layer is more stable due to the presence of Ni atoms in the copper lattice, resulting in a lower number of defects. The oxide therefore provides better protection against further oxidation, which explains the presence of a metallic Cu signal in Figure 6.3d (lower). Nevertheless, in our experiments the graphene-coated Cu/Ni alloy still shows significantly better oxidation resistance, compared to the uncoated Cu/Ni alloy, as can be seen from the absence of an oxide signals in Figure 6.3d (upper).

Under air oxidation graphene also shows remarkable chemical stability. Figure 6.4 illustrates the Raman spectra of coated and uncoated Cu and Cu/Ni foil samples, before and after heating in air (200 °C, 4 h). Before treatment, the coated Cu foil exhibits a large 2D/G peak ratio which is indicative of high quality single layer graphene. The coated Cu/Ni foil also exhibits characteristics of high quality multilayer graphene—a low D band in conjunction with the distinct G and 2D peak shapes. After heat treatment, the uncoated Cu foil shows multiple peaks between 214 cm^{-1} and 800 cm^{-1}, corresponding to various copper oxides - Cu_2O, CuO, $Cu(OH)_2$. Uncoated Cu/Ni foil displays CuO and Cu_2O peaks, as well as NiO peaks (550 and 1100 cm^{-1})[17]. In contrast, the initial and final spectra of the coated foils are essentially identical. This clearly shows that the graphene is not only protecting the underlying metal, but is also

virtually unaltered by the oxidizing gas. The data shown in Figures 6.3 and 6.4 illustrate that both single and multi-layer graphene serve as ideal protection coatings by both preventing diffusion and remaining chemically inert.

Role of Defects in Protective Layers

In order to study the impact of defects that are expected in CVD graphene sheets, 2-dimensional micro-Raman spectroscopy was used on a graphene-coated Cu thin film. As noted above, an important aspect of graphene protection is its chemical inertness. Nevertheless, it is known that graphene is more likely to react at edges or where defects are present[18]. In Figure 6.5, we show a series of 2-D Raman maps taken on a graphene coated Cu thin film before and after H_2O_2 exposure. In particular we show spatial Raman mappings of signals for Cu oxide (490 – 652 cm^{-1}) and graphene D band (1300 – 1330 cm^{-1}), all normalized with respect to the G band signal. We make two notable observations in these 2-D Raman images. First, even before the H_2O_2 exposure, there exist areas of high oxide signal, which also show larger D bands (black arrow). This is most likely due to the presence of some residual copper oxide before the growth that resulted in graphene of poor quality. Second, while most graphene areas show no changes before and after the exposure (white arrow), there are areas that display a clear change. In these areas (red arrow), we observe a large increase in D/G ratio which is accompanied by the appearance of copper oxide peaks. This suggests that in the majority of areas the graphene is of higher quality and is able to protect the metal completely. In other areas, however, graphene does not act as a perfect diffusion barrier, and allows some of the etchant to penetrate through the

graphene layer and oxidize the metal. This overall increase in the presence of surface oxides, which are hydrophilic, is further supported by the water contact angle measurements presented in

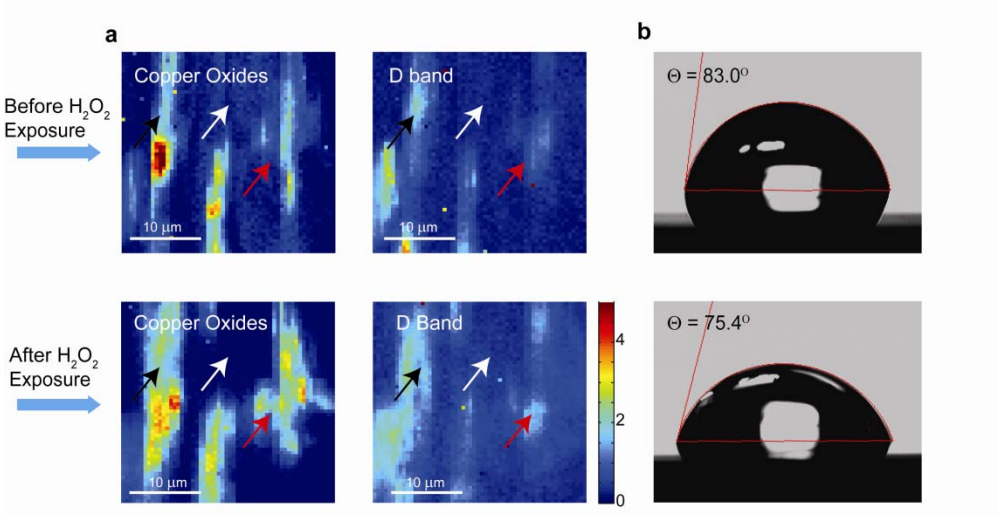

Figure 6.5 | Oxidation effects on graphene surface. a, Two-dimensional micro-Raman maps of graphene coated Cu film (500 nm thick) before (upper row) and after (lower row) H_2O_2 treatment (30%, 2 min), measured for the same location. Left column indicates Cu oxide/G (490 – 652 cm^{-1}) while right column portrays D/G (1300 – 1330 cm^{-1}) ratio. Black arrows indicate pre-existing oxidized areas before H_2O_2 exposure while white and red arrows show well protected areas and poorly protected areas after H_2O_2 exposure, respectively. **b**, Contact angle measurements of water on graphene coated Cu films before (upper) and after (lower) H_2O_2 treatment.

Figure 6.5b. Before H_2O_2 exposure, the graphene-coated Cu film exhibits a contact angle of 83º, comparable to values obtained for HOPG[19]. After peroxide treatment, however, the contact angle is reduced by over 10%, indicating the presence of a more hydrophilic film. Since this contact angle is much closer to that of HOPG than to the contact angle for pure copper oxide film[20], our results further suggest that the hydrophobic graphene sheet is still protecting the majority of the underlying metal.

In principle, perfect graphene without defects and grain boundaries, thanks to its impermeability and chemical inertness, will be able to preserve the surface of metal under reactive environments over a long period of time. However, real CVD graphene is expected to show non-ideal behaviors, one example of which is discussed above. In addition, the protection by a graphene layer would be severely limited in the presence of voids of finite size. This is similar to the behavior of conventional coatings, where a small hole allows the initiation and diffusion of local corrosion of underlying material. While such voids would be difficult to create in an ideal graphene due to its chemical and mechanical stability, a polycrystalline CVD graphene layer could be susceptible to such a mechanism. In our experiments, we indeed observe behavior that suggests a similar mechanism is in play, thus allowing chemical reactions to occur on metal surfaces in the vicinity of such voids.

The importance of graphene adhesion to the metal film is exemplified by the AFM images shown in Figure 6.6. Protected metal substrates were exposed to 0.5 M NaCl (Figure 6.6a) and 0.5 M H_2SO_4 (Figure 6.6b) for 10 mins and then examined for defects. Although the majority of the sheet is smooth and unaffected, certain areas with well-defined edges have been visibly attacked by the solutions. While the exact cause for this behavior is not clear, this could be explained by graphene being less strongly bound to the surface in these regions. The etchants are able to attack the metal grain boundaries, as seen before, but may also intercalate between the graphene and the metal surface in areas of weaker adhesion. This then allows the poorly adhered graphene patch to be lifted off and carried away. After graphene removal the surface is

roughened by the short exposure to the aqueous etch, whereas unexposed regions remain unaffected.

While weakened adhesion may contribute to decreased protection, diffusion at metal grain boundaries is another significant factor in accelerating corrosion. In Figure 6.6c we follow the etching of a thin copper film in 0.2M HNO_3. On both coated and uncoated films etch

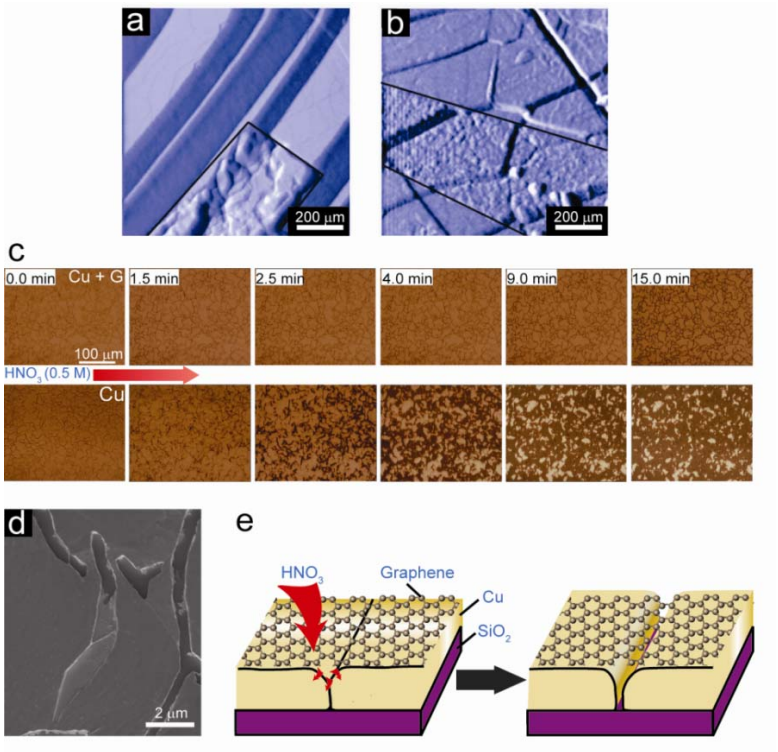

Figure 6.6 | Corrosion of graphene-coated metals in aqueous solutions. a, AFM images of graphene-coated Cu immersed in NaCl solution (0.5 M, 10 min) and **b** graphene-coated Cu/Ni alloy immersed in H_2SO_4 solution (0.5 M, 10 min). The exposed metal surface between the black lines has been roughened by the acid while the covered regions remain smooth. **c**, Time series optical micrograph snapshots of graphene coated (upper row) and uncoated (lower) Cu films under a strong etchant (HNO_3, 0.2 M). **d**, SEM image showing an etched Cu grain boundary partly covered by a graphene layer. **e**, Schematic depicting mass transport through defects/voids in graphene leading to the corrosion of the underlying copper film, which is faster along Cu grain boundaries.

originates along the metal grain boundaries. For coated films, however, although the channels are etched all the way down to expose the silicon oxide, the top of the channel can remain bridged by a graphene sheet (see Figure 6.6d). The proposed mechanism for this process is depicted in Figure 6.6e. While good graphene does act as a perfect diffusion barrier, "bad" graphene only limits it – eventually allowing the etchant to diffuse through, etch the metal, and diffuse the products out. The exact mechanism is still unclear – whether the diffusion occurs through the graphene sheet itself, or if the sheet is ruptured in weak spots, allowing the etchant to flow freely through those small holes. Despite these effects, the protected copper film is etched about ten times more slowly.

6.4 | Metal Etch Masks Using Graphene

From the previous section it follows that the protection that this graphene layer affords the metal substrate can also be used to selectively etch the substrate. One can choose to expose only certain areas of the Cu underneath by carefully patterning the graphene adlayer. The entire substrate can then be subjected to some form of etching, whereby the graphene will protect the Cu surface underneath while the unprotected regions are quickly removed. This general scheme is presented in Figure 6.7b below. In this case, we first grow graphene on 500 nm of Cu and then remove unwanted graphene areas using photolithography. After stripping the photoresist, we then expose these sample chips to an environment of Cl_2. It is known that Cl_2 rapidly reacts with bulk Cu, etching the surface by producing volatile $CuCl_x$ compounds (see Figure 6.7a)[21]. These products then evolve from the surface, exposing a fresh layer of Cu

underneath thus allowing the etch process to continue. Additionally, as discussed in Chapter 4, Cl_2 etches graphene very slowly[22], resulting in the rapid removal of Cu in areas without graphene leaving behind a patterned metal film. This process can be utilized for even high aspect ratio patterns, as shown in Figure 6.7c where the fidelity of the pattern is maintained.

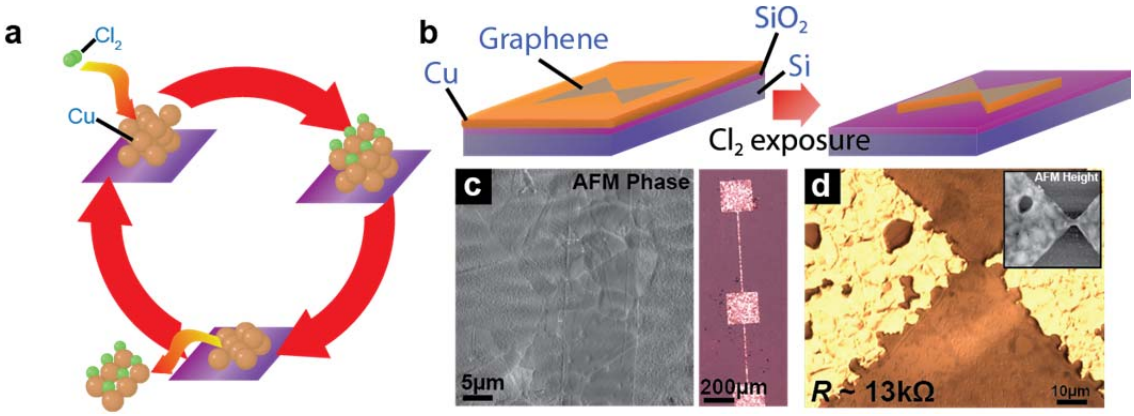

Figure 6.7 | Graphene as a metal etch mask. a, General schematic of Cu etch process using Cl_2. Cl_2 reacts with Cu to form volatile $CuCl_x$ compounds which sublime from the surface to expose a fresh Cu layer. **b**, General process for using graphene as a protective layer for metal etching. Graphene is first patterned using photolithography, similar to the processes discussed earlier. The substrate is then exposed to Cl_2 gas, preferentially etching the metal that is not covered by graphene. **c**, Left: AFM phase image of a partially etched Cu surface. The graphene surface remains smooth (strip) whereas the exposed Cu is visibly roughened. Right: Optical image of the pattern fully etched down to the SiO_2 surface. **d**, Optical image of a suspended graphene channel that has been undercut using Cl2. The resulting device shows a two-point resistance of ~13 kΩ. Inset: AFM height image showing the channel is suspended. Levendorf, *et al.* unpublished, 2010.

There is a small degree of undercut in this etching method, which can be taken advantage of in order to produce narrow suspended channels of graphene (Figure 6.7d). Similar to the transfer-free technique discussed in Chapter 3, these suspended regions are already contacted by the catalytic Cu underneath, making electrical

measurements straightforward to perform. Therefore, the combination of this etch technique with the Cl doping effects presented in Chapter 4, it is possible to create large arrays of such suspended devices with carefully tuned electrical properties.

These studies therefore show the broad potential of graphene as a passivation layer. The ability to both prevent diffusion, as well as its inertness in both oxidizing and acidic solutions allow for its use in a wide variety of environments. Although slight defects may arise at metal grain boundaries, in the absence of defects we note that the graphene sheets provide near perfect protection within grains. With further advances in graphene growth and careful control of the metal catalyst, we anticipate a significant improvement in the level of protection these films may provide. Furthermore, refinement of graphene transfer techniques may even make it possible to take advantage of this material's amazing properties in any compatible system.

6.5 | Graphene as a Platform for Chemical Synthesis

The results of the previous section are a direct consequence of the high degree of chemical and thermal stability that graphene exhibits. This characteristic, however, can also be helpful in directing chemical reactions, in particular those that have a significant degree of conjugation. Through this insight, our collaborators at Cornell experimented in the use of graphene films as a growth substrate for covalent organic frameworks (COF)[23].

COFs are crystalline structures comprised of specific molecular building blocks that are joined by covalent bonds. These materials are typically porous and have therefore been proposed as ideal media for hydrogen storage, photovoltaics, and

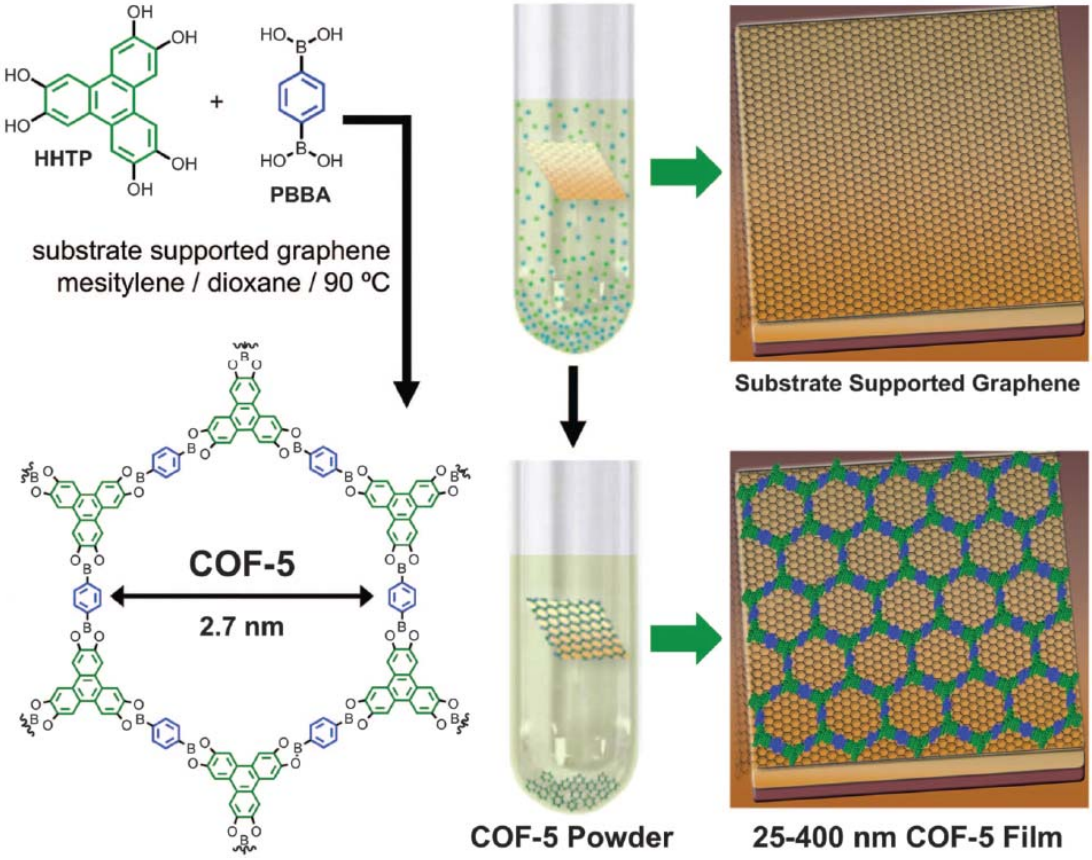

Figure 6.8 | Synthesis of COF-5 on graphene support layer. The COF-5 synthesis is performed in the conventional manner but in the presence of a graphene coated substrate. This leads to both a thin film of aligned COF-5 on the graphene, as well as the expected powder. Reproduced from Ref. 23.

chemical sensing platforms. Traditional synthetic methods, however, yield microcrystalline powders—limiting the utility of these structures. In the presence of graphene, however, it was found that there is an induced vertical alignment in the formation of COF crystals. This finding proved to be general in nature, and was shown to work for three COF films.

The general reaction scheme is presented above in Figure 6.8. Conventional solution COF reactions are performed in the presence of a graphene coated substrate (here, graphene on $Cu/SiO_2/Si$). The presence of this substrate induces the formation

of an aligned film directly on the graphene layer, while not impeding the production of the standard randomly oriented COF powder. This can be clearly seen in the X-ray scattering data depicted in Figure 6.9. As expected, the powder (Figure 6.9a) shows no preferred orientation, with intensities relatively uniform over the scattering arc. This is in stark contrast to the experiment performed on the graphene supported films (Figure 6.9b), where there are well defined peaks along the $Q_{||}$ direction only. This data suggests that the graphene supported COF crystals show vertical (*c*-axis) orientation, but individual crystals are rotated about this axis.

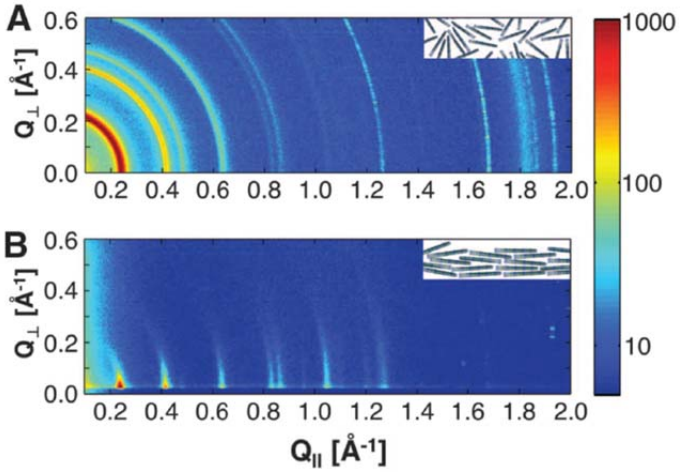

Figure 6.9 | X-ray scattering data of powder and film. a, The scattering data from the powder shows randomly oriented COF-5 crystals (see inset). **b**, Grazing incidence diffraction measurements show crystal alignment in the z-dimension (inset). Reproduced from Ref. 23.

This finding is important to the COF community, opening up the potential for true rational formation of useful films. Furthermore, graphene can also be used as a bottom contact for any electrical devices that are to be made out of these resulting materials. The impact goes beyond this particular field, however, as this study represents the general utility of graphene as a platform for chemical synthesis that may

benefit from well-controlled π-conjugated substrates.

6.6 | Summary and Outlook

In this chapter we took advantage of the inertness and stability of graphene in order to perform a diverse set of experiments, including exploiting its inertness to protect reactive surfaces. These studies inherently provide a route for the patterning of metal surfaces as well, which we showed in our model graphene/Cu system. This enables the large-scale formation of suspended graphene strips that can be simultaneously tuned via exposure to Cl_2 gas—an application of the effects seen in Chapter 4. Beyond this, our collaborators have also developed a method for synthesizing aligned organic crystals. This procedure is again a direct consequence of the stability and structure of the graphene sheets, which induces a vertical alignment of these organic films. These studies represent the impact graphene can have on a broad number of scientific fields and further illuminate the degree to which graphene is currently underutilized.

REFERENCES

1. Lee, C., Wei, X., Kysar, J. W. & Hone, J. Measurement of the elastic properties and intrinsic strength of monolayer graphene. *Science* **321,** 385–388 (2008).

2. Bunch, J. S. *et al.* Electromechanical resonators from graphene sheets. *Science* **315,** 490–493 (2007).

3. Bunch, J. S. *et al.* Impermeable atomic membranes from graphene sheets. *Nano Lett.* **8,** 2458–2462 (2008).

4. Yuk, J. M. *et al.* High-resolution EM of colloidal nanocrystal growth using graphene liquid cells. *Science* **336,** 61–64 (2012).

5. Nair, R. R., Wu, H. A., Jayaram, P. N., Grigorieva, I. V & Geim, A. K. Unimpeded permeation of water through helium-leak-tight graphene-based membranes. *Science* **335,** 442–444 (2012).

6. Chen, S. *et al.* Oxidation resistance of graphene-coated Cu and Cu/Ni alloy. *ACS Nano* **5,** 1321–1327 (2011).

7. Stoll, J. D. & Kolmakov, A. Electron transparent graphene windows for environmental scanning electron microscopy in liquids and dense gases. *Nanotechnology* **23,** 505704 (2012).

8. Chen, Q. *et al.* 3D motion of DNA-Au nanoconjugates in graphene liquid cell electron microscopy. *Nano Lett.* **13,** 4556–4561 (2013).

9. Holt, J. K. *et al.* Fast mass transport through sub-2-nanometer carbon nanotubes. *Science* **312,** 1034–1037 (2006).

10. Shivaraman, S., Chandrashekhar, M. V. S., Boeckl, J. J. & Spencer, M. G. Thickness Estimation of Epitaxial Graphene on SiC Using Attenuation of Substrate Raman Intensity. *J. Electron. Mater.* **38,** 725–730 (2009).

11. Li, X. *et al.* Large-area synthesis of high-quality and uniform graphene films on copper foils. *Science* **324,** 1312–1314 (2009).

12. Li, X., Cai, W., Colombo, L. & Ruoff, R. S. Evolution of graphene growth on Ni and Cu by carbon isotope labeling. *Nano Lett.* **9,** 4268–4272 (2009).

13. Poulston, S., Parlett, P. M., Stone, P. & Bowker, M. Surface Oxidation and Reduction of CuO and Cu_2O Studied Using XPS and XAES. *Surf. Interface Anal.* **24,** 811–820 (1996).

14. Dubé, C. E., Workie, B., Kounaves, S. P., Robbat, A. & Aksu, M. L. Electrodeposition of Metal Alloy and Mixed Oxide Films Using a Single-Precursor Tetranuclear Copper-Nickel Complex. *J. Electrochem. Soc.* **142,** 3357–3365 (1995).

15. Sasi, B. & Gopchandran, K. G. Nanostructured mesoporous nickel oxide thin films. *Nanotechnology* **18,** 115613 (2007).

16. Yuan, S. J. & Pehkonen, S. O. Surface characterization and corrosion behavior of 70/30 Cu–Ni alloy in pristine and sulfide-containing simulated seawater. *Corros. Sci.* **49,** 1276–1304 (2007).

17. Chou, M. H., Liu, S. B., Huang, C. Y., Wu, S. Y. & Cheng, C.-L. Confocal Raman spectroscopic mapping studies on a single CuO nanowire. *Appl. Surf. Sci.* **254,** 7539–7543 (2008).

18. Jiang, D., Sumpter, B. G. & Dai, S. Unique chemical reactivity of a graphene nanoribbon's zigzag edge. *J. Chem. Phys.* **126,** 134701 (2007).

19. Yan, A., Xiao, X., Külaots, I., Sheldon, B. W. & Hurt, R. H. Controlling water contact angle on carbon surfaces from 5° to 167°. *Carbon* **44,** 3116–3120 (2006).

20. Chang, F.-M., Cheng, S.-L., Hong, S.-J., Sheng, Y.-J. & Tsao, H.-K. Superhydrophilicity to superhydrophobicity transition of CuO nanowire films. *Appl. Phys. Lett.* **96,** 114101 (2010).

21. Efremov, A. M. & Svettsov, V. I. Dry Etching of Copper Using Chlorine: A Review. *Russ. Microelectron.* **31,** 179–192 (2002).

22. Wendt, H., Dermeik, S. & Ziogas, A. Chlorine corrosion of graphites and technical carbons - I. Reaction with gaseous chlorine at elevated temperatures. *Mater. Corros. und Korrosion* **41,** 457–463 (1990).

23. Colson, J. W. *et al.* Oriented 2D covalent organic framework thin films on single-layer graphene. *Science* **332,** 228–231 (2011).

CHAPTER 7

CONCLUSIONS AND FUTURE WORK

7.1 | Summary of Thesis

The work we presented in this thesis can be viewed as all falling under one goal: to find new and useful applications of 2-dimensional materials. In pursuit of this, we have needed to develop the variety of tools and techniques which have allowed us to manipulate the qualities of these films. We initially focused on the controlled synthesis of these materials, which formed the basis for all future studies. In this section, we presented our work demonstrating the first successful growth of graphene on thin-films of copper[1]. This, combined with our method of transfer-free fabrication represented the earliest work on truly wafer-scale Cu CVD graphene.

After establishing techniques for the intrinsic growth of graphene, we then turned our attention towards rationally altering its composition via the introduction of dopant atoms. We found that briefly exposing graphene to molecular chlorine after growth resulted in strong *p*-type doping, resulting from the chemical bonding of Cl atoms at defect and edge sites. This method was found to be both tunable through the dilution of Cl_2 as well as reversible upon a mild anneal—suggesting use as a recoverable chemical sensor. We also presented experiments on the substitutional insertion of B atoms, again allowing controlled *p*-type doping. This work, done in collaboration with the Pasupathy group at Columbia University, is particularly useful given the non-destructive nature of the process as well as the fact that *n*-type dopants (N atoms) had already been previously reported[2]. Thus, combining B- and N-doped

graphene now provides a route towards the formation of *synthesized*—as opposed to *fabricated*—*p*-*n* junctions.

Next, we used this developed expertise in synthesis to unite dissimilar 2D materials into continuous hybrid sheets[3]. We showed that this process, which we called patterned regrowth, was general as we demonstrated successful integration of both intrinsic and doped graphene layers as well as graphene and hexagonal boron nitride (*h*-BN). This method has exciting applications in the formation of the thinnest possible 3D electronics, which we highlighted by fabricating atomically-flat 3D interconnects out of graphene/*h*-BN films. By incorporating a semiconductor such as MoS_2, this process can be used to create complex circuitry and electronics in the thinnest possible system.

Lastly, we proposed novel uses of graphene based on its remarkable physical properties. Taking advantage of its stability, we showed that graphene could be utilized as an effective etch mask for copper under Cl_2 exposure. Due to its low reactivity with Cl_2, patterned graphene layers remain largely unetched while the exposed Cu surfaces rapidly react and are removed. This process could therefore be used to create complicated patterns with high fidelity, as well as suspended graphene channels. In a similar application, along with our collaborators in the Ruoff group we suggested the use of graphene as an effective oxidation barrier[4]. Here graphene protects the underlying metal surface by preventing metal exposure to ambient environments—therefore limiting oxidation to diffusion initiating at grain boundaries or edges.

7.2 | The Prospect of 2D Materials

While the major focus of thesis was on graphene as our model system, many other 2D systems exist and are waiting to be studied[5]. Significantly, most of the techniques and tools we have established are completely general and can theoretically be applied to any atomically-thin substance. It is therefore an extremely exciting time for the field, as we are now able to rapidly investigate and characterize this wealth of new materials. Indeed, this process is already well underway, with several groups publishing papers recently on MoS_2[6–9] and WS_2[10–12]—which were rarely studied only a few years ago. Furthermore, future work is not limited to focusing on homogenous systems, as researchers can now use our patterned regrowth method to investigate several combinations of lateral heterojunctions.

Experiments can also be extended into 3 dimensions by stacking these films on top of each other. In this case, the materials do not even need to be dissimilar; interest in twisted bilayer graphene has recently ignited a flurry of activity in the field, including recent works by members of the Park group[13–16]. This also introduces two new parameters to play with, since changing the relative rotation angle (θ_{rel}) or interlayer distance (d_{int}) can drastically change their interaction. While heteroatomic layered materials, such as boron nitride, introduce an additional complication, such studies have very recently been completed[16]—indicating the speed at which the community is advancing. This momentum, combined with improvements in the methods we have created, can therefore lead to the discovery of exciting new materials and structures which have the potential to greatly impact both science and society.

REFERENCES

1. Levendorf, M. P., Ruiz-Vargas, C., Garg, S. & Park, J. Transfer-Free Batch Fabrication of Single Layer Graphene Transistors. *Nano Lett.* **9,** 4479–4483 (2009).

2. Zhao, L. *et al.* Local atomic and electronic structure of boron chemical doping in monolayer graphene. *Nano Lett.* **13,** 4659–4665 (2013).

3. Levendorf, M. P. *et al.* Graphene and boron nitride lateral heterostructures for atomically thin circuitry. *Nature* **488,** 627–632 (2012).

4. Chen, S. *et al.* Oxidation resistance of graphene-coated Cu and Cu/Ni alloy. *ACS Nano* **5,** 1321–1327 (2011).

5. Coleman, J. N. *et al.* Two-dimensional nanosheets produced by liquid exfoliation of layered materials. *Science* **331,** 568–571 (2011).

6. Radisavljevic, B., Radenovic, A., Brivio, J., Giacometti, V. & Kis, A. Single-layer MoS2 transistors. *Nature Nanotech.* **6,** 147–150 (2011).

7. Mak, K. F., He, K., Shan, J. & Heinz, T. F. Control of valley polarization in monolayer MoS2 by optical helicity. *Nature Nanotech.* **7,** 494–498 (2012).

8. Liu, K.-K. *et al.* Growth of large-area and highly crystalline MoS_2 thin layers on insulating substrates. *Nano Lett.* **12,** 1538–1544 (2012).

9. Zeng, H., Dai, J., Yao, W., Xiao, D. & Cui, X. Valley polarization in MoS_2 monolayers by optical pumping. *Nature Nanotech.* **7,** 490–493 (2012).

10. Elías, A. L. *et al.* Controlled Synthesis and Transfer of Large-Area WS_2 Sheets: From Single Layer to Few Layers. *ACS Nano* **7,** 5235–5242 (2013).

11. Gutiérrez, H. R. *et al.* Extraordinary room-temperature photoluminescence in triangular WS2 monolayers. *Nano Lett.* **13,** 3447–3454 (2013).

12. Georgiou, T. *et al.* Vertical field-effect transistor based on graphene-WS_2 heterostructures for flexible and transparent electronics. *Nature Nanotech.* **8,** 100–103 (2013).

13. Havener, R. W. *et al.* Hyperspectral imaging of structure and composition in atomically thin heterostructures. *Nano Lett.* **13,** 3942–3946 (2013).

14. Brown, L. *et al.* Twinning and twisting of tri- and bilayer graphene. *Nano Lett.* **12,** 1609–1615 (2012).

15. Havener, R. W., Zhuang, H., Brown, L., Hennig, R. G. & Park, J. Angle-resolved Raman imaging of interlayer rotations and interactions in twisted bilayer graphene. *Nano Lett.* **12,** 3162–3167 (2012).

16. Kim, C.-J. *et al.* Stacking Order Dependent Second Harmonic Generation and Topological Defects in h-BN Bilayers. *Nano Lett.* **13,** 5660–5565 (2013).